

# **The Effects of Nonuniform Microstructures on Ni/Al Reactive Laminate Sheets and Powders**

By Adam Stover

A dissertation submitted to Johns Hopkins University in conformity with  
the requirements for the degree of Doctor of Philosophy

Baltimore, Maryland  
July, 2014

## **Abstract**

This work aims to make progress in understanding the relationship between nonuniform microstructures in Ni/Al reactive systems and reactive properties. To this end, alternating Ni and Al sheets were cold-rolled into fully dense structures and had their reactivity tuned by further cutting, stacking and rerolling. In addition, some of the resulting foils were mechanically ground into mechanically processed composite powders.

The cold-rolled microstructure was extensively characterized via scanning-electron microscopy (SEM) and a 'home-built' MATLAB code that determined the bilayer spacing and the local Ni atomic fraction associated with each bilayer. Differential scanning calorimetry, gas pycnometry density analysis and self-propagating reaction velocity/maximum temperature determination were performed on all of the foil types. The reaction velocity and maximum temperature were found to vary with processing conditions rather than the volume average bilayer thickness, with foils that had more gradual rolling passes having a hotter and faster reaction compared to foils with more severe plastic deformation during rolling. The detailed microstructural information gathered from SEM images was used to simulate diffusion during self-propagating reaction to predict the maximum temperature. While there is a lot of variation between SEM images, we found that the distribution of bilayer thicknesses and local chemistries in the foils with gradual rolling passes have a more uniform bilayer thickness distribution, which promotes more complete reaction on the time scale of the self-propagating front and therefore a higher maximum temperature. The source for the variation in propagation velocity is currently unknown.

An analogous set of rolled foils were fabricated to investigate the propagation mechanism using high-speed cameras. However, their propagation velocities vary with bilayer, but the mechanism of propagation is similar to a previously reported one in the Al/Co system. Furthermore, the measured maximum temperatures are constant. The net velocities of the foils are shown to vary inversely with the volume average bilayer thickness, as well the local propagation rate perpendicular to that direction, which agrees with previously reported results.

The mechanically fabricated powders show variation in both physical density and DSC behavior as a function of both original foil microstructure and particle size. As the particle size is decreased, the DSC heat release decreases as Al melting and mixing becomes more prevalent, with the strongest decreases seen in particles with the coarsest microstructure. The evolved heats are also plotted as a function of the average number of bilayers in each particle and the result is that they all fall on one curve. This is an important parameter to bear in mind when using these powders for commercial applications. Furthermore, of the three particle types fabricated, one becomes Ni-rich at the smallest particle sizes; one becomes Al-rich while one shows little variation.

We attribute this variation to non-random breakup during the grinding process, resulting in the smallest particle sizes having the highest concentration of Ni-rich and Al-rich bilayers, which leads to Al melting and mixing as well as a reduction in total heat release during DSC scans. We are able to model the reduction in heat by using a simulated bimodal distribution in bilayer Ni atomic fraction taken as a subset of the total bilayer chemistry distribution, leading us to believe that our hypothesis of non-random breakup is a reasonable one.

## Acknowledgements

I have been fortunate to enter such an intellectually fostering setting at Johns Hopkins. Working under the tutelage Professor Timothy Weihs has been such a pleasure and positive experience in innumerable ways. I have grown and matured both as a researcher and a person and for that I am duly grateful. Prof Weihs has been a fantastic role model both in and outside of the lab and has helped me through many challenges during my time at Johns Hopkins. His influences have made me a better researcher with a keener eye for detail.

I also want to thank the members of my committee, Profs. Timothy Weihs, Todd Hufnagel, Omar Knio, Robert Cammarata and Kevin Hemker. I was previously advised by Prof. D. Howard Fairbrother in the chemistry department and would like to thank him for his helpful insights during my time in his laboratory.

I have received much help from my labmates in the Weihs Group. Many, many thanks go to Gregory Fritz for his help and support in ways too numerable to delineate. Thank you Sara Barron for your help measuring the maximum temperature and reaction velocity. Thank you Howie Joress for your insights into density separation. You saved me many weeks with your ideas. Thank you Nick Krywopusk for your help swaging and coding. Many thanks to David Gibbins for your help continually running different code iterations. Katie Fisher made lab a sunnier place to be and is sorely missed.

There were many staff members in the department who have been extremely helpful throughout my time at Hopkins. Thank you Mark Koonz for your SEM wizardry. Thank you Jeanine Majewski for tracking me down and harassing me to register for

classes. Marge Weaver was instrumental for obtaining laboratory software and equipment. Thank you Dorothy Reagle for all your help shipping things last-minute.

Many thanks go to the Mike Franckowiak, Walt Krug and Frank Cook in the machine shop. The engineering shop was a great resource of knowledge and you were far too generous with advice, tools and your time.

I am grateful to the Office of Naval Research and their generous funding of my research. I have been able to acquire many instruments integral to my research.

Thank you, Hopkins Harriers and your 10:30 daily reminder to get outside and run. I thoroughly enjoyed every run, even when Tom and Pete decided to tempo back from Gilman. I already miss your company on my (now much less frequent) runs.

Thank you Steve Farias and Alex Kinsey for giving Taggart and me a place to crash while going back and forth between Albany and Baltimore.

I want to thank my parents, Sue and Jeff Stover for their support throughout my life. I also want to thank my grandfather, David Haylett, who always pushed me to excel in all that I do.

Last but certainly not least, I would like to thank my wife Allie. She has been incredibly supportive and patient while I split my time between Albany and Baltimore.

# Table of Contents

|  |      |
|--|------|
| Abstract.....  | ii   |
| Acknowledgements.....  | iv   |
| Table of Contents.....   | vi   |
| List of Figures and Tables.....                                      | viii |
| 1. Introduction.....   | 1    |
| 1.1 Background on Reactive Materials.....                            | 1    |
| 1.2 Fabrication of RM.....   | 2    |
| 1.2.1 PVD.....   | 2    |
| 1.2.2 Mechanical Fabrication.....                                    | 4    |
| 1.3 Uses for RM.....   | 7    |
| 1.3.1 Bonding with RM.....   | 7    |
| 1.3.2 Reactive Fragments.....  | 9    |
| 1.3.3 RM Delays and Fuses.....                                       | 11   |
| 2. Fabrication and Characterization of Ni/Al Reactive Materials..... | 16   |
| 2.1 Fabrication of Rolled Ni/Al Laminates.....                       | 16   |
| 2.2 Fabrication of Ni/Al Composite Powders.....                      | 17   |
| 2.3 Characterization Techniques.....                                 | 19   |
| 2.3.1 Scanning-Electron Microscopy.....                              | 19   |
| 2.3.2 Differential Scanning Calorimetry.....                         | 19   |
| 2.3.3 Gas Pycnometry.....  | 20   |
| 2.3.4 Velocity and Maximum Temperature Measurement.....              | 20   |
| 3. Mechanical Properties of Cold-Rolled Ni/Al Laminates.....         | 22   |
| 3.1 Introduction.....  | 22   |
| 3.2 Experimental Methods.....  | 23   |
| 4. Microstructure and Properties of Cold-Rolled Ni/Al Laminates..... | 30   |
| 4.1 Introduction.....  | 30   |
| 4.2 Experimental Methods.....  | 32   |
| 4.2.1 Materials Fabrication and Characterization.....                | 32   |
| 4.2.2 Microstructural Analysis.....                                  | 32   |
| 4.2.3 Verification of Microstructural Analysis.....                  | 34   |

|   |     |
|---|-----|
| 4.3 Results.....  | 35  |
| 4.4 Discussion.....   | 47  |
| 4.4.1 Density and Chemistry.....  | 47  |
| 4.4.2 Average Bilayer Thickness.....  | 49  |
| 4.4.3 Bilayer Spatial and Thickness Distributions.....                        | 51  |
| 4.4.5 Predicting $T_{\max}$ for Self-propagating Reactions.....               | 53  |
| 4.4.6 Predicting Reaction Velocity.....                                       | 58  |
| 5. Mechanical Fabrication and Characterization of Ni/Al Laminate Powders..... | 64  |
| 5.1 Introduction.....   | 64  |
| 5.2 Experimental Methods.....   | 65  |
| 5.3 Results.....  | 66  |
| 5.4 Discussion.....   | 75  |
| 6. Unsteady Reaction Propagation in Cold-Rolled Ni:Al Laminates.....          | 87  |
| 6.1 Introduction.....   | 87  |
| 6.2.1 Materials Fabrication and Characterization.....                         | 89  |
| 6.2.2 High-speed Video Analysis.....  | 89  |
| 6.3 Results.....  | 90  |
| 7. Conclusions and Future Work.....   | 109 |
| 7.1 Conclusions.....  | 109 |
| 7.2 Future Work.....  | 111 |

## List of Figures and Tables

|   |       |
|---|-------|
| Figure 1.1 Schematic of the sputtering process .....  | 2     |
| Figure 1.2 SEM of a sputtered Ni/Al reactive foil .....                                       | 3     |
| Figure 1.3 Cold-Rolling process schematic .....   | 4     |
| Figure 1.4 Swaging schematic .....  | 5     |
| Figure 1.5 Brazing with reactive material .....   | 8     |
| Figure 1.6 Reactive fragment ignition process.....  | 9     |
| Figure 1.7 Particle propagation process .....   | 12    |
| Figure 2.1: Cold-Rolling Process Schematic.....   | 16    |
| Figure 2.2 Cross-sectional SEM images of cold-rolled microstructures .....                    | 17    |
| Figure 2.3 Powder fabrication schematic .....   | 18    |
| Figure 2.4 Dogbone specimen dimensions .....  | 21    |
| Table 3.1 Initial foil thicknesses, number of times rolled and final bilayer thickness.....   | 21    |
| Figure 3.1 Stress/Strain curves for foils with 305 $\mu\text{m}$ initial bilayer.....         | 21    |
| Figure 3.2 Stress/Strain curves for foils with 43 $\mu\text{m}$ initial bilayer.....          | 21    |
| Figure 3.3 Tensile test compilation .....   | 21    |
| Figure 3.4 Hardness values and estimated yield strengths .....                                | 21    |
| Figure 4.1 Scatterplots of Ni atomic fraction versus bilayer thickness .....                  | 33    |
| Figure 4.2 Density calculations and estimates from SEM images .....                           | 33    |
| Table 4.1 Microstructural quantification of the rolled composites.....                        | 33    |
| Figure 4.3 Bilayer volume fraction histograms .....   | 37    |
| Figure 4.4 Bilayer volume fractions and their corresponding chemistry .....                   | 40    |
| Figure 4.5 Volume fraction of bilayers relative to the volume average bilayer thickness ..... | 41    |
| Figure 4.6 DSC curves .....   | 42    |
| Figure 4.7 DSC peak temperatures .....  | 42    |
| Figure 4.8 Integrated DSC heats.....  | 42    |
| Figure 4.9 Maximum flame temperature and reaction velocity .....                              | 42    |
| Figure 4.10 Unsteady propagation mechanism.....   | 42    |
| Figure 4.11 Calculated enthalpy of formation curve.....                                       | 42    |
| Figure 4.12 Maximum temperature predictions .....   | 55    |
| Figure 4.13 Maximum temperature predictions for longer diffusion scales .....                 | 57    |
| Figure 4.14 Reaction velocity predictions .....   | 59    |
| Figure 5.1 Powder mass fractions after blending.....  | 65    |
| Figure 5.2 SEM images of original foils .....   | 66    |
| Table 5.1 Volume average bilayer thickness of original foils .....                            | 67    |
| Figure 5.3 SEM images of original foils .....   | 68    |
| Figure 5.4 Coefficient of variance for powder sample size .....                               | 69    |
| Figure 5.5 DSC curves as a function of particle size and initial microstructure.....          | 70-71 |
| Figure 5.6 Integrated DSC heats.....  | 72    |

|   |        |
|---|--------|
| Figure 5.7 DSC curves of small powders ground from large ones.....                | 73     |
| Figure 5.8 Simulated bimodal distributions.....                                   | 80     |
| Figure 5.9 Simulated heat release of subsets of SEM images.....                   | 842    |
| Figure 5.10 Heats of reaction versus bilayers per particle.....                   | 842    |
| Table 6.1 Microstructural quantification of the foils .....                       | 89     |
| Figure 6.1 SEM images of the foils.....   | 90     |
| Figure 6.2 DSC curves .....   | 91     |
| Figure 6.3 DSC peak temperatures .....  | 92     |
| Figure 6.4 Integrated DSC heats.....  | 93     |
| Figure 6.5 Net propagation velocity versus volume average bilayer thickness ..... | 94     |
| Figure 6.6 Maximum reaction temperature .....                                     | 95     |
| Figure 6.7 Reaction mechanism photographs.....                                    | 96     |
| Figure 6.8 Reaction band growth versus time for both directions .....             | 98-100 |
| Figure 6.9 Average band growth velocity.....                                      | 101    |
| Figure 6.10 Band growth velocity overlaid with net propagation velocity.....      | 101    |

# 1. Introduction

## 1.1 Background on Reactive Materials

Reactive materials (RM) are combinations of elements or oxides that, when given an external stimulus such as a spark, a thermal pulse, or rapid deformation, undergo sustained exothermic reactions releasing substantial amounts of heat [1–10]. This field became a subject of research over 100 years ago with the discovery of the aluminum and iron oxide thermite reaction [11], and numerous other thermite systems have been discovered and studied since then [12]. In the 1960's Soviet scientists found that elements can combine in an exothermic, self-propagating, high-temperature synthesis (SHS) reaction to form intermetallic products [13,14].

In contrast to thermite reactions which involve oxidation, SHS reactions do not. Rather, they consist of A-A bonds and B-B bonds breaking and forming A-B bonds, where A and B are transition metals or light elements such as C, B, Al or Si. For example, Ni and Al are two metals which can react through SHS to form Ni-Al intermetallics. During the reaction of an equal number of Ni and Al atoms, 61 kJ/mol or 1380 J/g of heat is released [15]. The rate of reaction or heat generation is governed by the average rate of atomic interdiffusion and the average distance between reacting species. For planar geometries, this distance is equivalent to  $\frac{1}{4}$  of the bilayer thickness in a binary (A/B) multilayer foil. The speed of propagation is determined by both the rate of heat generation and the rate of heat conduction away from the reaction zone [16–18].

## 1.2 Fabrication of RM

### 1.2.1 PVD

Physical vapor deposition (PVD), specifically magnetron sputtering, is a process which uses physical methods to generate a vapor that can then be deposited as opposed to chemical reactions. Magnetron sputtering is a specific type of PVD process which uses  $\text{Ar}^+$  ions to bombard a negatively charged sputter target [19,20]. The Ar atoms are

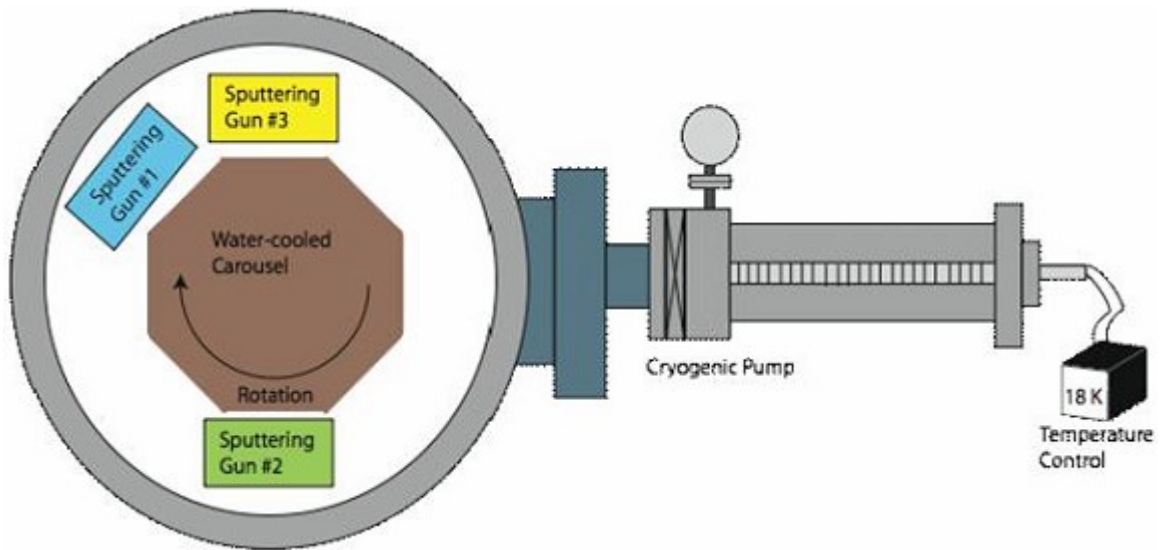


Figure 1.1 Schematic of the sputtering process. The substrate rotates between Ni and Al guns, each depositing one layer and with each complete rotation a bilayer is deposited. The speed of rotation and the sputtering power determine the bilayer period.

ionized in the plasma above the sputter target and then are accelerated towards the target. Upon impact with the target neutral target atoms are ejected and some of them condense on a cooled substrate. Magnets are used to aid efficiency and concentrate the charged gaseous species and secondary electrons around the sputter target, typically forming a “racetrack.” However, due to the use of magnetic fields only nonmagnetic metals and alloys can be easily sputtered.

To sputter thin reactive laminate films a rotating substrate is positioned between two sputter guns, each sputtering a different material (See Figure 1.1). A combination of deposition rates for each gun and the rotation rate for the carousel will determine the average chemistry and the bilayer thickness for the material deposited, and the total time sputtered determines the final thickness of the thin film. Figure 1.2 shows a scanning electron micrograph of a sputtered Ni/Al multilayer film with the bilayer marked. The power of the sputter guns can be changed to obtain different elemental ratios, such as 1:1, 3:1 and 3:2.

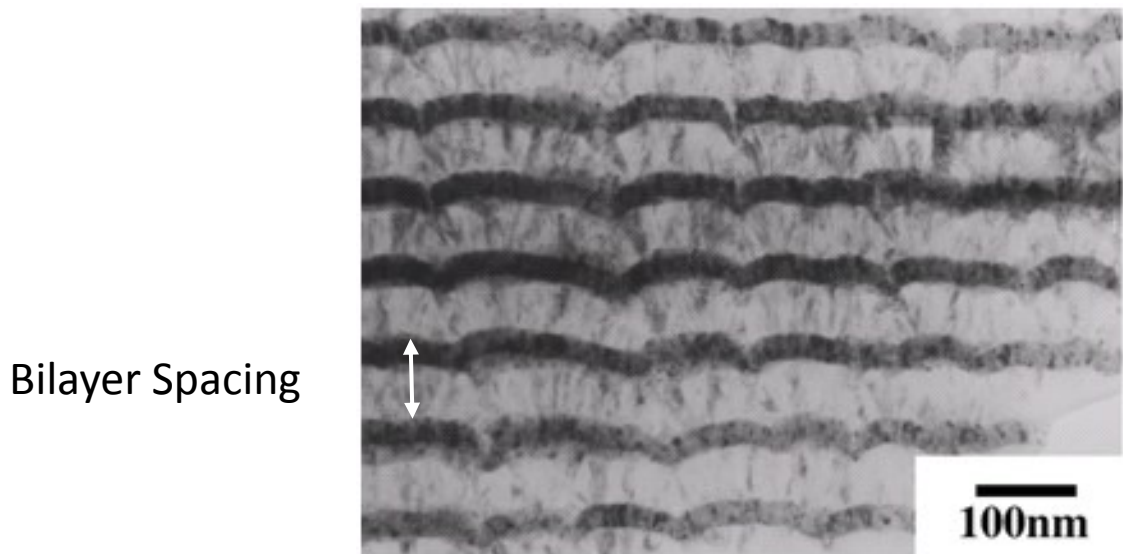


Figure 1.2 SEM of a sputtered Ni/Al reactive foil. Ni layers are light and Al layers are dark. Note the uniformity of the bilayer period (marked with a white arrow.)

Sputtering is a powerful technique that can be used to quickly probe different reactive binary chemistries and various ratios for any given binary intermetallic driver. Different targets can be changed quickly to test different formulations, and the gun powers can be altered to generate different elemental ratios. In addition, the resulting foils can be reacted in air to test their susceptibility to oxidation by examining mass gain

and temperature profiles [21]. However, sputtering is limited in materials selection because magnetic materials such as Ni are difficult to sputter. In addition, some materials such as B or C have very low sputter rates due to low sputter yields and charging difficulties. Furthermore, the capital costs of sputtering are quite high, full material utilization is difficult and the geometry of sputtered materials is limited to foils (on flat surfaces) and powders (on a mesh or lattice.)

### 1.2.2 Mechanical Fabrication

There are many ways to fabricate layered or composite RM using mechanical methods, which involve compressing metal sheets, foils or powders together. For example, cold-isostatic pressing [22], hot-isostatic pressing [23], swaging [24] and rolling [25–33] can be used to combine alternating sheets of different

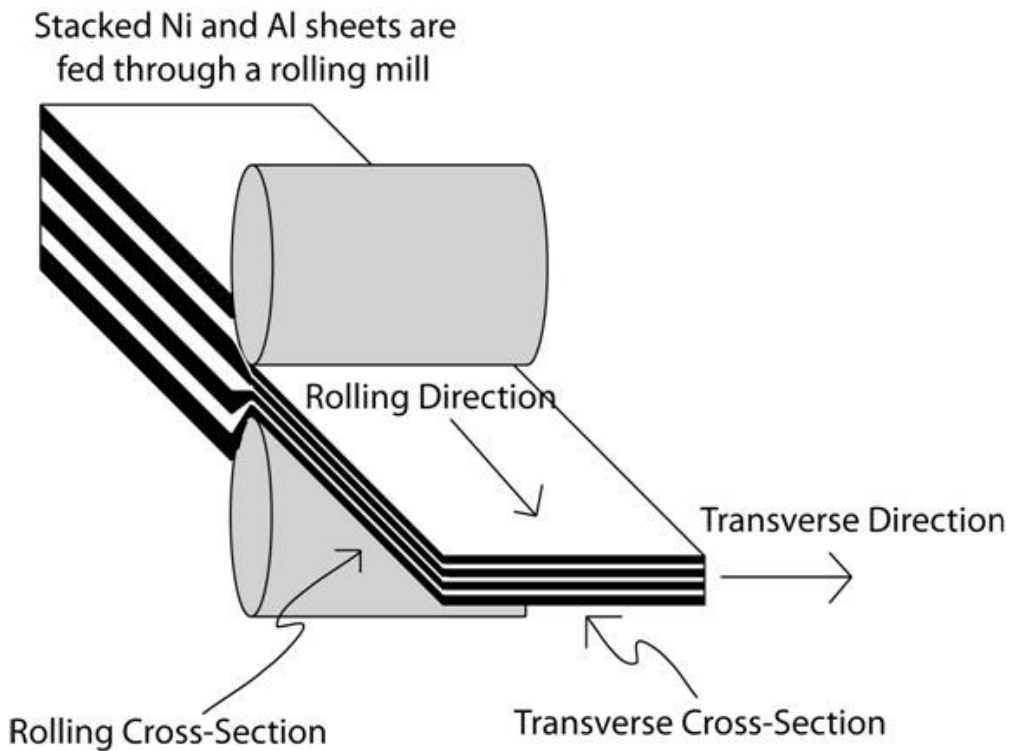


Figure 1.3 Schematic of the rolling process. Two alternating foils are stacked to build a structure and passed through a rolling mill, achieving a 50% thickness reduction. This

thickness reduction bonds the foils together and reduces the average bilayer. After, the foil can be cut in half, stacked and rerolled, further refining the microstructure.

reactants to form a solid, layered and reactive composite. Alternatively, reactant powders can be ball-milled [34–37] together to form composite particles in which one reactant is mechanically embedded in the other. Typically, the amount of strain imparted during processing controls the average diffusion distance, so the number of swaging reductions or the number of cutting, restacking and rerolling passes controls microstructure and properties. Figure 1.3 depicts the rolling process while Figure 1.4 shows the front of a 4 die swager.

When loose sheets are stacked together and passed through a rolling mill with a sufficient thickness reduction, the severe plastic deformation serves two purposes: it

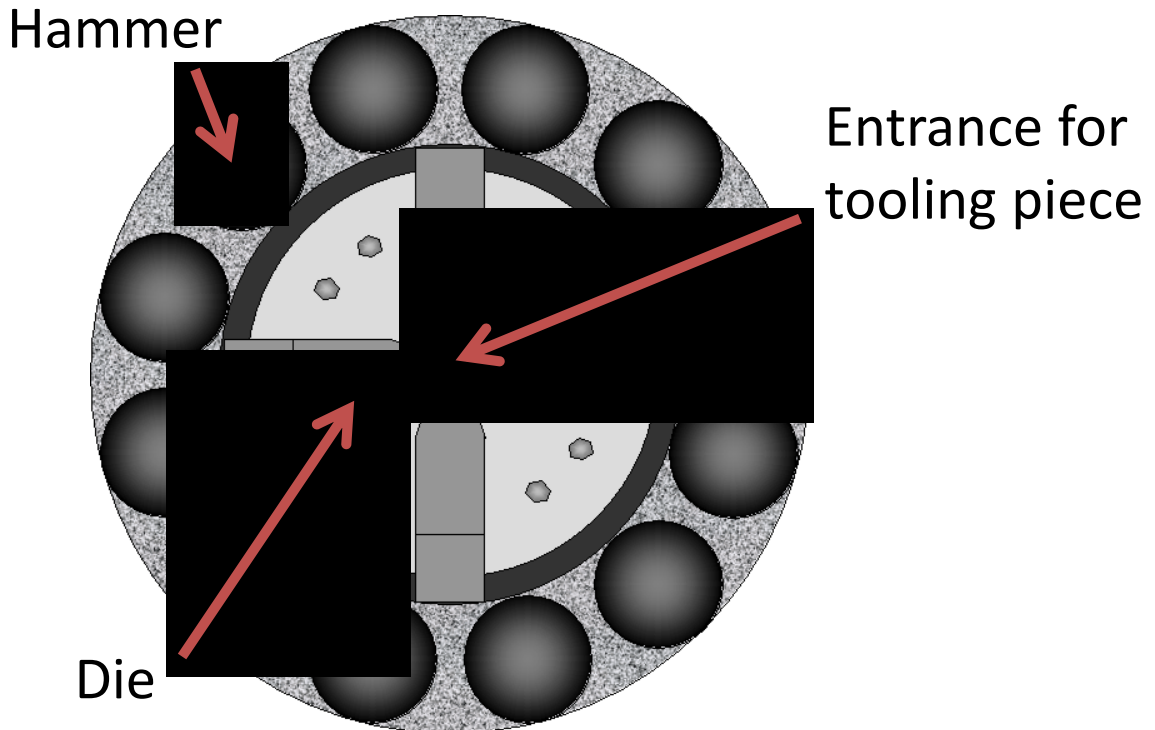


Figure 1.4 Front view of the swager roll-cage. The tooling piece is inserted between the dies, which rotate around and are struck by the hammers on the rollers, forcing them together and reducing the diameter of the tooling piece.

bonds the sheets together making a solid laminate and it reduces the average bilayer thickness in the laminate. The final bilayer thicknesses and distributions are controlled by the initial hardness, strain hardening, and strain-rate hardening of the materials that are rolled together [25–27]. For example, if fully annealed Ni and Al are rolled together, Al preferentially deforms as it is the softer phase. After more rolling passes, the Al hardens through an increase in its dislocation density and the Ni begins to neck and break up. After many more passes, the Al has hardened enough to force the Ni to deform as well, and a quasi-layered microstructure is formed. However, when two materials are rolled with a different hardness cracks can be generated since one phase will resist deformation more than the other. These cracks tend to run perpendicular to the rolling direction and become more prevalent as the extent of rolling increases. If two materials with a similar hardness and strain hardening behavior like Al and Pd are rolled together, the two materials deform at the same rate, forming a relatively uniform microstructure and few cracks [38].

In addition to rolling elemental sheets, swaging of elemental powders or rolled sheets packed in steel tubes can be used to fabricate reactive rods [24]. In contrast to rolling, the differences in material hardness cause far less cracking during swaging since it is a 2-D compressive technique. There is break-up of Ni into a matrix of Al, though, and the strain imparted during the swaging process is radially dependent, with the outer areas of the tooling piece have more strain imparted than the inner core. This variation in strain with radius can lead to porosity in the center of the final product [39].

Mechanical processing of RM has many advantages. High material utilization as well as low capital costs makes mechanical processing highly attractive for bulk

fabrication. In addition, swaging is highly attractive for processing materials that cannot easily be sputtered due to low efficiencies or magnetic challenges such as B or Ni. Like other mechanical processing methods, the degree of compaction during swaging will serve to reduce the average diffusion distance between reactants (easing atomic diffusion) but also increase the total packing density of the composite (easing thermal transport).

### **1.3 Uses for RM**

Applications for RM have drawn on the ability to control the heat released during reaction, as well as the rate at which the reaction propagates. Typical applications include the use of a reactive material as a heat source for joining, thermal batteries and advanced munitions. Other applications include their use in delays [40,41] for the mining and defense industries and their use in producing near net-shaped intermetallics [42]. The following sections focus on three applications in particular – joining, chemical delays and reactive fragments.

#### **1.3.1 Bonding with RM**

Currently, one of the most active applications of reactive materials is their use in foil form as a heat source designed to melt solder between two planar surfaces and bond the respective components [43–45]. (See Figure 1.5) The flat and brittle nature of sputtered reactive foils, though, is not well-suited for bonding curved or otherwise irregularly-shaped surfaces. However, reactive laminate or composite powders could be sprinkled and pressed between the two pieces to be bonded and reacted. A challenge for

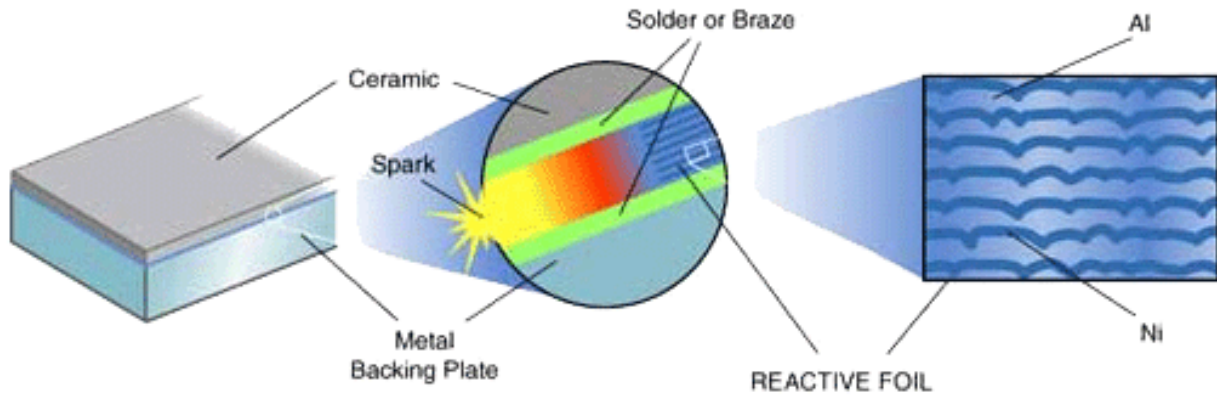


Figure 1.5 Schematic of a reactive foil used to bond two materials together that have been coated with solder or braze. The reactive foil rapidly heats the solder or braze and melts it, allowing two materials that are typically not able to be soldered together, such as ceramics.

this alternative material form is an increased risk of quenching due to the many reignition steps that must take place for full propagation.

An ideal material system that would accomplish this would need a high temperature of reaction, react in the solid state to avoid spraying solder and be resistant to quenching as the reaction propagates between particles. Preliminary studies have found that Ni/Al particles sprinkled and pressed between two planar surfaces do not enable a self-propagating reactions under load and quench with an applied pressure of 100 PSI. Additional investigations will be needed to identify superior particle chemistries with both a higher temperature of reaction and a reduced propensity to quenching.

### 1.3.2 Reactive Fragments

Reactive fragments are designed to deliver more energy to a given target than a

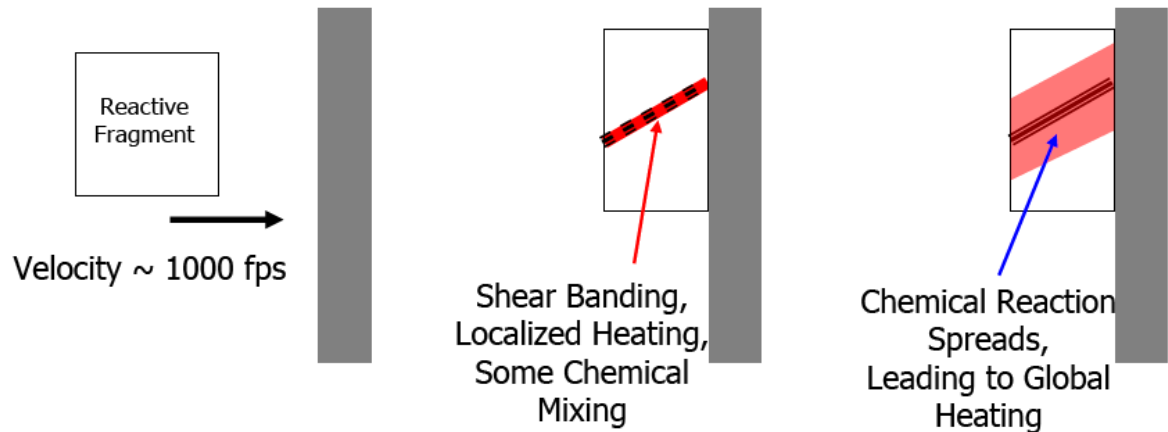


Figure 1.6 Chain of events when a reactive fragment strikes a target. First, the rapid deformation starts chemical mixing and localized reaction. As the reaction spreads throughout the fragment, it begins to globally heat, delivering more energy to the target than a traditional steel fragment.

conventional, inert steel or tungsten fragment by enabling a chemical reaction following impact [46,47]. Ideally the chemical reaction releases as much or more energy than the kinetic energy that is delivered by conventional, inert fragments. Measuring the energy delivered to a target upon impact is challenging. Currently, large-scale tests are typically performed by measuring the quasi-static pressure rise that results after a fragment passes through a 1/16" steel sheet, enters a steel chamber and then strikes an anvil [48]. Fragment velocities can range from low values of 300m/s to high values of 3000 m/s. The rapid plastic deformation that follows impact is thought to trigger shear banding and localized heating that then leads to the initiation of a chemical reaction (See Figure 1.6.)

The rapid plastic deformation that occurs on impact should trigger an intermetallic reaction in the laminate particles, even at low impact velocities. The heat of the intermetallic reaction could then be used to drive oxidation of fuel particles that can

be included in the reactive fragment. Alternatively, in an ideal scenario, the intermetallic compounds that form within the laminate particles will also oxidize and thereby deliver two to five times more energy than simply the formation reaction. Consider, for example, a 1 g piece of steel that strikes a wall at 1000 m/s and delivers kinetic energy equal to  $\frac{1}{2}mv^2$  which is 500 J. If the fragment were instead made of a Ni/Al laminate composite, it would deliver 500 J from kinetic energy and an additional 1,390 J of chemical energy due to the formation of the NiAl intermetallic from the elemental reactants. If the NiAl intermetallic oxidizes as well, an additional 12,100 J will be released, which is a twentyfold increase over the energy delivered by a standard steel fragment. Expanding this example further, if a 1g compact consisting of 0.3 g of Ni/Al, 0.5 g of Al and 0.2g of W strikes a wall it would release 405 J from the NiAl intermetallic formation and 15,500 J from Al oxidation [49]. If the intermetallic then oxidized it would release another 2575 J of energy, releasing almost 19,000 J of energy. This marks an improvement of almost 40 times over only the kinetic energy of a standard steel fragment.

When considering replacing steel with a reactive material in fragments, several factors must be considered. A successful candidate material must have a density similar to steel to maintain the same component mass, be stable through launch, sensitive enough to react upon impact and deliver a substantial and sustained rise in local pressure through heating. Ideally, an intermetallic component such as Ni/Al reactive laminate powders to serve as an initiator, fuel powders susceptible to oxidation such as Zr or an Al-Mg alloy and dense powders such as W. These components could be combined together in a loose compact and swaged inside of a steel tube to form a fully dense compact.

### 1.3.3 RM Delays and Fuses

Reactive materials that incorporate transition metals and light elements such as Al, C, B or Si could be incorporated into delays and fuses for mining and munitions to replace toxic lead azides and thereby offer an environmentally friendly alternative. To be able to compete with state-of-the-art delays and fuses, a successful candidate material needs to have a velocity that can be finely tuned to generate accurate delays of microseconds to several seconds. For quick delays, reactive RM foils are ideal geometries as their high thermal diffusivity allows for very quick reaction velocities. However, for longer delays, foil bilayer lengths associated with very slow reaction velocities propagate in an unsteady manner and are prone to quenching [50]. Therefore, a new geometry is needed if RMs are to be viable delay candidates.

If many reaction interrupts can be incorporated into traditional geometries by using powders or particles instead of rods or foils, the reaction velocities can be slowed by an order of magnitude or more. Previous research has shown that the time of thermal ignition is roughly 200 times slower than the reaction propagation time in the three step propagation sequence [51] (Shown schematically in Figure 1.7.) Thus, reactive laminate powders have an additional way other than the average bilayer to control reaction velocity: the particle packing fraction and the thermal resistance of the particle-particle interface. This means that both the rate of atomic diffusion within particles and the rate of thermal diffusion between the particles can be independently tuned and this RM geometry holds promise for delay and fuse applications.

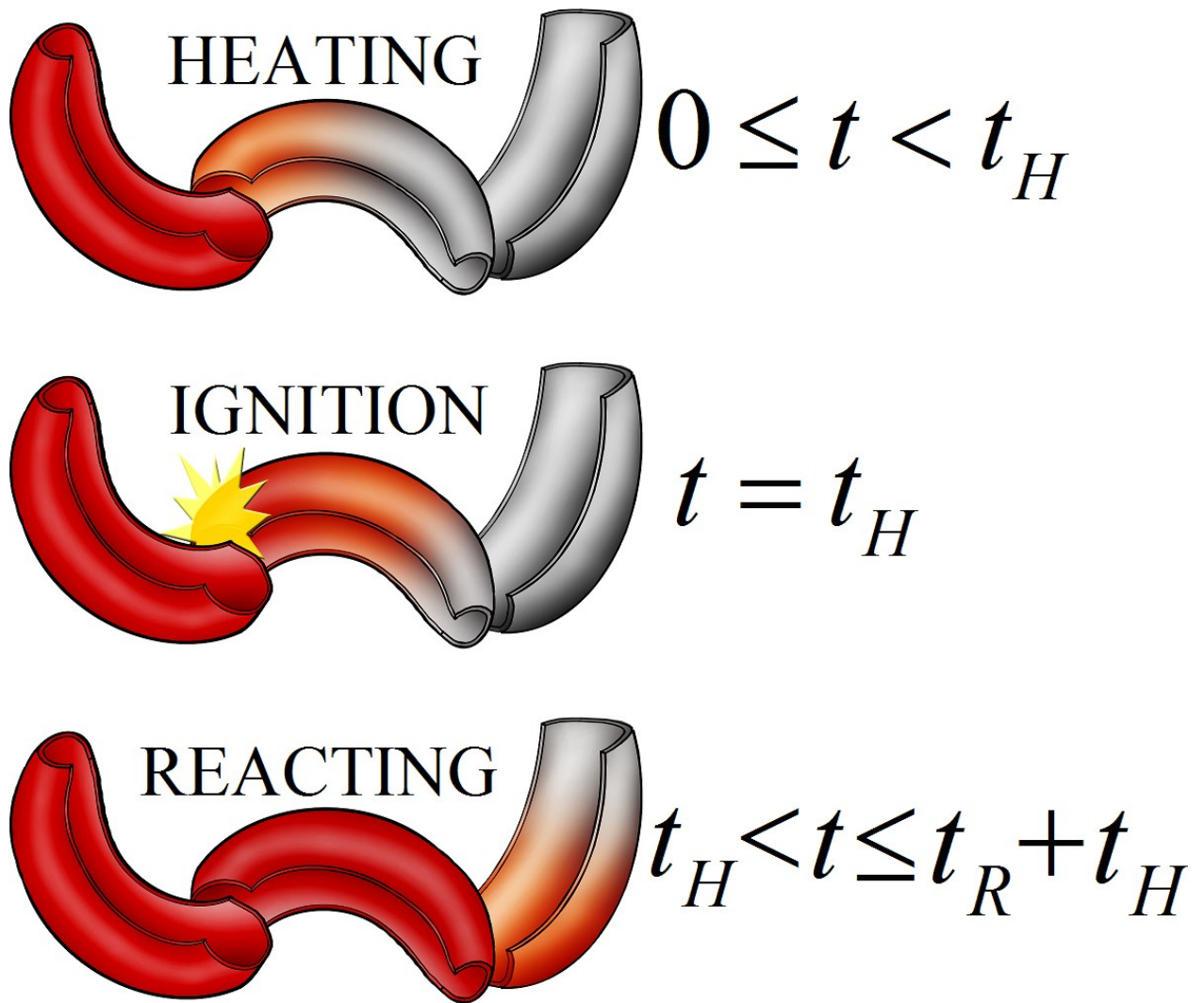


Figure 1.7 Process of particle reaction propagation when the particles are self-contained systems where only chemical diffusion happens within the particle and thermal energy is transferred to the next particle. Eventually the heat from the reacting particle heats the next one in the chain, which begins the cycle anew.

## References

- [1] Weihs TP. Self-propagating Reactions in Multilayer Materials, in: Handbook of Thin Film Process Technology. Bristol: TOP; 1998.
- [2] Floro JA. Journal of Vacuum Science & Technology A: Vacuum, Surfaces, and Films 1986;4:631.
- [3] Gavens AJ, Heerden D Van, Mann AB, Reiss ME, Weihs TP. Journal of Applied Physics 2000;87:1255.
- [4] Ma E, Thompson C V., Clevenger LA, Tu KN. Applied Physics Letters 1990;57:1262.
- [5] Anselmi-Tamburini U, Munir ZA. Journal of Applied Physics 1989;66:5039.
- [6] Wickersham CE. Journal of Vacuum Science & Technology A: Vacuum, Surfaces, and Films 1988;6:1699.
- [7] Dyer, T S, Munir, Z A, Ruth V. Scripta Metallurgica et Materialia 1994;30:1281.
- [8] Reiss ME, Esber CM, Van Heerden D, Gavens AJ, Williams ME, Weihs TP. Materials Science and Engineering: A 1999;261:217.
- [9] Rogachev AS, Grigoryan AÉ, Illarionova E V., Kanel IG, Merzhanov AG, Nosyrev AN, Sachkova N V., Khvesyuk VI, Tsygankov PA. Combustion, Explosion, and Shock Waves 2004;40:166.
- [10] Rogachev AS. Russian Chemical Reviews 2008;77:21.
- [11] Goldschmidt H. Iron Age 1908;82:232.
- [12] Moore JJ, Feng HJ. Progress in Materials Science 1995;39:243.
- [13] Eslamloo-Grami M, Munir ZA. Material Science Report 1989;3:227.
- [14] Merzhanov AG. Combustion and Plasma Synthesis of High-Temperature Materials. Weinheim: VCH; 1990.
- [15] Boer RF, Boom R, Mattens WCM, Miedema AR, Niessen AK. Cohesion in Metals. Amsterdam: Elsevier Ltd; 1988.
- [16] Salloum M, Knio OM. Combustion and Flame 2010;157:1154.
- [17] Salloum M, Knio OM. Combustion and Flame 2010;157:288.
- [18] Salloum M, Knio OM. Combustion and Flame 2010;157:436.

- [19] Scobey M, Seddon RI, Seeser JW, Austin RR, LeFebre PM, Manley BM. Magnetron Sputtering Apparatus and Process, n.d.
- [20] Kelly P., Arnell R. Vacuum 2000;56:159.
- [21] Barron SC, Wysk N, Weihs TP. In Preparation n.d.
- [22] Govindarajan RM, Aravas N, Mechanics A. 1994;36:343.
- [23] Helle a. S, Easterling KE, Ashby MF. Acta Metallurgica 1985;33:2163.
- [24] Gibbins JD, Stover AK, Krywopusk NM, Woll K, Weihs TP. In Preparation n.d.
- [25] Hebert RJ, Perepezko JH. Scripta Materialia 2003;49:933.
- [26] Hebert RJ, Perepezko JH. Materials Science and Engineering: A 2004;375-377:728.
- [27] Hebert RJ, Perepezko JH. Scripta Materialia 2004;50:807.
- [28] Saito Y, Utsunomiya H, Tsuji N, Sakai T. Acta Materi 1999;47:579.
- [29] Park JS, Lim HK, Kim J-H, Park JM, Kim WT, Kim DH. Journal of Materials Science 2005;40:1937.
- [30] Mozaffari A, Danesh Manesh H, Janghorban K. Journal of Alloys and Compounds 2010;489:103.
- [31] Eizadjou M, Kazemi Talachi A, Danesh Manesh H, Shakur Shahabi H, Janghorban K. Composites Science and Technology 2008;68:2003.
- [32] Qiu X, Liu R, Guo S, Graeter JH, Kecskes L, Wang J. Metallurgical and Materials Transactions A 2009;40:1541.
- [33] Battezzati L, Pappalepore P, Durbiano F, Gallino I. Acta Materialia 1999;47:1901.
- [34] Trunov M a, Umbrajkar SM, Schoenitz M, Mang JT, Dreizin EL. The journal of physical chemistry B 2006;110:13094.
- [35] Bazyn T, Glumac N, Krier H, Ward TS, Schoenitz M, Dreizin EL. Combustion Science and Technology 2007;179:457.
- [36] Badiola C, Schoenitz M, Zhu X, Dreizin EL. Journal of Alloys and Compounds 2009;488:386.
- [37] Dreizin EL. Progress in Energy and Combustion Science 2009;35:141.
- [38] Bordeaux F, Yavari R. Z Metallkde 1990;81:130.
- [39] Li R, Zou-ren N, Tie-yong Z. Trans Nonferrous Met Soc China 2006;16:1015.

- [40] Baginsky TA, Parker TS, Fahey WD. Electro-explosive Device with Laminate Bridge. U.S. Patent 6,421,071, n.d.
- [41] Baginsky TA, Talioferro SL, Fahey WD. Journal of Propulsion and Power 2001;17:184.
- [42] Morsi K. Materials Science and Engineering: A 2001;299:1.
- [43] Swiston AJ, Hufnagel TC, Weihs TP. Scripta Materialia 2003;48:1575.
- [44] Duckham A, Spey SJ, Wang J, Reiss ME, Weihs TP, Besnoin E, Knio OM. Journal of Applied Physics 2004;96:2336.
- [45] Wang J, Besnoin E, Knio OM, Weihs TP. Acta Materialia 2004;52:5265.
- [46] Montgomery HE. Reactive Fragment. U.S. Patent 375,246, n.d.
- [47] Truitt RM, Nielson DB, Ashcroft BN, Braithwaite PC, Rose MT, Cvetnic MA. Weapons and Weapon Components Incorporating Reactive Materials and Related Methods. U.S. Patent 11/512058, n.d.
- [48] Lee RJ, Mock W, Carney JR, Holt WH, Pangilinan GI, Gamache RM, Boteler JM, Bohl DG, Drotar J, Lawrence DG. AIP Conference Proceedings, in: 2006.
- [49] Fischer SH, Grubelich MC. A Survey of Combustible Metals, Thermites, and Intermetallics for Pyrotechnic Applications, in: Lake Buena Vista: 1996.
- [50] Jayaraman S, Mann AB, Reiss M, Weihs TP, Knio OM. Combustion and Flame 2001;124:178.
- [51] Fritz GM, Joress H, Weihs TP. Combustion and Flame 2011;158:1084.

## Chapter 2 Fabrication and Characterization of Ni/Al Reactive Materials

### 2.1 Fabrication of Rolled Ni/Al Laminates

The foils in this study were fabricated by rolling alternating sheets of 25  $\mu\text{m}$  thick 6061 T6 Al and 18  $\mu\text{m}$  thick fully annealed 201 Ni from All-Foils Inc. and were stacked after cleaning with ethanol to create a loose multilayer structure. They were rolled at room temperature to achieve a 50% thickness reduction as shown schematically in Figure 2.1. The initial layer thicknesses correspond to a nominal chemistry of 52 at% Ni and an initial bilayer thickness of 43  $\mu\text{m}$ . The severe plastic deformation

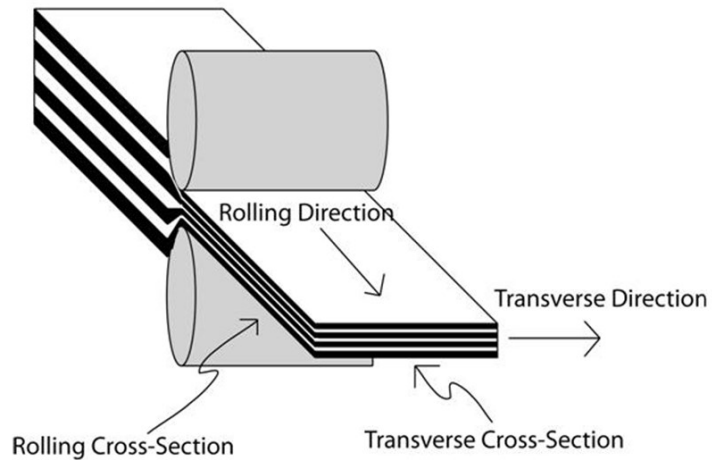


Figure 2.1: Cold-Rolling Process. Initially loose foils were stacked and passed through the rolling mill to achieve a 50% thickness reduction which bonds the foils together and also reduces their thickness. Subsequent passes were accomplished by cutting and restacking two laminate foils, after edge cracks were trimmed. Both the rolling and transverse cross-sections are highlighted.

during the rolling process reduces the thickness of the layers and bonds the individual foils together. After one rolling pass, the foils were cut, restacked and rerolled to achieve either three, six or nine 50% thickness reductions. In addition, some foils were rolled

further using six 20% thickness reductions but without cutting and restacking. The six 20% reductions are equivalent to two 50% thickness reductions. We refer to the final foils using the number of initial 50% thickness reductions and the number of additional

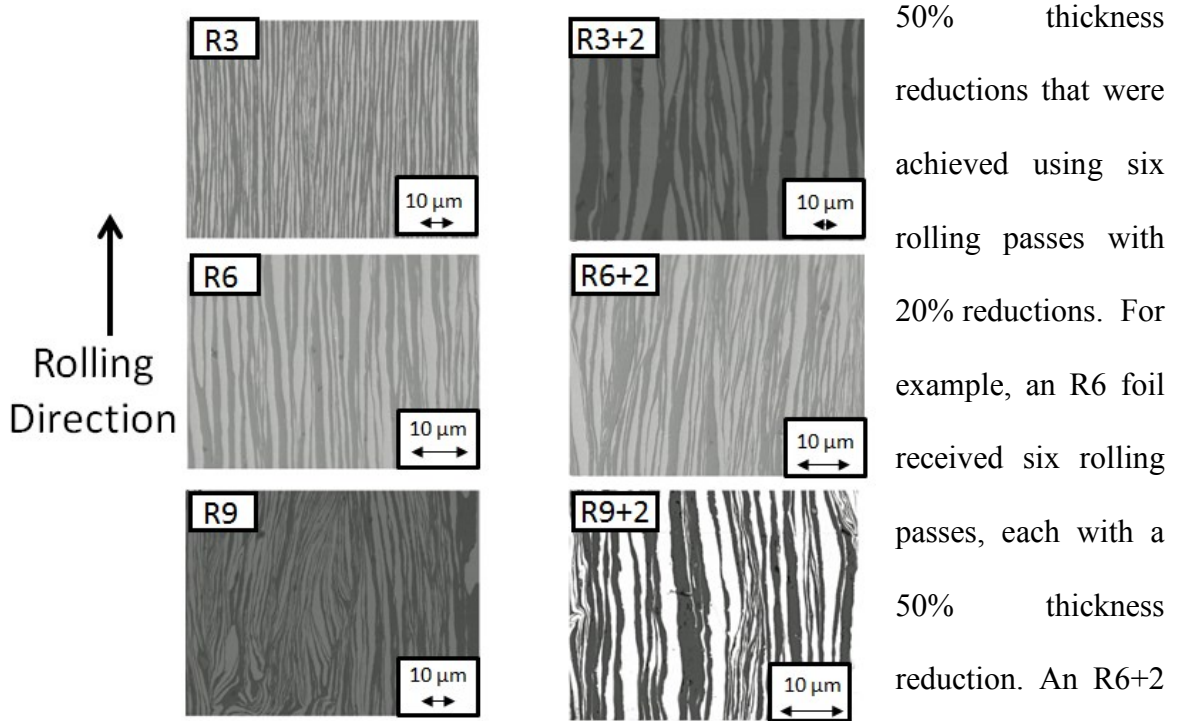


Figure 2.2 Cross-sectional SEM images of microstructures in the six cold-rolled samples. Each image is a transverse cross section.

See Figure 2.2 for typical SEM cross-sectional images of the microstructure for all the samples.

## 2.2 Fabrication of Ni/Al Composite Powders

R6+2, R8+2 and R10+2 foils were broken up by hand, blended in a Blend-Tec blender for 90 seconds, and then the resulting powders were sieved to 850-500 μm, 500-

355  $\mu\text{m}$ , 355-212  $\mu\text{m}$ , 212-150  $\mu\text{m}$ , 150-106  $\mu\text{m}$  and 106-53  $\mu\text{m}$  size ranges. Figure 2.3 shows the powder fabrication schematic.

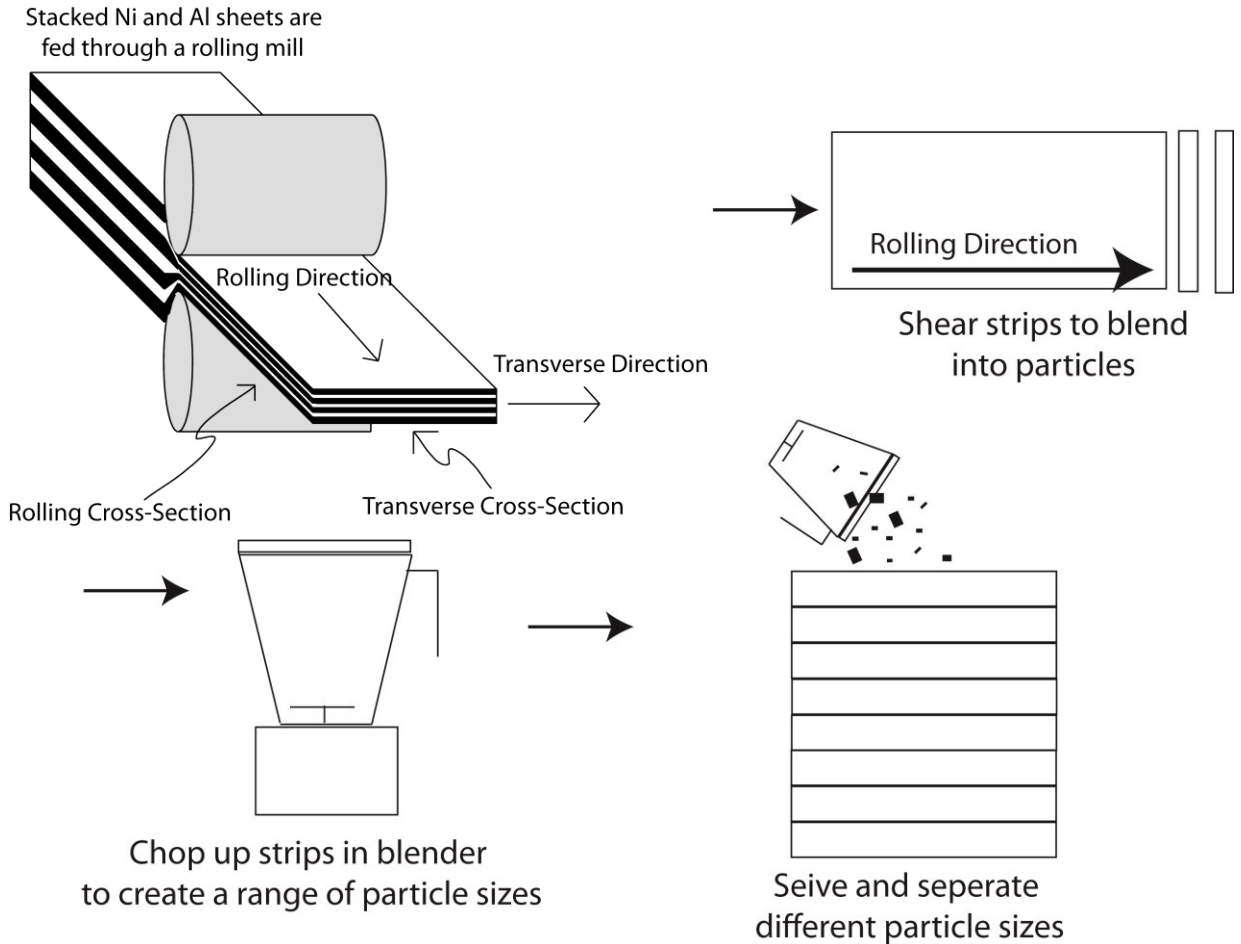


Figure 2.3 In the first stage of powder fabrication, reactive laminates are created by cold-rolling altering sheets of Al and Ni with a 50% thickness reduction. This first rolling pass bonds the sheets through plastic deformation to create a solid composite. After this first 50% thickness reduction, the composite is cut in half, restacked, and rolled back together, further refining the microstructure. Additionally, after 6, 8 or 10 50% thickness reductions, an additional 6 passes are performed at 20% thickness reduction per pass with no stacking. The foils are then broken by hand and ground in a blender for 90 seconds to generate a range of particle sizes. The particles are then sieved into powder size ranges that vary from 850  $\mu\text{m}$  to 53 $\mu\text{m}$ .

## **2.3 Characterization Techniques**

### **2.3.1 Scanning-Electron Microscopy**

Rolled samples were mounted in Buehler epoxy exposing a rolling or a transverse cross-section (Figure 2.1) and the samples were polished with 340 grit sandpaper followed by 9 and 3  $\mu\text{m}$  suspensions of diamond as well as a 0.05  $\mu\text{m}$  silica suspension. As Ni and Al have different hardnesses, the polishing steps should be performed with a low load (typically 1N/sample) and with a complimentary rotation direction. Also, polishing techniques should be used that preferentially cut and remove the sample rather than smearing it away, so sandpaper should only be used for the coarsest grinding step. The polished samples were imaged in a JEOL JSM-6700F scanning electron microscope (SEM.) In addition, the individual Ni and Al layer chemistries had their chemistries analyzed with Electron Dispersive Spectroscopy (EDS.) The Ni layer had no trace components, and the Al layer had a chemistry of 97at %/3 at% Al/Mg, due to the Mg in the 5052 alloy.

### **2.3.2 Differential Scanning Calorimetry**

A Perkin-Elmer Pyris 1 differential scanning calorimeter (DSC) was used to measure the material heat of reaction. 10 mg of sample were sealed inside disposable Cu pans and heated from 50  $^{\circ}\text{C}$  to 725  $^{\circ}\text{C}$  at 40  $^{\circ}\text{C}/\text{min}$ . The first scan is used to identify exotherms generated by irreversible formation reactions and the second is used as a baseline and subtracted from the first to determine the net heat flow [1]. Symmetric x-ray diffraction was performed on samples quenched immediately after each exothermic peak to determine the corresponding phase transformations. The enthalpy of formation literature value for the B2 NiAl intermetallic is 1380 J/g [2] however the diffusion

distances in the rolled Ni/Al composites are much larger and do not fully react during DSC scans. Therefore, we observe that materials with more rolling passes release more energy (see Chapters 4-6); however this is due to the temperature limitation of the DSC and is not physically significant.

### **2.3.3 Gas Pycnometry**

A combination of microbalance measurements and gas pycnometry were used to determine physical density. Roughly 5g of powders or foil were placed in a Micromeritics Accu-Pyc II 1340 He gas pycnometer, which uses He gas expansion to determine the displaced volume. A load pressure of 19.5 psi was used.

### **2.3.4 Velocity and Maximum Temperature Measurement**

Radiant light from the reaction front was collected with optical fibers spaced 2-5 cm apart along the strip length and sent to a two-color pyrometer or photodiodes for analysis of the maximum temperature and reaction velocity, respectively, as reported in [3]. Unsteady reaction propagation was captured using a Photron SA5 fast-cam at 50,000 frames per second and a 1  $\mu$ s shutter speed. The reaction fronts were imaged with a top-down view. The high-speed videos were analyzed using Tracker, a freeware program, with an overlaid scale bar taken from a photo before reaction.

### **2.3.5 Mechanical Testing**

Cold-rolled Ni/Al laminates were milled into dogbone samples according to ASTM standards [4]. The dimensions (in inches) are shown in Figure 2.4. Samples were loaded into an Instron 5582 load frame with an Instron 2630-121 extensometer clipped onto the gauge section during the test. A strain rate of  $10^{-4}$  was used, and all samples

were cut perpendicular to the rolling direction to minimize the role of cracks on test results.

Hardness tests were performed using a LECO Vickers microindenter using a 300g load and a square pyramidal tip. Indents were done parallel to the layers and were large enough to sample multiple layers of both Ni and Al.

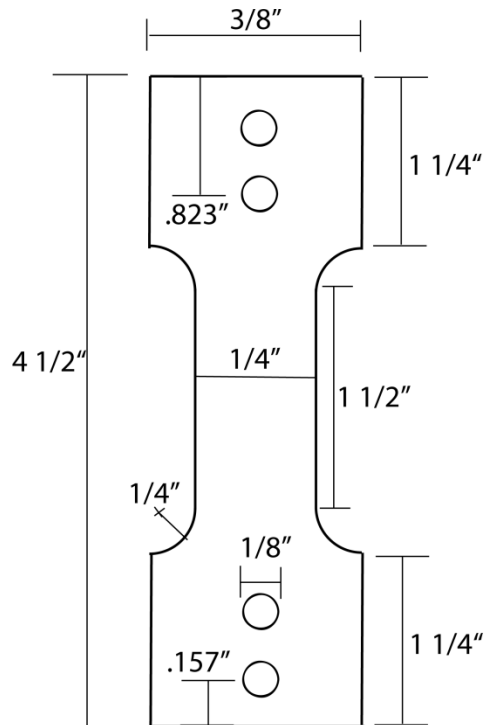


Figure 2.4 Dogbone specimen schematic. All dimensions are in inches. The two holes are used for gripping the sample into the Instron load frame.

## References

- [1] Michaelsen C, Barmak K, Weihs TP. *Journal Physics D; Applied Physics* 1997;30:3167.
- [2] Boer RF, Boom R, Mattens WCM, Miedema AR, Niessen AK. *Cohesion in Metals*. Amsterdam: Elsevier Ltd; 1988.
- [3] Barron SC, Knepper R, Walker N, Weihs TP. *Journal of Applied Physics* 2011;109:013519.
- [4] ASTM E8/E8M - 11 *Standard Test Methods for Tension Testing of Metallic Materials*. West Conshohocken: International, ASTM; 2005.

# Chapter 3 Mechanical Properties of Cold-Rolled Ni/Al Laminates

## 3.1 Introduction

Reactive materials (RMs) have the potential to be incorporated into traditional projectiles in the form of reactive casings or fragments to add chemical energy on impact [1–3]. For these materials to be viable reactive fragment candidates, they must exhibit a host of properties, such as a high energy density, a density similar to steel ( $\sim 7 \text{ g/cm}^3$ ), and an ability to react on impact at relatively low impact velocities. While energy density is important in RMs, it is becoming apparent that strength and mass density could be a limiting factor in determining which RMs hold promise as weapons additions [1–3]. Previous research has shown that RM effectiveness depends strongly on mass density due to the momentum gained from the blast impact, but only weakly on reactivity (beyond a threshold value [4].)

NiAl composites have both a moderate mass density ( $\sim 5.2 \text{ g/cm}^3$ ) and a moderate energy density (1,380 J/g for NiAl formation [5],  $\sim 6,200 \text{ J/g}$  for NiAl oxidation.) However, compared to the industry standard aluminum/Teflon composite, RM4, they have a high density and elastic modulus, therefore they are the focus of static tensile testing in this study [3]. Furthermore, these materials could be incorporated into a composite reactive fragment that includes a metallic fuel (such as Al, Al/Mg alloy or Zr) and a density enhancer (such as Ta or W.)

Mechanical methods for the fabrication of RM hold promise because the deformation process should increase both the reactivity and the strength as the reactant spacing is reduced [6–10]. For cold-rolling, each additional pass deforms the microstructure, which reduces both the reactant diffusion distance and the dislocation

glide distance. However, the limitations of this technique include the relatively high cost of foils (compared to powders) and the necessity of hardness uniformity for the materials deformed. If one phase is harder than the other, it will resist deformation and cause cracking, impeding uniform layer reduction and negatively influencing the mechanical properties [6–8,11–13].

### 3.2 Experimental Methods

The NiAl laminates used in this study were fabricated via cold-rolling, explained in Chapter 2. However, one laminate set began with 127  $\mu\text{m}$  thick Ni and 178  $\mu\text{m}$  Al foils, and is thus named R3\_127\_178. The other rolling sets began with 18  $\mu\text{m}$  and 25  $\mu\text{m}$  thick Ni and Al foils, respectively, with three, six or nine 50% rolling reductions (R3, R6 and R9.)

Mechanical testing methods are also detailed in Chapter 2.

### 3.3 Results

Table 3.1 Original Ni and Al foil thicknesses and number of rolling passes used to create the composites

| Starting Ni Thickness ( $\mu\text{m}$ ) | Starting Al Thickness ( $\mu\text{m}$ ) | Number of 50% Thickness Reductions | Volume Average Bilayer Thickness ( $\mu\text{m}$ ) |
|---|---|------------------------------------|--|
| 127                                     | 178                                     | 3                                  | 30.+/-11   |
| 18                                      | 25                                      | 3                                  | 14+/-3.2   |
| 18                                      | 25                                      | 6                                  | 5.3+/-1.5  |
| 18                                      | 25                                      | 9                                  | 3.2+/-0.7  |

Table 3.1 shows the four foils fabricated and their volume average bilayer thickness. Foils with more rolling passes or a smaller initial bilayer thickness have a smaller volume average bilayer thickness.

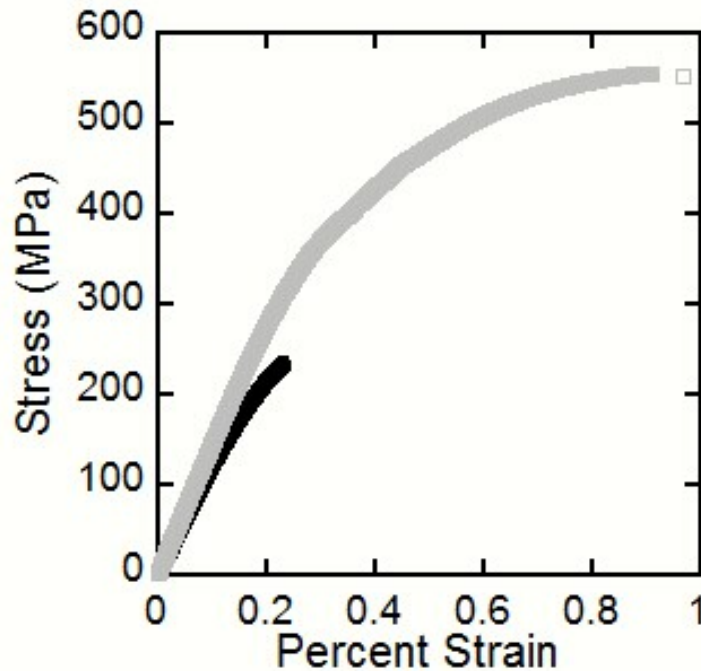


Figure 3.1 Stress/strain curve for two different 127\_178\_R3 samples. Note the large difference in strain before fracture, as well as the tensile strength.

Figures 3.1 and 3.2 show sample stress/strain curves for samples both an initial 43  $\mu\text{m}$  and 305  $\mu\text{m}$  bilayer. Figure 3.3 shows the tension test results for the four laminates as a function of volume average bilayer thickness. The material with the coarsest microstructure (127\_178\_R3) had the highest strength while the other materials either had a strength around 100 MPa or broke in the gripped section.

In addition to tensile tests, Vickers microhardness tests were performed on mounted and polished samples, with the results shown in Figure 3.4 labeled as

“Microhardness.” R9 has the highest hardness, followed by 127\_178\_R3, R6 and R3.

Figure 3.4 also shows the estimated yield strengths based on the Tabor relation [14],

labeled as “Yield Strength.”

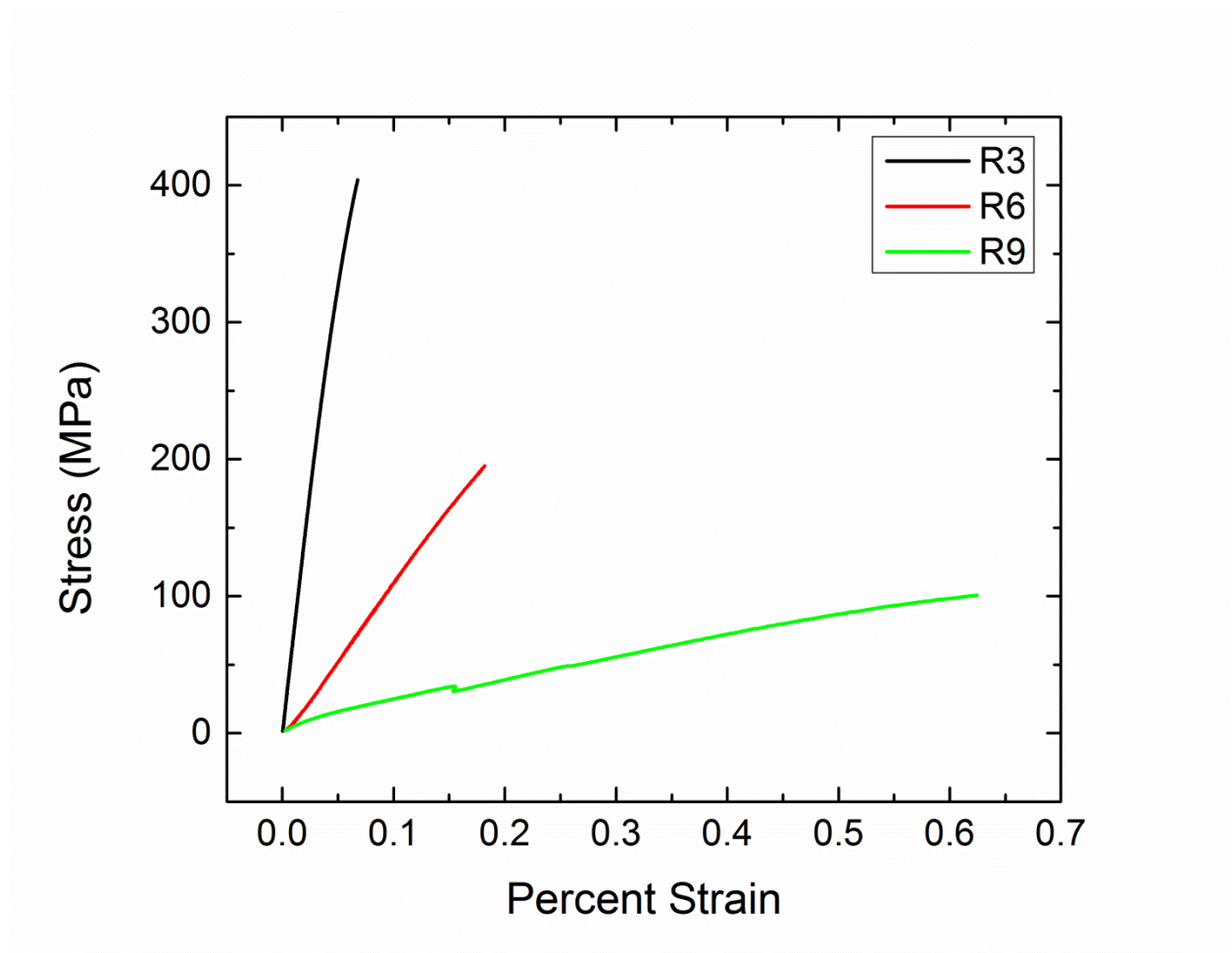


Figure 3.2 Stress/strain curve for samples with an initial bilayer of 43  $\mu\text{m}$ . Note the large difference in modulus and maximum strength

### 3.4 Discussion

The mechanical behavior of the cold-rolled laminates should be governed by two hardening parameters, the total amount of strain during rolling (increases dislocation density) and the volume average bilayer thickness (which impedes dislocation motion

through the interface.) Therefore, we expect that the strength to be highest for the materials with the most rolling passes [6–13]. However, the bulk tensile strengths

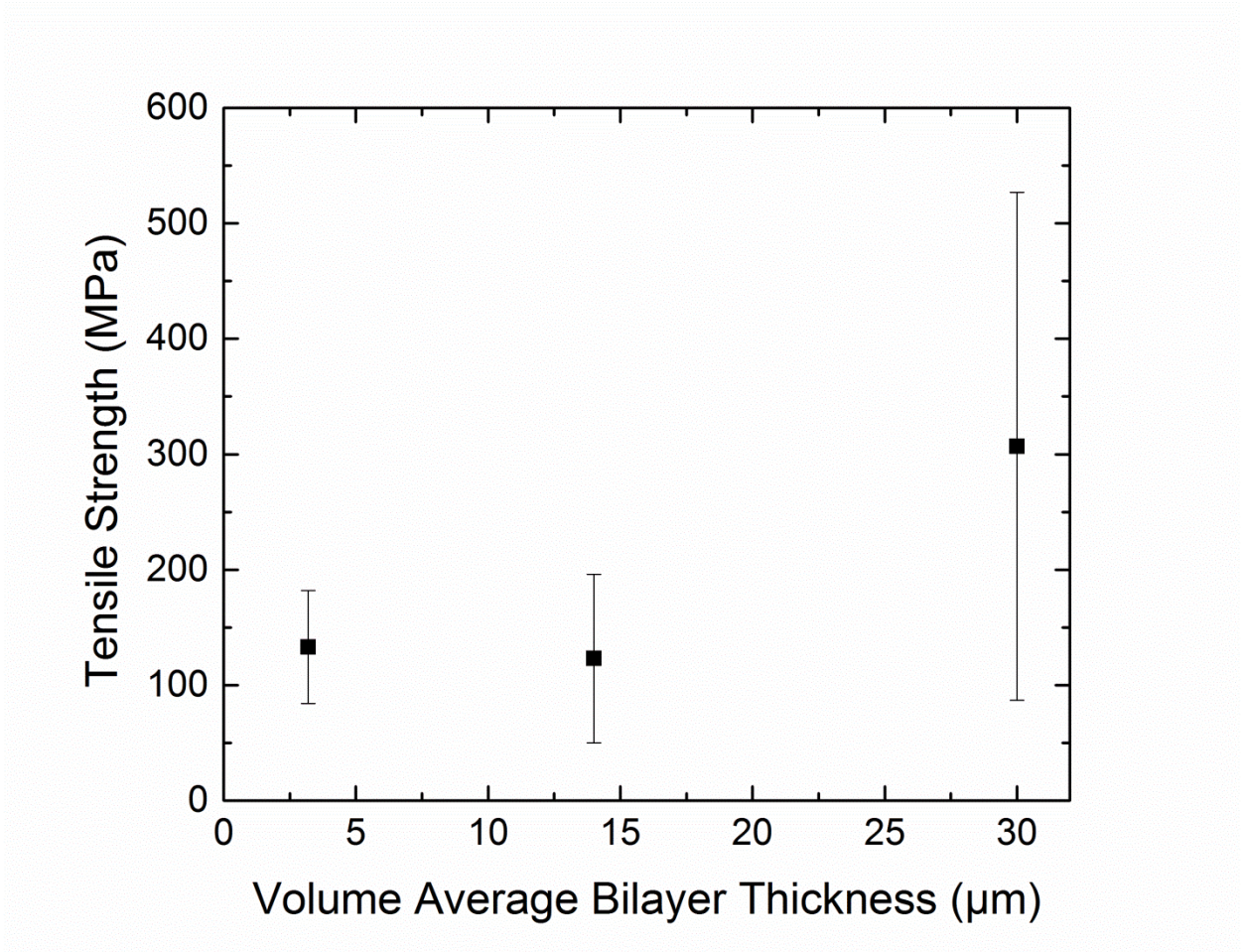


Figure 3.3 Compilation of tensile test data. Note the large standard deviations for the 127\_178\_R3 laminates due to cracks in some of the samples. The other samples have strengths much lower than their processing conditions would predict, which we attribute to many cracks in the sample. R6 samples broke in the grip region, which invalidates the strength data gathered.

(Figure 3.1) do not show this trend, as the material with the highest strength, 127\_178\_R3 has only 3 rolling passes and the largest volume average bilayer thickness. We attribute this behavior to the presence of cracks from the rolling process and fracture before yield. The density of cracks appears to increase with a smaller starting foil thickness and the number of rolling passes. Very few of the samples show any plasticity

before breaking, so a fracture strength is measured due to the latent cracks rather than the true tensile strength. Fracture strength can be measured in all cases but not yield. Figures 3.1 and 3.2 show different stress/strain curves for all samples. The gray curve in Figure 3.3 shows 1% plasticity before breaking, while the sample represented by the black curve broke with only 0.2% strain. The black curve in Figure 3.4 is for R3, which shows the highest strength but the lowest yield before failure. R6 is depicted by the red curve, and has the intermediate strength and yield before failure while R9, shown in green has the highest yield before failure but the lowest strength. Furthermore, the scatter in the tensile strength is significant (Figure 3.3), again signifying that the strength is controlled by a distribution of cracks. If one sample is relatively crack-free, it will support higher stresses and more plasticity than samples with more cracks, particularly large cracks. The R3, R6 and R9 samples are more heavily cracked, reducing their overall strength. The uniform distribution of cracks is thought to limit the scatter in tensile strength as well.

In order to approximate the strength in the absence of cracks, local microhardness tests were performed. The indents sizes were chosen to sample multiple bilayers. For samples that started with 18  $\mu\text{m}$  thick Ni and 25  $\mu\text{m}$  thick Al foils, the hardness tests show the expected strength trend as R9 has the highest hardness while R3 has the lowest. Interestingly, the hardness for the 127\_178\_R3 is just below that of R9, even though its extremely large volume average bilayer thickness suggests that it would have the lowest hardness of all the materials. This surprising result may be due to the hardness of the initial Al and Ni foils being different than those used for the other foils.

Given the rolling process generates cracks due to the differing hardnesses of Ni and Al, fabricating bulk quantities of RM for reactive fragments via rolling is not ideal. One way to remediate this is to break the foils into powders and then recombine them alone or with additional elements to enhance their reactive properties via swaging. The grinding process and the subsequent powders are discussed in-depth in Chapter 5.

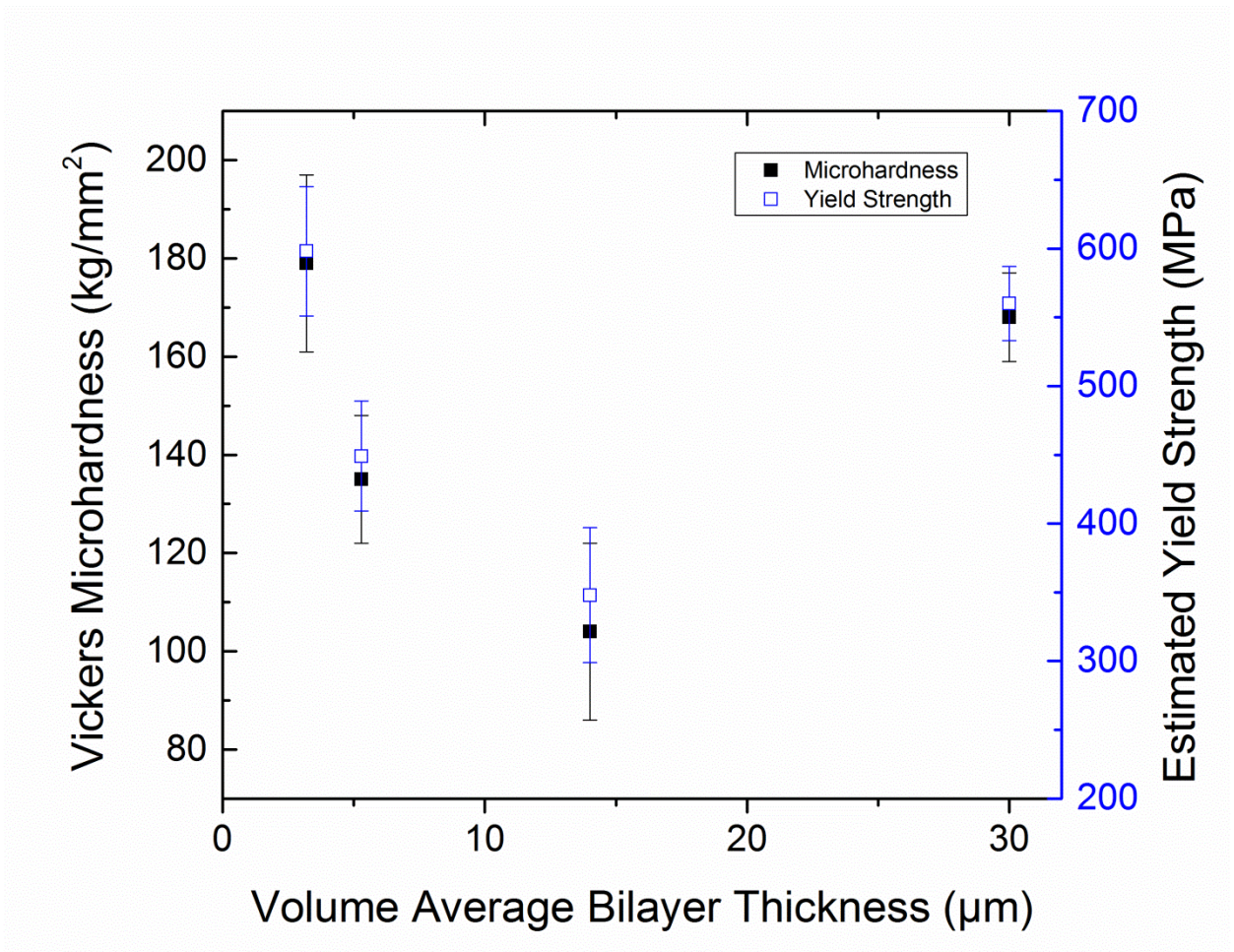


Figure 3.4 Hardness and estimated yield strength for the rolled composites. The hardness values result in more reasonable approximations for the yield strength, as there is an increase for samples with more rolling reductions.

## References

- [1] Montgomery HE. Reactive Fragment. U.S. Patent 375,246, 1976.
- [2] Weihs TP. AE Technical Exchange 2008.
- [3] Ames RG. AE Technical Exchange 2008.
- [4] Fischer SH, Grubelich MC. A Survey of Combustible Metals, Thermites, and Intermetallics for Pyrotechnic Applications, in: Lake Buena Vista: 1996.
- [5] Boer RF, Boom R, Mattens WCM, Miedema AR, Niessen AK. Cohesion in Metals. Amsterdam: Elsevier Ltd; 1988.
- [6] Hebert RJ, Perepezko JH. Scripta Materialia 2003;49:933.
- [7] Hebert RJ, Perepezko JH. Scripta Materialia 2004;50:807.
- [8] Sieber H, Park JS, Weissmüller J, Perepezko JH. Acta Materialia 2001;49:1139.
- [9] Arzt E. Acta Materialia 1998;46:5611.
- [10] Vinci RP, Vlassak JJ. Annual Review of Materials Science 1996;26:431.
- [11] Battezzati L, Pappalepore P, Durbiano F, Gallino I. Acta Materialia 1999;47:1901.
- [12] Dinda GP, Rösner H, Wilde G. Scripta Materialia 2005;52:577.
- [13] Bordeaux F, Yavari AR. Journal of Applied Physics 1990;67:2385.
- [14] Tabor D. The Hardness of Metals. Oxford: 1951.

## **Chapter 4 Microstructure and Properties of Cold-Rolled Ni/Al Laminates**

### **4.1 Introduction**

Laminate composite reactive materials have typically been fabricated with a uniform distance between the two layers using PVD techniques such as magnetron sputtering [1–4] or electron-beam deposition [5–7]. Other investigators, though, have used mechanical methods to compress and bond alternating sheets of metal via rolling, hammering or swaging [8–14]. Furthermore, high-energy ball milling has been used to fabricate composite powders with a discontinuous layered structure [15–18]. In general, bottom-up PVD methods produce more refined and uniform microstructures while top-down mechanical deformations create coarser, nonuniform microstructures. However, microstructural uniformity can be controlled to some degree during mechanical deformation by choosing materials that have similar initial hardnesses and strain hardening rates to encourage uniform layer deformation and to minimize layer pinch-off.

There have been several attempts to link the non-uniform layering in mechanically fabricated laminate composites to their reactive properties. For example, Sieber *et al* [10] reported two exothermic peaks in isochronal differential scanning calorimetry (DSC) tests of 3Al:Ni foils fabricated via cold-rolling. The first DSC peak corresponds to the nucleation and growth of the Al<sub>3</sub>Ni phase along the interface between the Ni and Al layers, and the second peak is attributed to the thickening of the continuous Al<sub>3</sub>Ni intermetallic phase. As the average bilayer decreases, the first peak becomes more

prominent relative to the second one, corresponding to more interfaces in a given volume. Both peaks also shift to lower temperatures reflecting the smaller diffusion distances. Sieber *et al* [10] modeled these peak positions effectively using an average bilayer thickness, but they needed to consider a distribution of layer thicknesses to capture the peak shapes or widths.

Beyond the average bilayer thickness and the numerical distribution of the layer thicknesses, one should also consider the spatial distribution of the layers. Knepper *et al* [1] prepared sputtered foils that contain alternating regions with large and small bilayer thicknesses and found that the velocity of self-propagating reactions in these composite structures can be predicted using a weighted volume average of bilayers if the spatial distribution of the regions with different bilayer thicknesses is relatively narrow. However, such predictions do not hold if the distribution of regions with small and large bilayers is coarse. In this case the small bilayers govern the reaction velocity because the reaction can propagate through them before any significant heat is lost to the regions with large bilayers. The work of Knepper *et al* [1] suggests that studies of non-uniform microstructures should preserve positional information for the constituent layers when quantifying thickness distributions. This, in turn, enables one to determine whether a composite has a coarse or a fine spatial distribution of small and large layers.

This chapter analyzes the distribution of layer thicknesses in cross-sectional images of non-uniformly layered, cold-rolled Ni:Al composites while retaining positional information within the image. The analysis procedure is validated using model images, and it is used to quantify volume average bilayer thicknesses, layer distributions and local and global chemistries as a function of the processing conditions for the Ni:Al laminate

composites. The resulting volume average bilayer thicknesses and distributions of bilayer thicknesses are used to explain shifts in the exothermic peak temperatures and the energy released that were measured using DSC. The layering distributions and local chemistries are also used to predict the properties of self-propagating formation reactions in the Ni:Al laminate composites. Specifically, the maximum temperatures and reaction velocities are predicted and compared to measured values.

## **4.2 Experimental Methods**

### **4.2.1 Materials Fabrication and Characterization**

Ni/Al cold-rolled laminates were fabricated and characterized as described in Chapter 2. The rest of this section details the ‘home-built’ MATLAB code used to quantify the complex microstructure after cold-rolling.

### **4.2.2 Microstructural Analysis**

Twelve to 15 scanning electron microscope (SEM) images of the final microstructure were analyzed for each rolling condition using a numerical code written in MATLAB. Each image contains 964 vertical pixels and 1280 horizontal pixels, with an average of 20-30 bilayers in each image. Our analysis of each sample encompasses approximately 15-19 million pixels that contain 200-300 bilayers, but the thickness of each bilayer is measured up to 964 times as it is tracked throughout the full height of the image. An example image for each of the six rolling conditions is shown in Figure 4.1.

During the bilayer counting process, the local atomic percentage of Ni in a bilayer is also computed by dividing the Ni layer thickness by the thickness of the bilayer that contains that Ni layer and by accounting for the density and atomic weight of both Ni and Al. For pixel rows with a different number of Ni and Al layers, the average of two

bilayers is used to determine a given bilayer thickness by counting from the left and the right of the image, similar to the average bilayer thickness calculation.

The above operations lead to 4 data sets, each of which preserves positional information: the Ni layer thicknesses, the Al layer thicknesses, the bilayer thicknesses and the Ni atomic fractions. These data sets are used to compute the number and volume average layer and bilayer

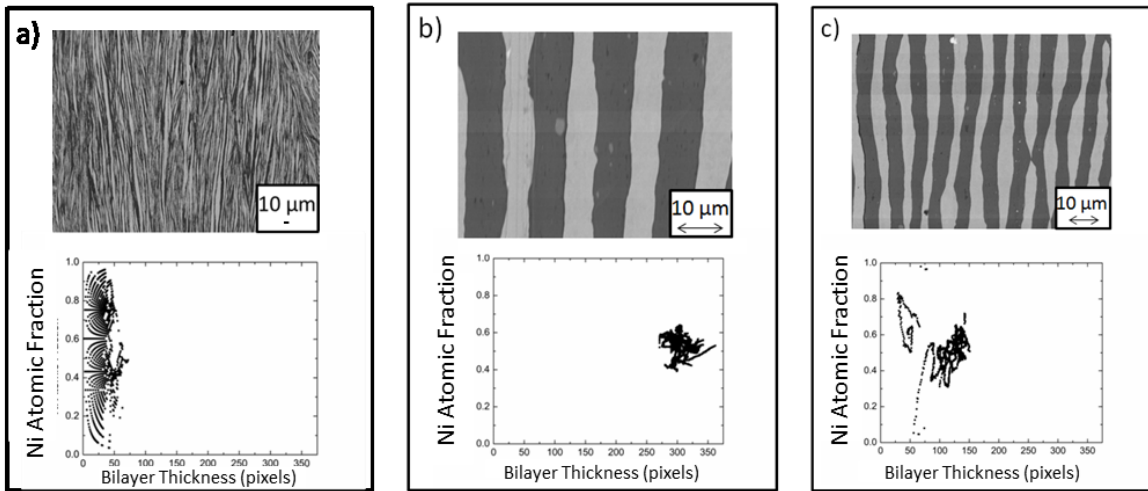


Figure 4.1 Scatterplots of Ni atomic fraction versus bilayer thickness obtained by numerical analysis of three images, a), b) and c). The first image, a), was taken at a low magnification, the second image, b), was taken at a high magnification and c) was taken at a medium magnification. The scatterplots above the images show that when bilayers measure only a few pixels in thickness, the discrete pixel size severely limits the number of possible Ni atomic fractions and the composition data become quantized.

thicknesses. They are also used to calculate the area fraction of bilayers above or below the mean and multiples of the mean (as in twice, three times, etc.). Lastly, the data sets are used to identify clusters of large layers, and the bilayers immediately adjacent to them are examined for both their thickness and their chemistry.

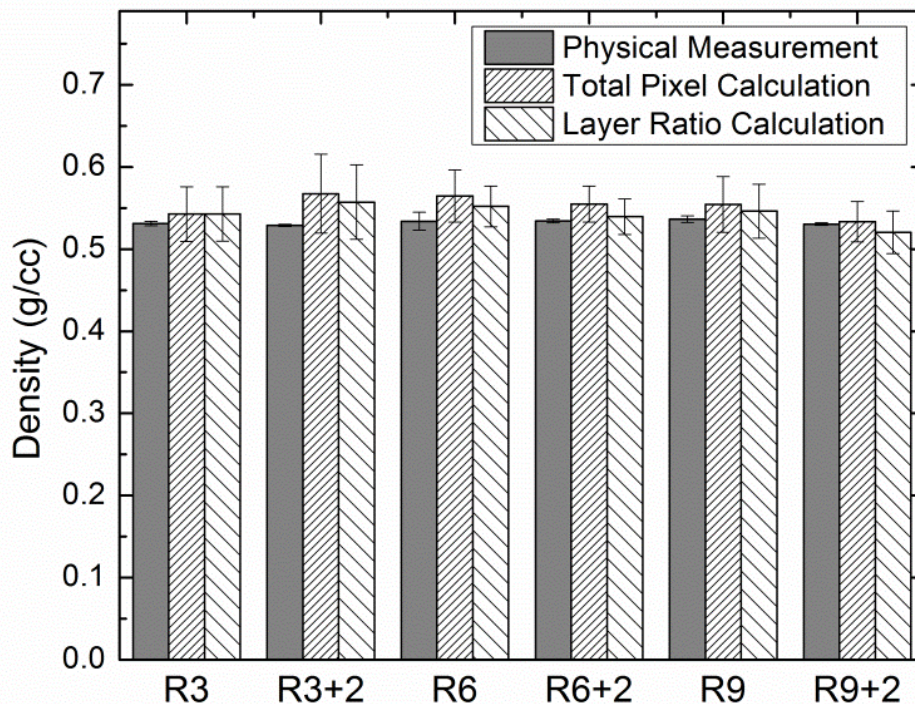


Figure 4.2 Ni atomic fractions for the rolled laminate composites. The Physical Measurements were calculated from densities that were measured using a gas displacement pycnometry technique and multiple 5g specimens taken from the middle and edge of each sample. Ni atomic fractions were also calculated using pixels and two different methods. In the first method (Total Pixel Calculation), Ni atomic fractions were calculated for at least 12 images of each sample by determining the total number of Ni and Al pixels. The values for each image were then averaged and the known densities of Ni and Al were used. In the second method (Layer Ratio Calculation), the Ni atomic fraction of each bilayer was determined using the total number of Ni and Al pixels in each bilayer. These very local chemistries were then area-averaged in at least 12 images for each sample; the 12 plus values were then numerically averaged.

#### 4.2.3 Verification of Microstructural Analysis

To help understand this analysis further we consider three scatterplots of bilayer thickness and Ni percentage shown in Figure 4.1 that were acquired using transverse cross-sectional SEM images of sample R6. The three histograms illustrate how the magnification of an image can affect the results gathered from it. The first image, Figure

4.1 (a), is taken at a low magnification and contains many bilayers that are only a few pixels thick. The small number of pixels per layer results in discrete Ni fractions and the parabolic ‘fans’ shown in the scatterplot below the SEM image. The second image, Figure 4.1 (b), is taken at a high magnification and contains just a few bilayers that range in width from 275 to 350 pixels. Note that the Ni fractions vary in a rather continuous manner but a much smaller fraction of the microstructure is considered. To balance the opposing needs of both imaging a large number of layers and obtaining sufficient Ni fraction resolutions, we chose moderate magnifications as shown in Figure 4.1 (c). The effect of pixilation is still visible in the scatterplot below this image but more than 10 bilayers are shown in the photo and most are thicker than 50 pixels, minimizing the pixilation.

### **4.3 Results**

Ni atomic fractions of the Ni:Al foils were quantified three different ways: (1) Physical Measurements were made with gas pycnometry, performed on pieces of the rolled Ni/Al composites taken from both the middle and edges of each laminate to calculate physical density from the volume and mass for each piece, then the Ni atomic fraction was calculated from the density; (2) The Total Pixel Calculation tabulated the total number of Ni and Al pixels in at least 12 micrographs to determine the Ni area fraction. An average Ni atomic fraction was calculated for each sample using the known densities of Ni and Al; (3) The Layer Ratio Calculation determined the Ni pixel ratio in each bilayer and was area-averaged in each of the 12 micrographs. The average Ni

fraction was then determined from a numerical average of the Ni fractions for the 12 plus images. The results of these three characterizations are shown in Figure 4.2.

Table 4.1 Volume average bilayer thickness, number average bilayer thickness, the coefficient of variance (CoV) for the volume average and the volume average bilayer reduction percentages per pass are listed for each sample. At least 12 to 15 images were used to calculate each value. The number averages are smaller than the volume averages due to a large number of relatively small bilayers that are counted more heavily in a number average, but constitute a small fraction of the area of each image. The volume average coefficient of variance always drops after rolling with additional 20% thickness reductions. In general, microstructural refinement decreases with each additional rolling pass.

|      | Total Volume Average ( $\mu\text{m}$ ) | Total Number Average ( $\mu\text{m}$ ) | Volume Average Coefficient of Variance | Volume Average Bilayer Reduction Percentage per Rolling Pass |                |                      |
|------|--|--|--|--|----------------|----------------------|
|      |  |  |  | 50 % Reductions  | 20% Reductions | Three 20% Reductions |
| R3   | 14 +/- 3.2                             | 10 +/- 3.0                             | 0.23                                   | 31%  |                |                      |
| R3+2 | 6.5 +/- 1.3                            | 3.9 +/- 1.0                            | 0.19                                   |  | 12%            | 32%                  |
| R6   | 5.3 +/- 1.5                            | 3.1 +/- 1.2                            | 0.28                                   | 28%  |                |                      |
| R6+2 | 2.2 +/- 0.5                            | 1.2 +/- 0.3                            | 0.24                                   |  | 14%            | 36%                  |
| R9   | 3.2 +/- 0.7                            | 1.8 +/- 0.5                            | 0.22                                   | 16%  |                |                      |
| R9+2 | 2.4 +/- 0.5                            | 1.4 +/- 0.3                            | 0.22                                   |  | 4.7%           | 13%                  |

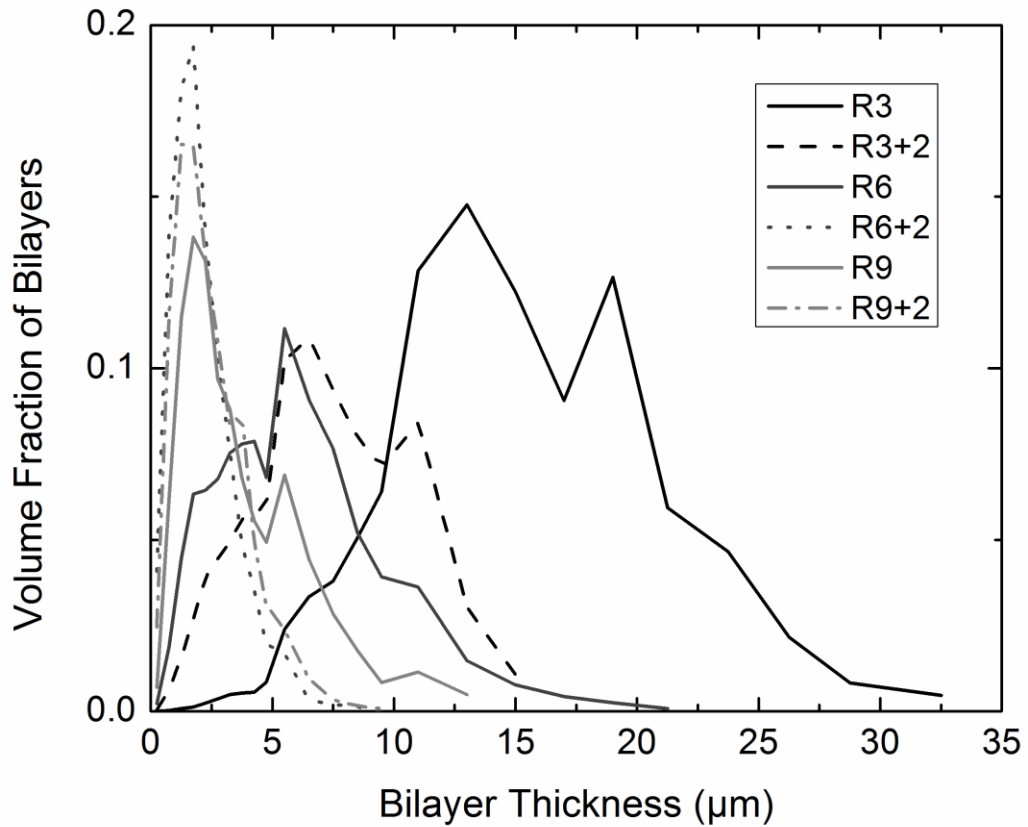
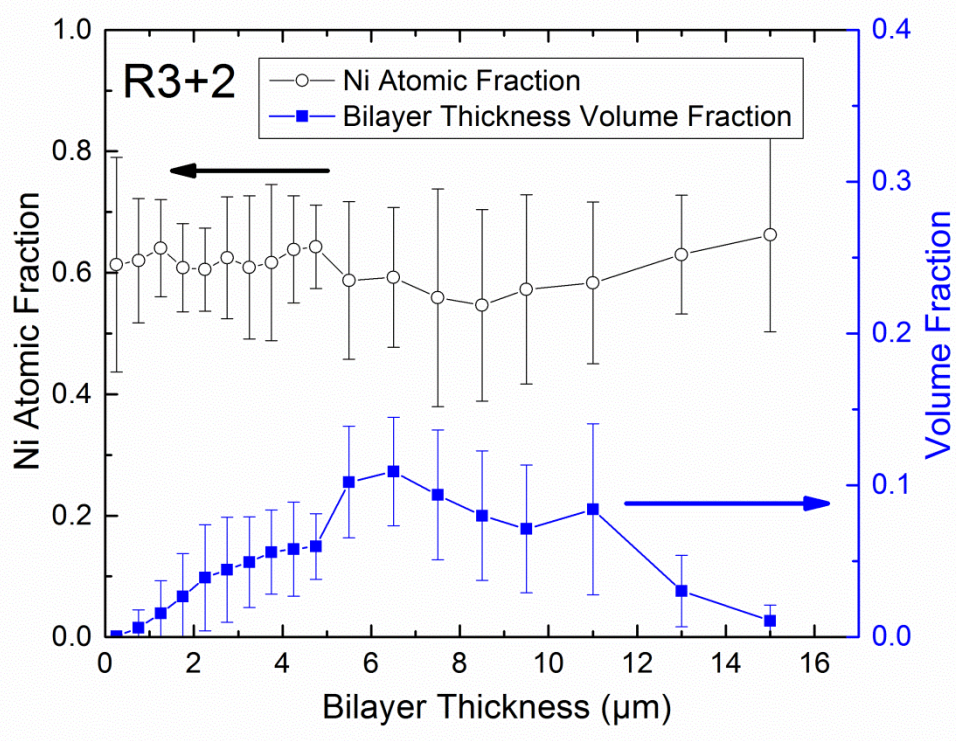
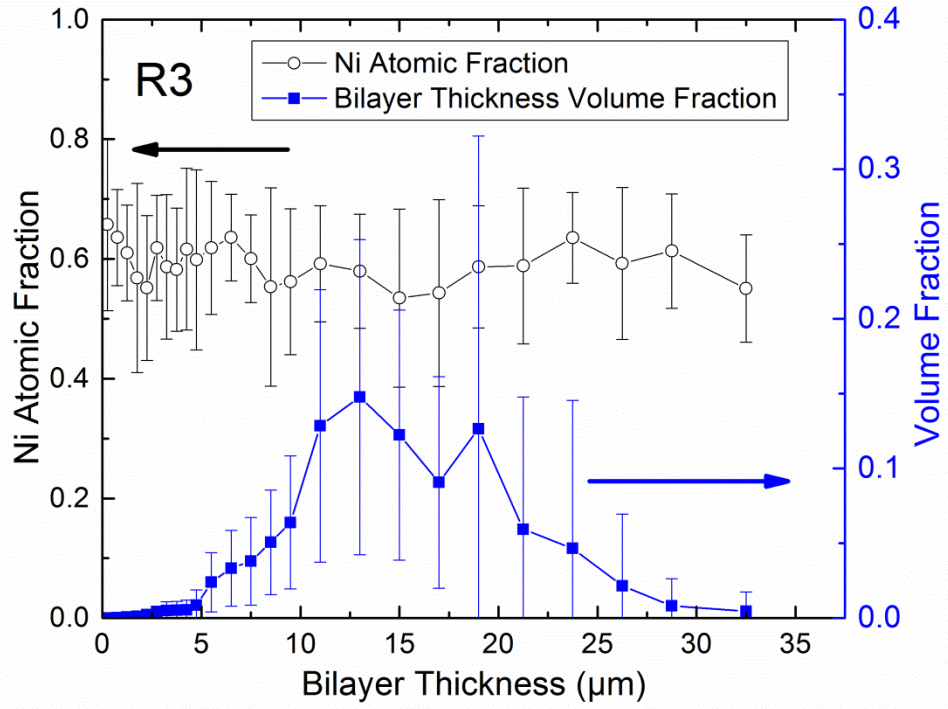
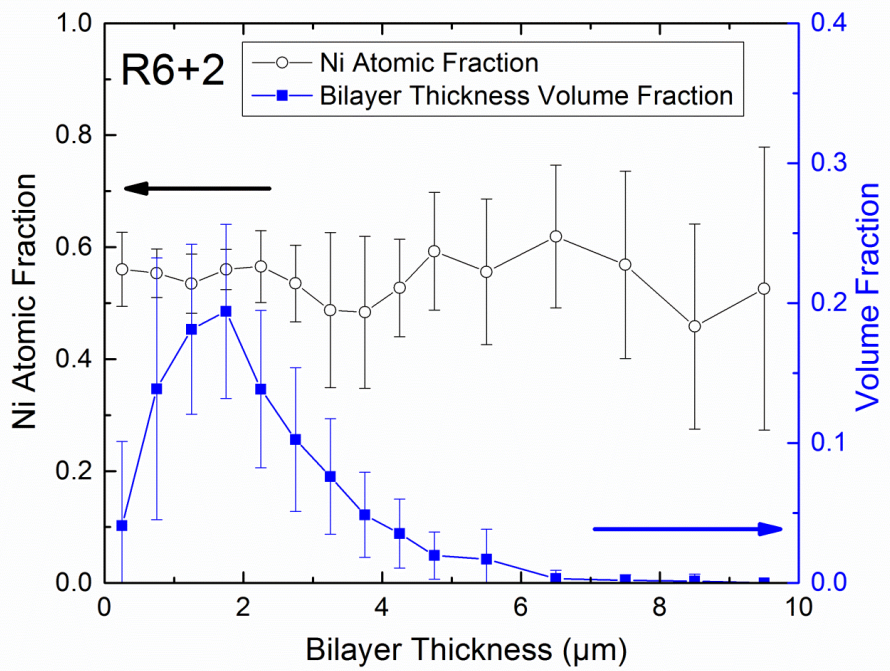
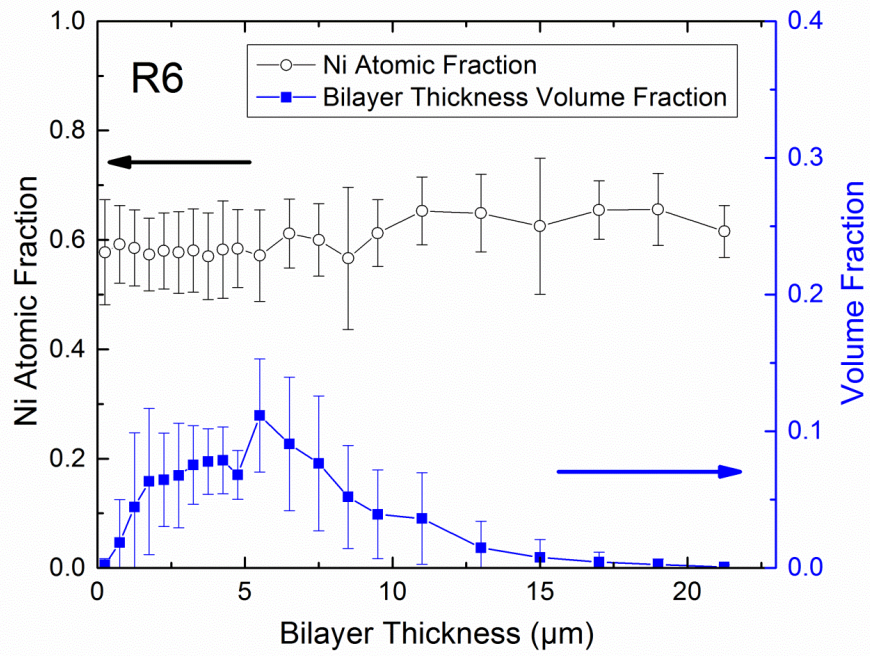


Figure 4.3 Bilayer volume fraction histograms for each of the rolled composites based on 12 to 15 images taken from the rolling and transverse cross-sections. Note that the distributions narrow with more rolling passes.

Table 4.1 lists results from microstructural analysis of 12 to 15 different images for each of the six samples. The first three columns display the volume average bilayer thickness, the number average bilayer thickness, and the coefficient of variance for the volume average bilayer thickness. In general, we note that bilayer thickness decreases as more rolling passes are employed, and we also note that the number average bilayer thickness is smaller than the volume average bilayer thickness, indicating a large number of small bilayers are present.





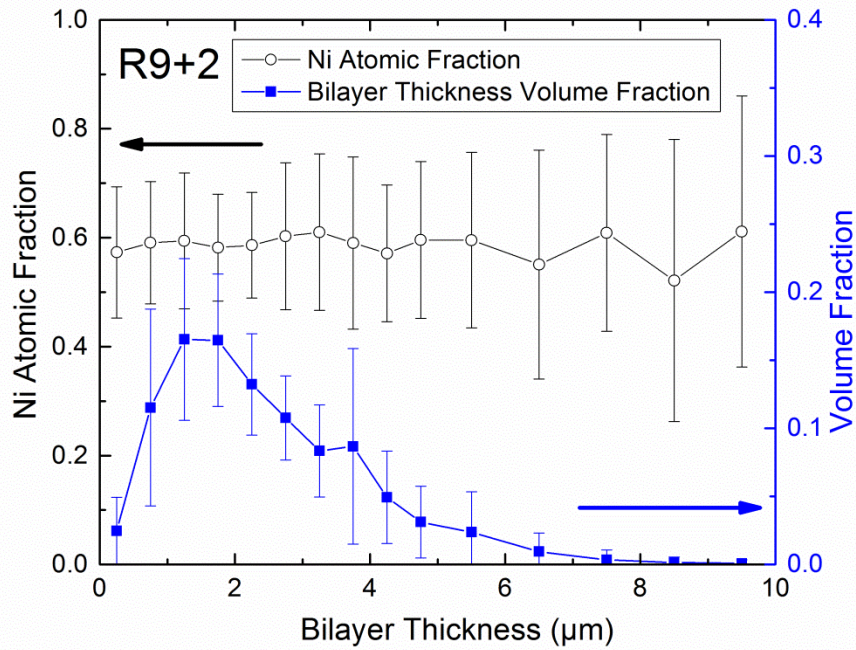
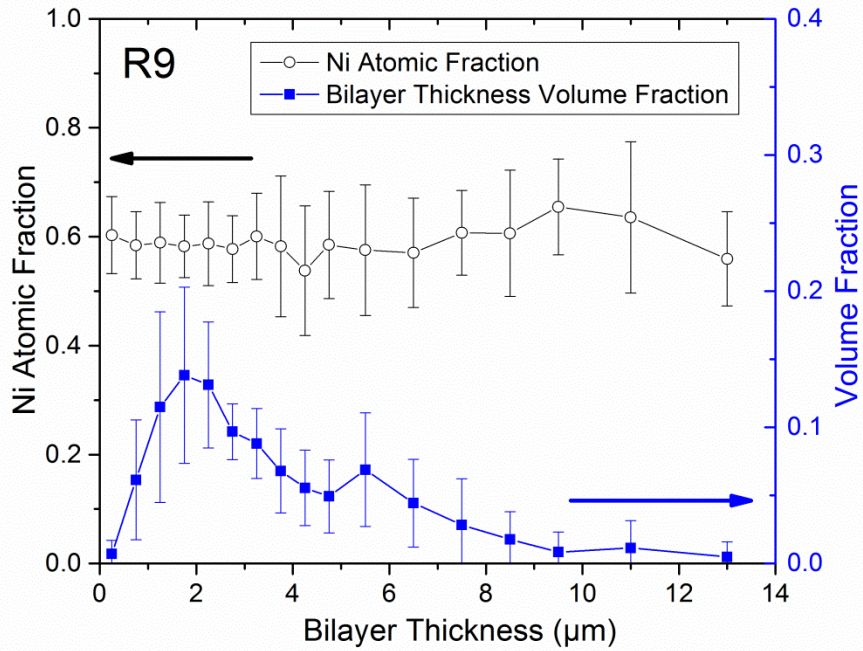


Figure 4.4 Bilayer volume fractions and their corresponding chemistry (Ni atomic fraction) versus bilayer thickness for all 6 samples. The bilayer volume fraction is the lower curve and corresponds to the right axis while the chemistry is the top curve and corresponds to the left axis.

The relatively large standard deviations and coefficients of variance (COV) confirm that rolled microstructures are nonuniform, but the consistent drop in the COV following the additional 20% rolling passes indicate that the more gradual 20% reductions improve the uniformity of the microstructures. The last three columns in

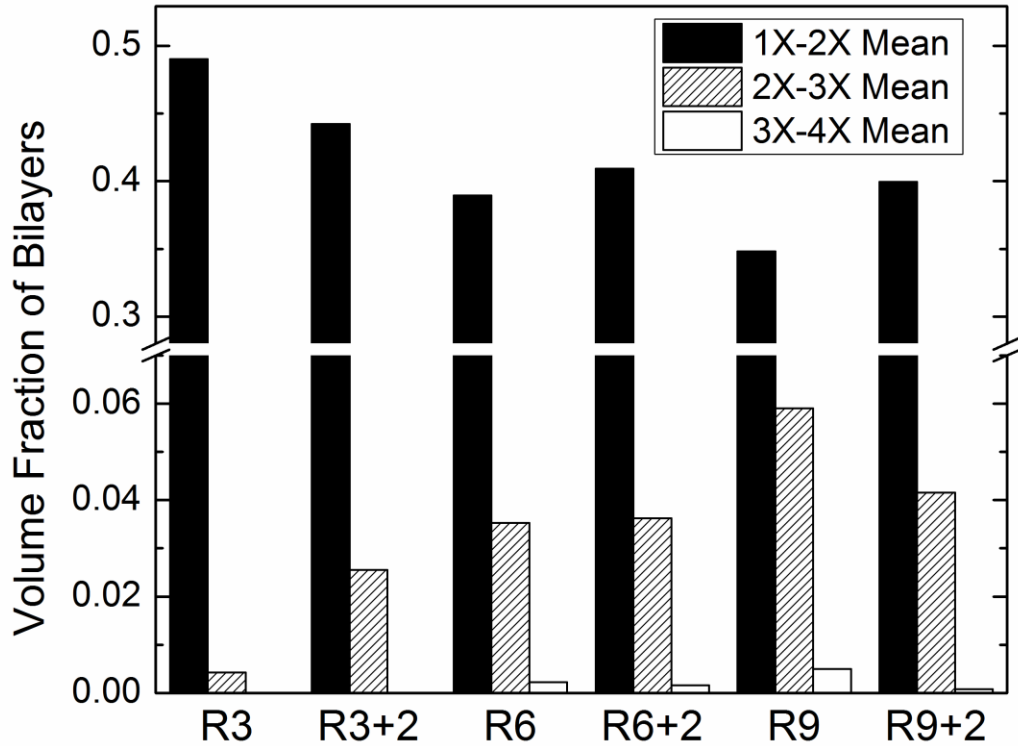


Figure 4.5 Volume fraction of bilayers within each sample that fall into various thickness ranges relative to the volume average bilayer thickness. R3 has very few bilayers that are much larger than the mean, and R9 has the largest populations.

Table 4.1 list percent reductions in the volume average bilayer thickness per rolling pass.

Note that the percent reduction per pass tends to decrease as the number of rolling passes increases and the material hardens. This is particularly true for the heavily rolled samples such as the transitions from R6 to R9 and from R9 to R9+2.

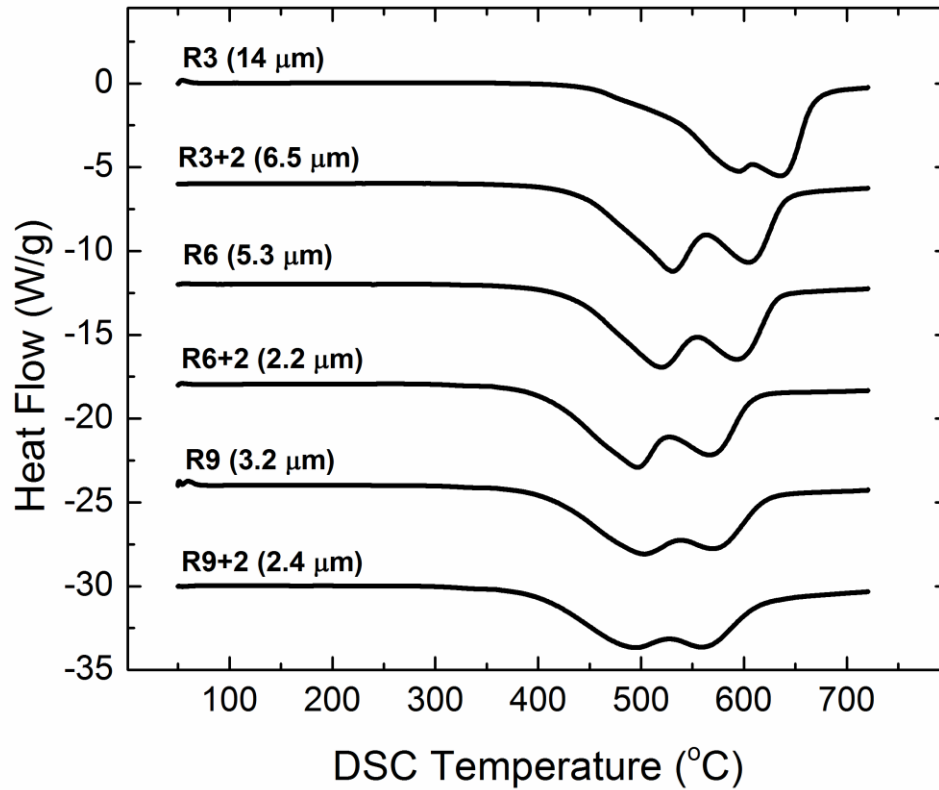


Figure 4.6 DSC curves for the 6 laminate samples. The two major exothermic peaks shift to lower temperatures as the number of rolling passes increase and the volume average bilayer (in parentheses) decreases. The first peak corresponds to the formation of the  $\text{NiAl}_3$  intermetallic + Ni and the second peak is the formation of the  $\text{Ni}_2\text{Al}_3$  intermetallic + NiAl + Ni.

Figure 4.3 displays histograms of the measured bilayer thicknesses for each sample. The comparison shows a clear narrowing of the distribution as the number of rolling passes increases and the average bilayer thickness decreases. Note that most samples show a bimodal distribution and that the bimodal distributions for samples R3, R6 and R9 tend to diminish as six additional 20% reductions are applied to obtain samples R3+2, R6+2 and R9+2. We note that the Ni atomic fraction was calculated for

each thickness range and shows no dependence and stays within the range of the standard deviation, shown in Figure 4.4.

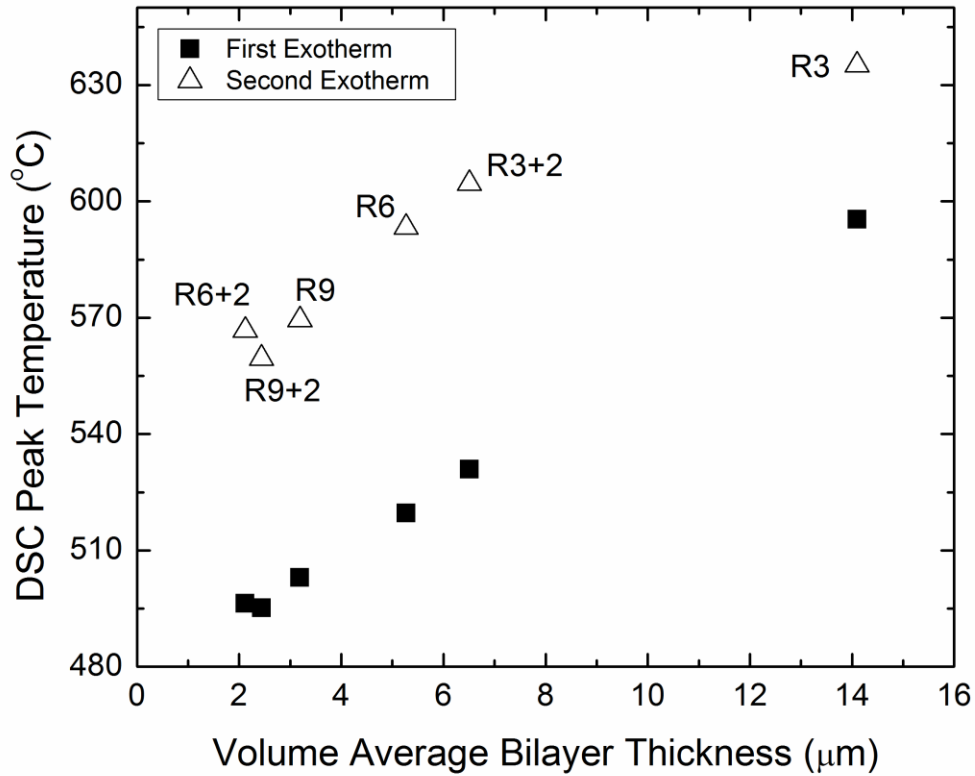


Figure 4.7 Peak temperatures for the DSC scans in Figure 4.6 are plotted versus volume average bilayer thickness for each sample. Note that peak temperatures decrease with additional rolling passes.

Another way to quantify the bilayer thickness distributions is to examine the volume fraction of bilayers greater than the volume average bilayer thickness or greater than multiples of the volume average bilayer thickness, as shown in Figure 4.5. R3 and R3+2 both have very small populations of bilayers that are larger than twice the volume average. R6 and R6+2 both have similar distributions, with a volume fraction of  $\sim 0.04$  for bilayers between twice to three times the volume average and very few bilayers between three times to four times the volume average. R9 has the largest volume fraction

of bilayers between twice and three times, and three times to four times the volume average, 0.06 and 0.01, respectively. However, R9+2 has a volume fraction of 0.04 for bilayers twice and three times the volume average and almost no bilayers between three times and four times the volume average.

Multiple DSC scans were run on each of the six rolled composites and typical scans are plotted in Figure 4.6; all show two broad exotherms between 400 °C and 700 °C. Based on symmetric X-ray diffraction of samples that were heated just beyond the

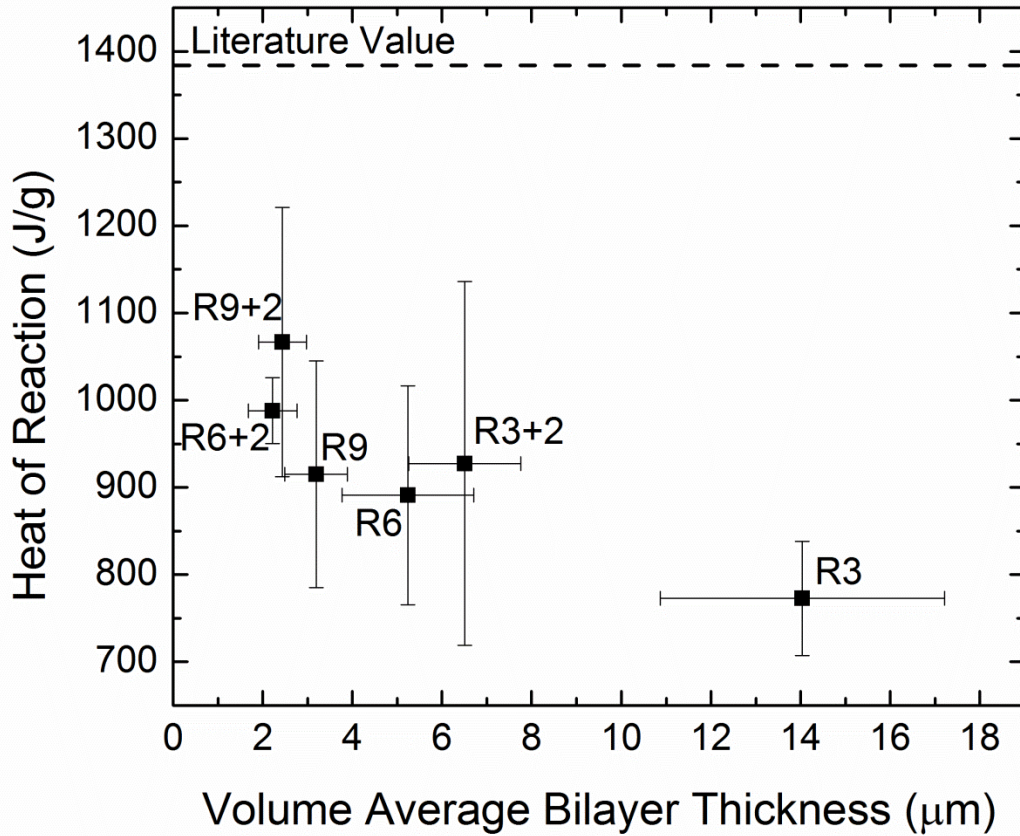


Figure 4.8 Measured heats of reaction versus volume average bilayer thickness. In general, foils with more extensive rolling release more heat. Note, however, that samples with additional 20% thickness reductions release more energy on average than samples with only 50% thickness reductions. The literature heat for full intermixing is 1380 +/- 40 J/g [27].

peak temperatures and then quenched, the first peak corresponds to the formation of NiAl<sub>3</sub> with excess Ni and the second peak is the formation of the Ni<sub>2</sub>Al<sub>3</sub> intermetallic + NiAl intermetallic with excess Ni. Note that the peaks for the two exotherms shift to

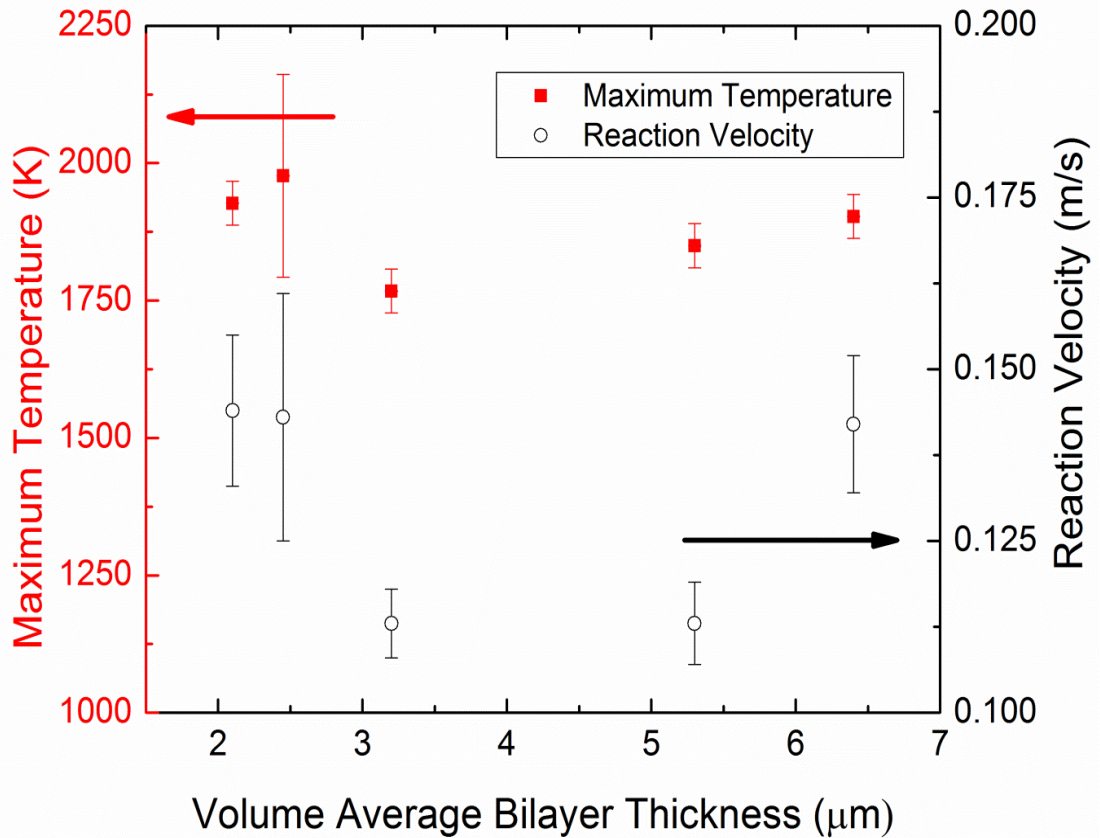


Figure 4.9 Measured velocities and maximum temperatures for self-propagating formation reactions in all samples except R3. The data show no dependence on the volume average bilayer spacing, which is unexpected given previous studies [1,19,20]. Instead, the velocity and  $T_{\max}$  appear to depend only on processing conditions with R3+2, R6+2 and R9+2 having a faster and hotter reaction than R6 and R9.

lower temperatures as the amount of rolling increases and the bilayer thickness decreases. This roughly linear trend of peak temperature with bilayer thickness is displayed clearly in Figure 4.7. The heats of reaction, obtained by integrating the curves in Figure 4.6, are plotted in Figure 4.8 and show the opposite trend: the heat released

during a DSC scan decreases as bilayer thickness increases. The heats of reaction that we measured are lower than the literature heat, as expected, because the foils cannot fully react in DSC scans to 725 °C. More stored energy will be released at high temperatures when the metastable products transform to the stable AlNi intermetallic. Note that the foils with additional 20% thickness reductions release more heat on average than the foils with just 50% thickness reductions. Figure 4.9 displays the velocity and maximum temperature ( $T_{\max}$ ) for self-propagating reactions that were spark ignited at room temperature in all samples except R3. X-ray diffraction was performed on samples after flame reaction and the 1:1 AlNi intermetallic phase was the only phase present. In all cases the reaction propagated in an unsteady earlier in Co/Al multilayers [21].



Figure 4.10 Reaction front image taken from a high-speed video. The propagating front is light, while the dark area of the photo is unreacted foil. Nucleating fronts can be seen near the top as they begin to react, perpendicular to the global propagation direction. The bright spots over the unreacted foil are particles that are sprayed off the foil as it reacts.

Here we see the formation of reaction bands at the reaction front that grow or spread normal to the global propagation direction and parallel to the reaction front. The formation of three such bands is identified in Figure 4.10. In contrast to past studies, though, we do not see a smooth variation of reaction velocity [1,2,5,19], or  $T_{\max}$  [22] with

the bilayer thickness. Instead, samples with only 50% thickness reductions, R6 and R9, have slower and cooler reactions than the foils with additional 20% thickness reductions: R3+2, R6+2 and R9+2. The subsequent discussion explores the underlying microstructure in the rolled composites in an attempt to explain this anomalous behavior, as typically the reaction velocity varies with the volume average bilayer thickness.

## **4.4 Discussion**

### **4.4.1 Density and Chemistry**

We first consider the three different density measurements to assess the uniformity of the Ni atomic fraction in the cold-rolled composites and to assess the quality and limitations of this microstructure analysis routine. For the physical measurements of density each data point in Figure 4.2 represents three tests from the edge of the laminate and three from the center; the Ni atomic fraction is calculated using the known densities of Ni and Al and assuming fully dense samples. Since the measurements of mass and volume have very low errors, 0.001% and 0.1%, respectively, fluctuations in density within or between samples could be attributed to variations in chemistry or the presence of voids. However, the data show very low standard deviations (<1%) suggesting that chemistry is uniform between different regions of the foil and that few large voids are present. The absence of voids within the many micrographs further supports this point and suggests that even small voids are absent. Lastly, the densities show little variation among samples and suggest an as-processed chemistry of 53 +/- 1 at% Ni, very close to the expected chemistry of 52 at% Ni, based on the thicknesses of the starting foils.

Ni atomic fractions also were calculated using the black (Al) and gray (Ni) pixels identified on all micrographs for a given sample. The Total Pixel Calculation tends to fall slightly above the Layer Ratio Calculation, and both are slightly above the physically measured averages as seen in Figure 4.2. However, given the large error bars for the pixel-based calculations, these differences are not likely to be statistically significant. The 12-15 micrographs used for each sample represent an area of approximately 100,000  $\mu\text{m}^2$  and we assume to a depth of 100  $\mu\text{m}$  or less. Thus, the imaged volume is  $10^5$  times smaller than the volumes ( $10^{12}$   $\mu\text{m}^3$  or 5g) used for the physical density measurements. Consequently, local variations in chemistry could be producing the larger standard deviations for pixel-based Ni atomic fractions. However, in general, the pixel-based Ni atomic fractions are in good agreement with Ni atomic fractions calculated using measured densities. This suggests that biases introduced by the choice of images or by the thresholding routine are relatively minor. It also suggests that the Ni atomic fractions calculated from pixels provide an effective indication of local chemistries.

To further assess how well one can calculate local chemistries using pixilated images we reconsider the ‘parabolic arcs’ in Figure 4.1 in which Ni atomic fraction is plotted versus bilayer thickness in pixels. Note that for very small bilayer thicknesses (less than 50 pixels) the chemistry is quantized. Adding an additional Ni pixel to a bilayer leads to discrete jumps in chemistry and the rounding associated with such calculations can produce errors. One way to reduce the effects of pixilation is to zoom in so far that few bilayers appear in each photo. However, very few bilayers per image require one to analyze many images to gain reasonable statistics. Here we suggest that 30 pixels per bilayer is a reasonable minimum size as it yields an error in thickness and

chemistry of approximately 5%. In this study we chose magnifications to produce images with 10 to 30 bilayers per image and then captured and analyzed 12 to 15 images per sample.

#### **4.4.2 Average Bilayer Thickness**

Table 4.1 shows that the average bilayer thickness of all of the composite foils consistently decreases with additional rolling passes. However, the degree of bilayer thinning for each 50% reduction in sample thickness tends to diminish with more rolling passes. For samples R3 and R3+2 the volume average bilayer thinned more than 30% for each 50% reduction in sample thickness. For R9 and R9+2, though, the volume average bilayer thinned less than 16% for each 50% reduction in sample thickness. The decreased thinning of the bilayer is attributed to strain hardening and pinch-off of the layers. As plastic strain accumulates in the layers, additional plastic deformation is impeded and layers begin to pinch-off, leading to a thinning and lengthening of the sample without a corresponding reduction in layer thickness. Previous studies have found that a large difference in hardness between the hard and soft phases, such as seen for Al and Ni, controls the layer refinement by promoting necking and pinch-off instead of uniform deformation [23]. Without the pinch-off of layers, the reductions in bilayer thickness should correlate directly with reductions in sample thickness. Thus, rolling parameters that favor layer thinning over layer pinch-off are preferred. We explore this concept by comparing the results from the two types of rolling passes: 50% sample thickness reductions and 20% sample thickness reductions.

To begin the comparison we reiterate that the coefficient of variance for the volume average bilayer thickness decreases as samples R3, R6 and R9 are reduced to

R3+2, R6+2 and R9+2, respectively, with six 20% rolling reductions. Thus, the 20% rolling reductions appear to produce a more uniform microstructure than the 50% rolling reductions. This can be seen qualitatively by comparing distributions for R3 and R3+2, R6 and R6+2, and R9 and R9+2 in Figure 4.3. Note that the bimodal nature of the bilayer distributions appears to diminish with the additional 20% rolling reductions. The 20% reductions also appear to be more effective at reducing the volume average bilayer thickness compared to the 50% reductions. Consider sample R6. When it was rolled to R9 with three 50% rolling reductions its bilayer thickness decreased by a total of 47% or 16% per rolling pass as shown in Table 4.1. When R6 was rolled to R6+2 with six 20% rolling reductions (or the equivalent of two 50% rolling reductions), its bilayer thickness decreased by 71% or 36% per equivalent 50% rolling reductions. Thus, more gradual 20% rolling reductions are more effective at thinning the average bilayer than the more abrupt 50% rolling reductions. This conclusion agrees with the results reported previously in [24].

The reduction of the average bilayer thickness with rolling leads to a clear shift in the DSC curves in Figure 4.6. The peaks of the first and second exotherms shift to lower temperatures as the average bilayer thickness thins for all samples. The only exception to this trend is sample R6+2, which has a smaller measured bilayer thickness than R9 and R9+2. However, the volume of the DSC samples is much greater than the effective volume characterized by the 12 to 15 micrographs for sample R6+2. For a 10 mg DSC sample the effective volume is  $\sim 10^9 \mu\text{m}^3$  and we estimate it to be  $\sim 10^7 \mu\text{m}^3$  for the image-based microstructural analysis of each sample. Thus, we suggest that the “bulk” DSC measurements provide a better estimate of a sample’s average microstructure or

chemistry, and we propose that the average bilayer thickness for sample R6+2 falls between the values for samples R9 and R9+2, as suggested by the temperatures for the exothermic peaks in Figure 4.7.

In addition to controlling the peak temperatures during DSC scans, the volume average bilayer thickness has been shown to control the velocity of the self-propagating formation reactions in Ni:Al multilayer foils, as well as the maximum reaction temperature at very small bilayer thicknesses [1,25]. For example, most researchers report that reaction velocity increases as bilayer thicknesses decrease and the average distance for atomic intermixing distances drops. At the smallest bilayer thicknesses, though, typically under 50 nm, intermixing during fabrication can lead to reductions in the heat of reaction, the maximum reaction temperature, and hence the measured reaction velocity. However, given the micrometer-sized bilayers studied here and the relatively low temperature rise during cold-rolling, the effect of premixing should be negligible [5,19,22]. In contrast to earlier reports, Figure 4.9 shows no dependence of reaction velocity or temperature on average bilayer thickness for the current cold-rolled laminate composites. Instead Figure 4.9 suggests that foils fabricated with 20% thickness reductions have hotter and faster reactions than foils fabricated with only 50% thickness reductions. Next we explore the distributions of bilayer thickness to find an explanation for this unexpected behavior.

#### **4.4.3 Bilayer Spatial and Thickness Distributions**

As noted earlier, the spatial distribution of bilayer thicknesses can affect the reaction velocity [1]. A coarse spatial distribution of small and large bilayers can lead to the small bilayers dominating reaction properties, while a fine spatial distribution causes the volume average bilayer thickness to govern the reaction velocity. To determine if a

coarse or a fine spatial distribution of bilayers exists in each sample we looked for clumping of large bilayers. Based on the bilayer distributions in Figure 4.3 the volume fraction of each sample that contains two adjacent bilayers that are both twice the mean is less than  $6 \times 10^{-6}$ . This strongly suggests that clustering is insignificant. Thus, with a fine spatial distribution we expect that the average bilayer will control reaction properties. However, the large bilayers can still have a secondary impact on reaction properties.

As the NiAl formation reaction self-propagates in these laminate composites, a

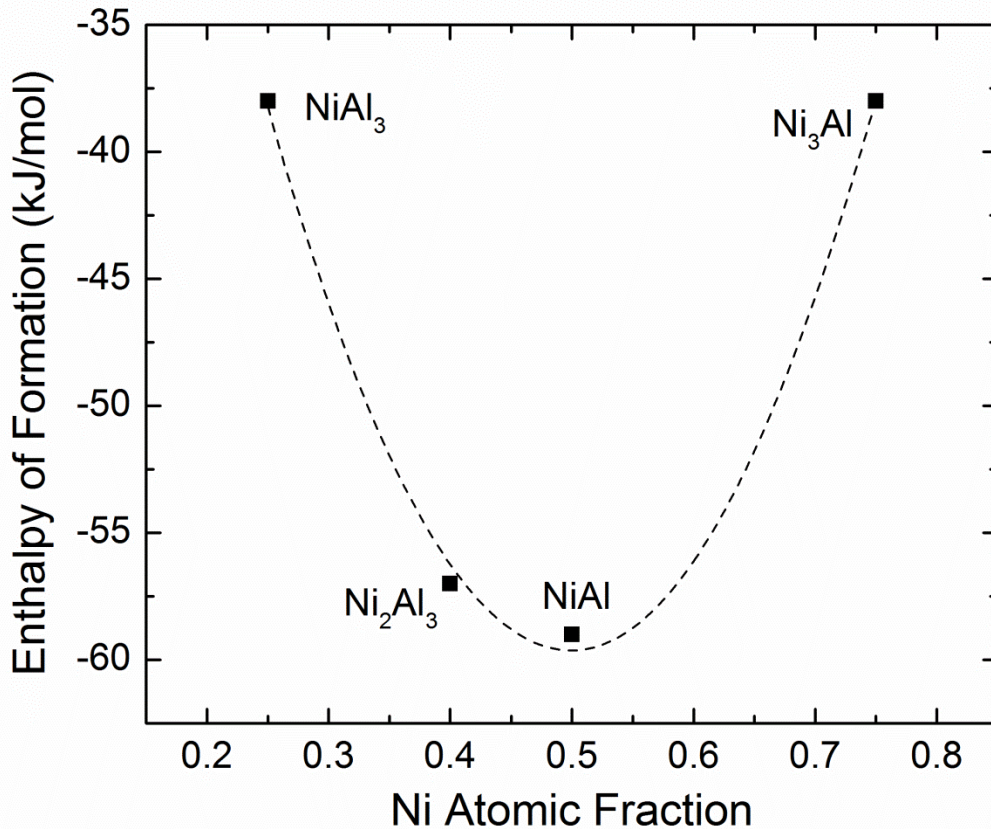


Figure 4.11 Enthalpy of formation vs. Ni atomic fraction. Note that the heat varies quadratically with composition so bilayers with chemistries greater or less than 50:50 will release less heat during self-propagating reactions [35]. The dashed line is a fit to the data for estimating heats of reaction for samples with average compositions between the given intermetallic compounds

certain fraction of the bilayers can be assumed to react completely and release the majority of their heat as the front passes. However, the large bilayers are unlikely to mix completely as the reaction front passes, simply due to their longer diffusion distances. This should lower the energy released in the reaction front and hence the maximum reaction temperature,  $T_{\max}$  [22,25]. The heat of reaction data reported in Figure 4.8 supports this argument. During the DSC scans to 725 °C the samples with large bilayers are less likely to react completely and a lower heat is measured. This general trend is seen in Figure 4.8 and has been reported earlier in [26]. However, note that the samples with additional 20% thickness reductions (R3+2, R6+2 and R9+2) release as much or more heat than any sample with only 50% thickness reductions (R3, R6 and R9). The lower percentage of larger bilayers in the R3+2, R6+2 and R9+2 samples likely enables more complete mixing during the DSC scans and hence higher measured heats. A similarly higher release of heat could also be expected during self-propagation of these formation reactions.

#### **4.4.5 Predicting $T_{\max}$ for Self-propagating Reactions**

Having argued that large bilayers can impede heat production within the reaction front, we now use the detailed microstructural data and the local composition data to predict  $T_{\max}$  for the self-propagating reactions. It should be noted that the maximum temperature for the Ni:Al 1:1 intermetallic formation reaction is commonly measured to be 1912 K, but the theoretical temperature without melting is higher, at 2380 K. We will ignore melting in our analysis to more effectively compare maximum temperatures for the different samples.

We begin our predictions of  $T_{\max}$  by first considering only the impact of large bilayers. Then we explore the impact of local variations in Ni atomic fractions on  $T_{\max}$

by assuming the local chemistry determines the maximum possible value of the local heat release. We use a  $\Delta H_{reaction}$  curve fit to experimental values, shown in Figure 4.11, to estimate the maximum value of the heat that can be released from each bilayer as a function of its Ni atomic fraction [27]. Finally, we combine both effects to predict maximum temperatures and reaction velocities.

#### A) Large Bilayer Effect

To predict the effect of only large bilayers on the maximum temperature we assume that some fraction of Ni and Al atoms react to form the NiAl phase in each bilayer. The fraction is determined by the thickness of the specific bilayer,  $\lambda_i$ , and the thickness of the volume average bilayer for that sample,  $\lambda_{avg}$ . These fractions are summed for all bilayers in the 12 to 15 micrographs that we analyzed for each sample to predict a maximum temperature  $T_{maximum}^{predicted}$  through

$$T_{maximum}^{predicted} = \left\{ 1 - \sum \frac{(\lambda_i - \lambda_{avg})}{\lambda_i} \right\} \times T_{maximum}^{theoretical} \quad (4.1)$$

If any bilayer thickness is smaller than the volume average bilayer complete reaction is assumed and  $\lambda_i - \lambda_{avg}$  is set equal to zero. The fraction in Equation 4.1 was summed for all the images of each sample and the results are plotted in Figure 4.12 as “Large Bilayer Model.” Note that  $T_{maximum}^{predicted}$  is the theoretical maximum temperature in the absence of any phase transformations or heat losses.

#### B) Local Chemistry Effect

To determine only the impact of local chemistry on the maximum temperature during self-propagating reaction we assume that the local chemistry equilibrates across a thickness equivalent to the average bilayer thickness. Thus, for a small bilayer ( $\lambda_i < \lambda_{avg}$ )

we assess chemistry across an area that includes neighboring bilayers to determine the

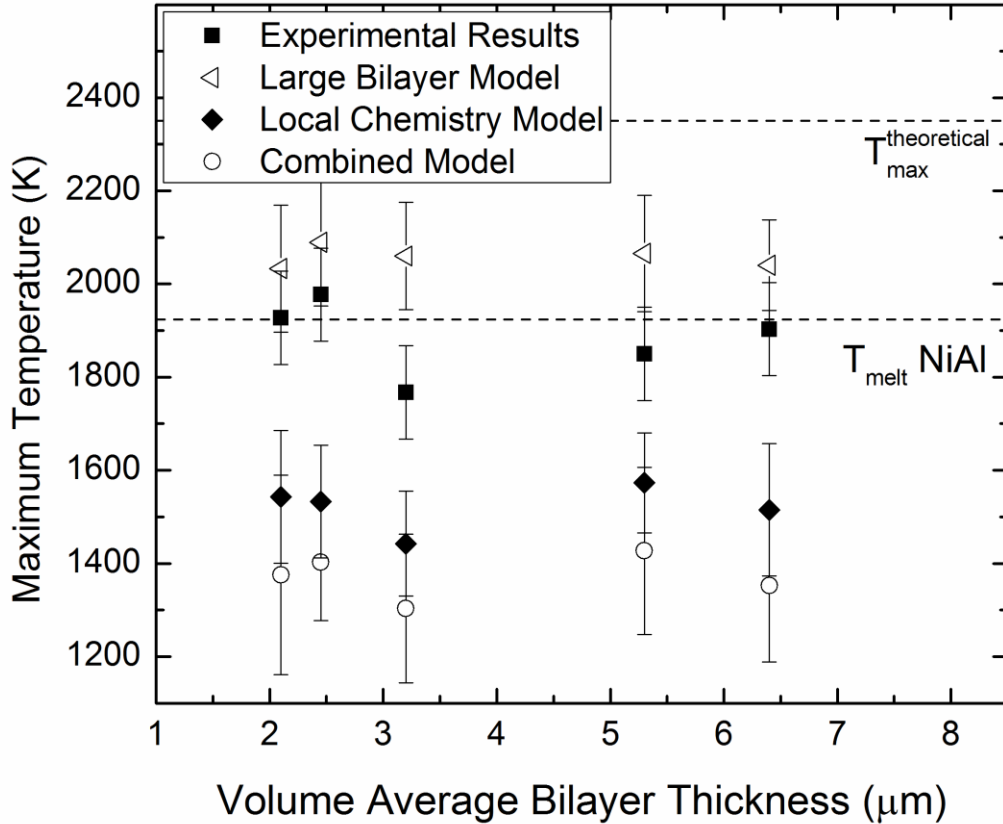


Figure 4.12 Predictions and measurements of maximum reaction temperatures are plotted for samples as a function of their volume average bilayer thickness. The “Large Bilayer Effect” accounts for large bilayers that cannot mix fully as the reaction front passes, “Local Chemistry” accounts for variations in heats produced due to local variations in chemistry as the reaction front passes and the “Combined Model” uses both methods to predict the expected maximum temperature. It should be noted that the predicted temperatures assume a solid product and do not consider the heat of fusion for the intermetallics being produced. The standard deviations are attained by averaging the predicted temperatures for each of 12-15 SEM images.

stoichiometry for that given bilayer. The chemistry analysis extends out  $\frac{1}{2}$  of  $\lambda_{\text{avg}}$  from the center of each small bilayer and uses the measured Ni fractions. For large bilayers ( $\lambda_i > \lambda_{\text{avg}}$ ) the chemistry for an individual bilayer is simply its measured Ni fraction. Once chemistries are known, local heats of reaction are determined using the calculated

$\Delta H_{formation}$  curve shown in Figure 4.11. We normalize the local heats of reaction based on a bilayer's area fraction within a given image, and then we sum the normalized heats with a temperature dependent heat capacity and ignore latent heats at phase transitions to predict  $T_{maximum}^{predicted}$  [27]. The results of these calculations are plotted in Figure 4.12 as "Local Chemistry Model."

### C) *Combination of Large Bilayer and Local Chemistry Effects*

We now combine the effects of both large bilayers and local chemistry to predict  $T_{max}$ . For all bilayers less than the volume average bilayer thickness complete mixing is assumed and the heat of reaction is determined by the chemistry within an area that extends  $\pm \frac{1}{2} \lambda_{avg}$  from the center of the bilayer. If a bilayer is larger than the volume average, then the calculated energy released is a function of both bilayer thickness and its Ni atomic fraction. For example, if a bilayer thickness is twice the volume average bilayer thickness and has a Ni atomic fraction of 0.4, it would release half of the energy expected based on its chemistry. The results of these predictions are plotted in Figure 4.12 as "Combined Model."

Based on our calculations, the effect of large bilayers on  $T_{max}$  is much smaller than the effect of Ni atomic fraction. The maximum temperatures that are predicted when considering only large bilayers effects are higher than the measured reaction temperatures in Figure 4.13. In contrast,  $T_{max}$  predictions based only on the local chemistries are lower than the measured temperatures, suggesting that this is the stronger factor in controlling reaction temperature. Combining both factors leads to predictions that are approximately 500K lower than the measured maximum temperatures. This suggests that the interdiffusion length scale parameter ( $\lambda_{avg}$ ) should be increased to

predict more mixing as the reaction front passes. We can increase the assumed mixing distance to  $1.5 \lambda_{\text{avg}}$  or  $2.0 \lambda_{\text{avg}}$  to determine the effect on the predicted  $T_{\text{max}}$ .

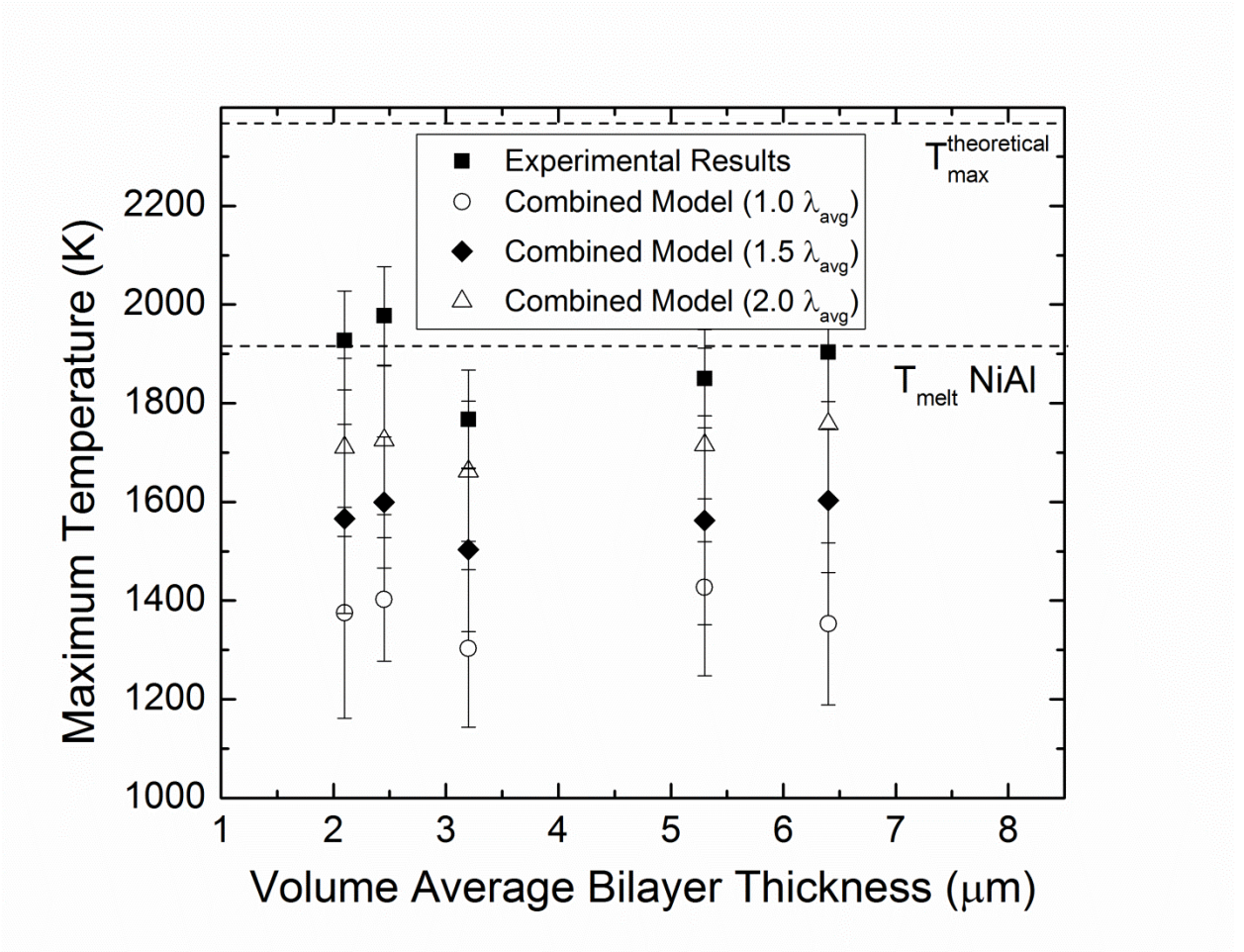


Figure 4.13  $T_{\text{max}}$  is predicted using the Combined Model and different atomic diffusion distances as the reaction front passes. Increasing the assumed diffusion distance increases the predicted degrees of mixing and hence the maximum temperatures. This results in a closer match to the measured experimental values. The standard deviations are attained by averaging the predicted temperatures for each of 12-15 SEM images.

We predicted  $T_{\text{max}}$  using both  $1.5 \lambda_{\text{avg}}$  and  $2.0 \lambda_{\text{avg}}$  in place of  $\lambda_{\text{avg}}$  in Equation 4.1 and the additional predictions are shown in Figure 4.13. Not surprisingly, the larger interdiffusion scaling parameters increase the predicted maximum temperatures. While

all predictions are lower than the experimental values, the  $2.0 \lambda_{\text{avg}}$  Combined Model offers reasonable agreement with the measured values and suggests that interdiffusion of Ni and Al occurs across a greater distance within the self-propagating reaction front than initially thought. Using  $2.0 \lambda_{\text{avg}}$  in Equation 4.1 doubles the assumed mixing distance during the reaction front and the comparisons in Figure 4.13 suggest that it could be slightly higher still.

An important point to note in Figure 4.13 is that the maximum temperatures predicted with the Combined Model and  $2.0 \lambda_{\text{avg}}$  match the variations seen in the measured values quite well. Samples R3+2, R6+2 and R9+2 all have a higher predicted maximum temperature than R6 and R9, and R9 has a lower predicted temperature than R6, similar to the experimental findings. This agreement supports the hypothesis that a combination of large bilayers and the variations in local chemistry determine the total heat produced within the reaction front and hence the maximum reaction temperatures.

#### 4.4.6 Predicting Reaction Velocity

In contrast to previous studies, the reaction velocities plotted in Figure 4.9 do not show a clear dependence on average bilayer thickness. However, given the corresponding variations in  $T_{\text{max}}$  and the explanations noted above, we consider whether the measured and predicted reaction temperatures could account for the unusual variation in reaction velocities with bilayer thickness. To explore this possibility we consider the analytical solution of Armstrong and Koszysowsky [28] that relates reaction velocity to temperature during self-propagation

$$v^2 = \frac{3ART^2 e^{\frac{-E_a}{RT}}}{\delta^2 E_a (T - T_0)} \quad (4.2)$$

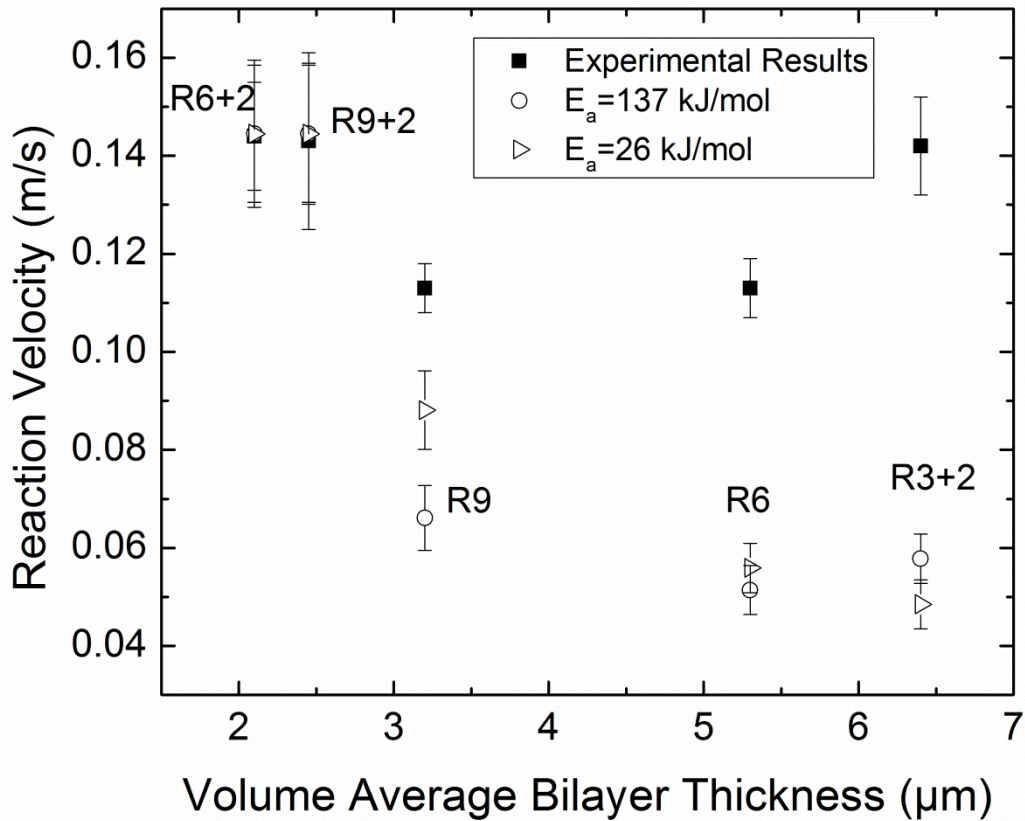


Figure 4.14 Predictions and measurements of reaction velocities are plotted versus volume average bilayer thickness. Predictions were made using an analytical solution from Armstrong and Koszywoski [36] and measured maximum temperatures from Figure 4.9. The pre-exponential term in the solution was obtained [18] by fitting to the R9+2 data and the rest of the predictions were allowed to vary with  $T_{\max}$  and the calculated volume average bilayer thickness.

where  $T$  is the maximum reaction temperature,  $T_o$  is room temperature,  $E_a$  is the reaction activation energy,  $R$  is the universal gas constant,  $A$  is a pre-exponential constant and  $\delta$  is the average diffusion distance, defined as a  $\frac{1}{4}$  of a bilayer. We can use Equation 4.2 and the measured maximum temperatures to predict reaction velocities. We assume two different activation energies based on previous literature: Mann *et al* [25] computed  $E_a$  as 137 kJ/mol using reaction velocities measured for sputtered Ni/Al multilayer foils while

Du *et al* [29] computed  $E_a$  as 26 kJ/mol for Ni diffusion into molten Al. By matching the prediction of the velocity of R9+2 to its experiment, we determined the pre-exponential A to be approximately  $1.5 \times 10^{-6} \text{ m}^2/\text{s}$ , reasonably close to a commonly accepted value of  $D_o$ ,  $2.18 \times 10^{-6} \text{ m}^2/\text{s}$  [20,30,31].

The results of the two calculations are shown in Figure 4.14. The predicted velocities do not agree with the experimental results. They decrease too quickly as bilayer thickness increases on moving from R9+2 to R9 and R6, and they do not increase again for R3+2. The variations in  $T_{\text{max}}$  are not capable of explaining the corresponding variations in reaction velocities within the context of this model. The model of Armstrong and Koszysowsky [28] assumes steady propagation, as do most analytical and numerical models [20,25,30–38]. More sophisticated numerical modeling [39] is likely needed to simulate unsteady reaction propagation effectively. A later chapter will investigate the mechanism of unsteady reaction propagation via high-speed video analysis.

## References

- [1] Knepper R, Snyder MR, Fritz G, Fisher K, Knio OM, Weihs TP. *Journal of Applied Physics* 2009;105:083504.
- [2] Reiss ME, Esber CM, Van Heerden D, Gavens AJ, Williams ME, Weihs TP. *Materials Science and Engineering: A* 1999;261:217.
- [3] Besnoin E, Cerutti S, Knio OM, Weihs TP. *Journal of Applied Physics* 2002;92:5474.
- [4] Rogachev AS, Grigoryan AÉ, Illarionova E V., Kanel IG, Merzhanov AG, Nosyrev AN, Sachkova N V., Khvesyuk VI, Tsygankov PA. *Combustion, Explosion, and Shock Waves* 2004;40:166.
- [5] Floro JA. *Journal of Vacuum Science & Technology A: Vacuum, Surfaces, and Films* 1986;4:631.
- [6] Dyer, T S, Munir, Z A, Ruth V. *Scripta Metallurgica et Materialia* 1994;30:1281.
- [7] Ma E, Thompson C V., Clevenger LA, Tu KN. *Applied Physics Letters* 1990;57:1262.
- [8] Hebert RJ, Perepezko JH. *Scripta Materialia* 2004;50:807.
- [9] Sieber H, Wilde G, Perepezko J. *Journal of Non-Crystalline Solids* 1999;250-252:611.
- [10] Sieber H, Park JS, Weissmüller J, Perepezko JH. *Acta Materialia* 2001;49:1139.
- [11] Saito Y, Utsunomiya H, Tsuji N, Sakai T. *Acta Materi* 1999;47:579.
- [12] Eizadjou M, Kazemi Talachi A, Danesh Manesh H, Shakur Shahabi H, Janghorban K. *Composites Science and Technology* 2008;68:2003.
- [13] Mozaffari A, Danesh Manesh H, Janghorban K. *Journal of Alloys and Compounds* 2010;489:103.
- [14] Qiu X, Liu R, Guo S, Graeter JH, Kecskes L, Wang J. *Metallurgical and Materials Transactions A* 2009;40:1541.
- [15] Dreizin EL. *Progress in Energy and Combustion Science* 2009;35:141.
- [16] Bazyn T, Glumac N, Krier H, Ward TS, Schoenitz M, Dreizin EL. *Combustion Science and Technology* 2007;179:457.

- [17] Badiola C, Schoenitz M, Zhu X, Dreizin EL. *Journal of Alloys and Compounds* 2009;488:386.
- [18] Stamatis D, Jiang X, Beloni E, Dreizin EL. *Propellants, Explosives, Pyrotechnics* 2010;35:260.
- [19] Weihs TP. Self-propagating Reactions in Multilayer Materials, in: *Handbook of Thin Film Process Technology*. Bristol: TOP; 1998.
- [20] Salloum M, Knio OM. *Combustion and Flame* 2010;157:288.
- [21] McDonald JP, Hodges VC, Jones ED, Adams DP. *Applied Physics Letters* 2009;94:034102.
- [22] Gavens AJ, Heerden D Van, Mann AB, Reiss ME, Weihs TP. *Journal of Applied Physics* 2000;87:1255.
- [23] Bordeaux F, Yavari R. *Z Metallkunde* 1990;81:130.
- [24] Dinda GP, Rösner H, Wilde G. *Scripta Materialia* 2005;52:577.
- [25] Mann AB, Gavens AJ, Reiss ME, Van Heerden D, Bao G, Weihs TP. *Journal of Applied Physics* 1997;82:1178.
- [26] Battezzati L, Pappalepore P, Durbiano F, Gallino I. *Acta Materialia* 1999;47:1901.
- [27] Boer RF, Boom R, Mattens WCM, Miedema AR, Niessen AK. *Cohesion in Metals*. Amsterdam: Elsevier Ltd; 1988.
- [28] Armstrong M, Koszykowski R. *Combustion and Plasma Synthesis of High-Temperature Materials*. New York: VCH; 1990.
- [29] Du Y. *Materials Science and Engineering A* 2003;363:140.
- [30] Salloum M, Knio OM. *Combustion and Flame* 2010;157:436.
- [31] Salloum M, Knio OM. *Combustion and Flame* 2010;157:1154.
- [32] Gavens AJ, Heerden D Van, Mann AB, Reiss ME, Weihs TP. *Journal of Applied Physics* 2000;87:1255.
- [33] Gunduz IE, Fadenberger K, Kokonou M, Rebholz C, Doumanidis CC, Ando T. *Journal of Applied Physics* 2009;105:074903.

- [34] Makino A, Law CK. Twenty-Fourth Symposium (International) on Combustion/The Combustion Institute, 1992/pp. 1883-1891, in: Twenty-Fourth Symposium on Combustion. 1992.
- [35] Makino A, Law CK. Combustion and Flame 1995;101:551.
- [36] Law CK. Combustion Science and Technology 2006;178:335.
- [37] Hardt AP, Phung P V. Combustion and Flame 1973;21:77.
- [38] Atzmon M. Metallurgical and Materials Transactions A 1992;23:49.
- [39] Alawieh L, Knio OM, Weihs TP. Journal of Applied Physics 2011;110:013509.

## **Chapter 5 Mechanical Fabrication and Characterization of Ni/Al Laminate Powders**

### **5.1 Introduction**

Laminate composite reactive materials are typically fabricated with a uniform distance between the two layers using physical-vapor deposition (PVD) techniques such as magnetron sputtering [1–6] or electron-beam deposition [7–9]. Other investigators, though, have used mechanical methods to compress and bond alternating sheets of metal via rolling, hammering or swaging [10–16]. In general, bottom-up PVD methods produce finer and more uniform microstructures while top-down mechanical deformations create coarser, non-uniform microstructures.

Over the last decade researchers have also fabricated reactive particles that contain both reactants. Examples include high-energy arrested ball-milled composite particles [17–20] and core-shell particles [26]. A key advantage of such composite particles is that one can independently control the rates of atomic diffusion and thermal diffusion during reaction propagation by varying two geometric parameters. The average reactant spacing within the particles controls the rate of atomic mixing while the average particle diameter controls the rate of the thermal diffusion [21,22]. Since both parameters can be varied independently, composite reactive particles allow for more control over propagation rates in powder compacts, compared to compacts with elemental or single-phase particles. In this latter case, the rates of atomic and thermal diffusion both depend on particle diameter and cannot be varied independently.

Here an alternative, two-step process to fabricate reactive composite powders is presented. First, we cold-roll alternating sheets of Ni and Al to create a bulk laminate

structure, which allows us to tailor the reactant spacing through the number of rolling passes. Then, we grind the foils into powders and sieve them to produce a range of particle sizes for testing. We investigate the change in reactive behavior of the particles as a function of both original foil microstructure and average particle diameter.

## 5.2 Experimental Methods

All foils and powders were fabricated and characterized using methods described in Chapter 2. The mass fraction of R6+2 powders produced by blending is shown in Figure 5.1. Any subsequent modeling is described later in this chapter.

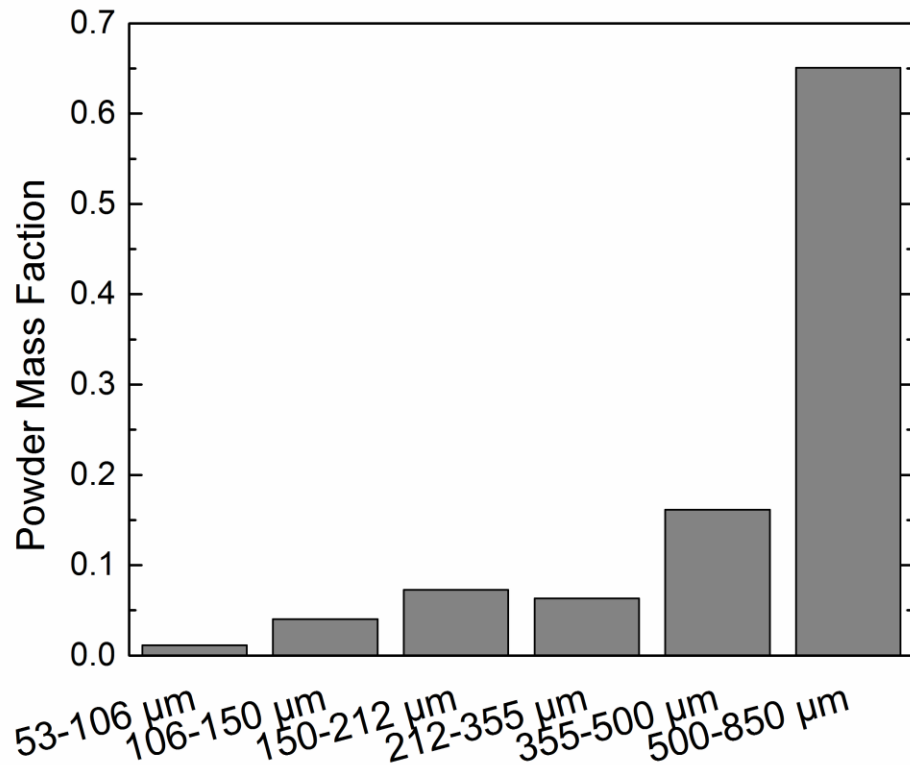


Figure 5.1 Weight fraction of various R6+2 powder size ranges after blending. Typically the largest powder sizes are obtained from the blending, as over 80% of the powders have a diameter greater than 500 µm.

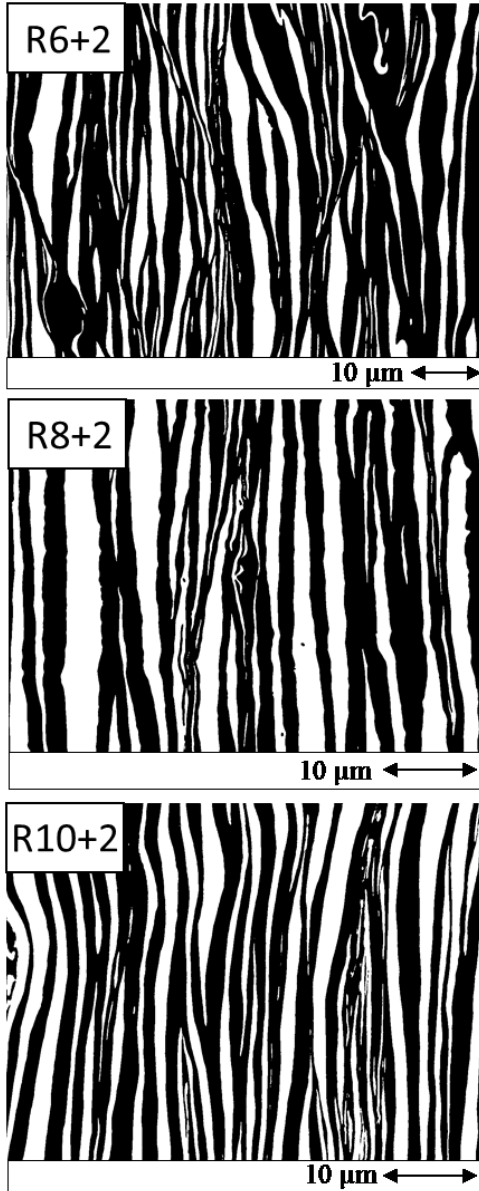


Figure 5.2 Scanning electron micrographs for each of the 3 initial foils. From top to bottom: R6+2, R8+2 and R10+2. The micrographs are thresholded to black and white with black representing Al and white representing Ni.

### 5.3 Results

Sample images of the microstructure resulting from each rolling condition are shown in Figures 5.2 (a)-(c). Bilayer thickness decreases as more rolling passes are

employed, but the percent reductions decrease with additional rolling passes. Table 5.1 lists results from the microstructural analysis of the 20 SEM images taken for each of the three foil samples. The first column displays the type of rolled material and the second shows the volume average bilayer thickness and the standard deviation. The standard deviation represents the variation in the bilayer thickness measured for each of the 20 SEM images taken for each sample. Note that the average bilayer varies from a high of 2.9 +/- 0.7  $\mu\text{m}$  for sample R6+2 to a low of 1.8 +/- 0.7  $\mu\text{m}$  for sample R10+2.

The physical densities of the powders vary with particle size as shown in Figure 5.3, but the variations differ for each sample. R6+2 powders skew Ni-rich at smaller particle sizes, while small R8+2 powders skew Al-rich. R10+2 powders have a density near 5.2 g/cc, which matches the theoretical density of 5.2 g/cc, based on the starting Ni and Al foil thicknesses. A “Particle Average” value is also shown in Figure 5.3 and represents the sum of each particle size’s mass fraction (Figure 5.1) multiplied by its physical density.

Table 5.1 Volume average bilayer thickness for each of the progenitor foils. The composite name is RX+Y where X is the number of 50% thickness reductions at 50% reduction per pass, and Y is the number of additional 50% thickness reductions done at 20% reduction per pass. The volume average bilayer thickness was determined from a numerical code and the standard deviation represents the variation of the values obtained from 20 different micrographs of the same sample.

|       | Volume Average Bilayer Thickness ( $\mu\text{m}$ ) |
|-------|--|
| R6+2  | 2.4 +/- 0.7  |
| R8+2  | 2.0 +/- 0.7  |
| R10+2 | 1.8 +/- 0.7  |

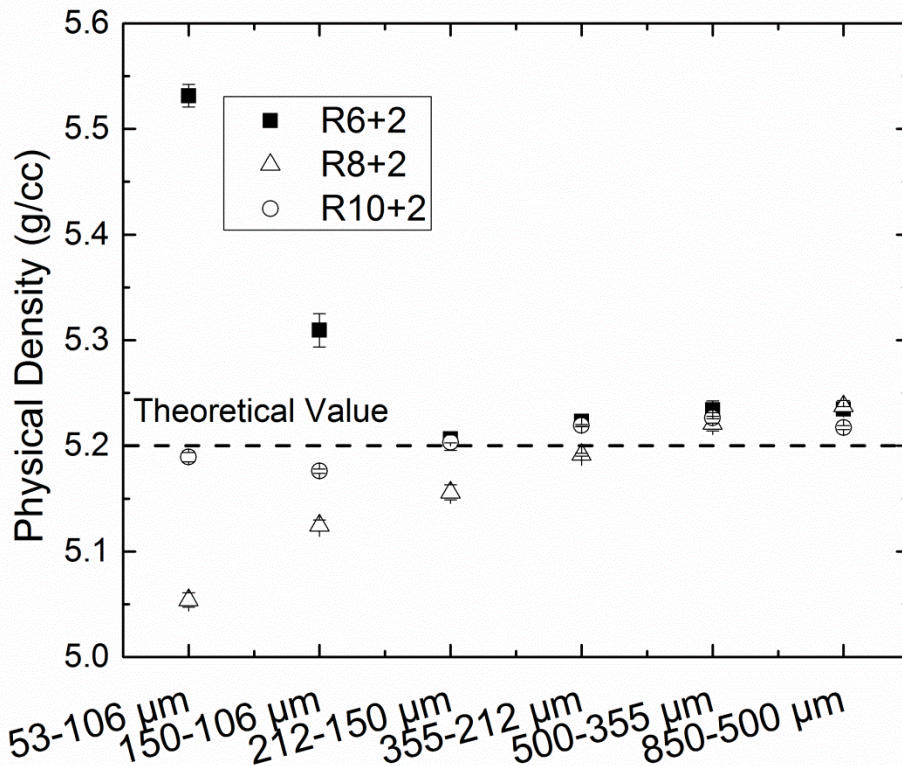


Figure 5.3 Physical density of the 3 types of powders by particle size. R6+2 skews Ni-rich at smaller particle sizes while R8+2 skews slightly Al-rich. R10+2 maintains a density close to the theoretical value of 5.2 g/cc. The “Particle Average” value is a mass weighted average of all of the powder size densities. Little difference is seen between it and the largest particle sizes, suggesting that the deviations seen at the smallest particle sizes do not significantly impact the averages for all particles or the values for the rolled foils, due to their low mass fraction.

To further explore variations in particle density, density was measured for various sample sizes of powder for the smallest and largest R6+2 powders. The resulting coefficients of variance (CoV) are shown in Figure 5.4 as a function of sample size. Note that 53-106 μm powders have a higher CoV in all sample sizes compared to the 500-850 μm powders. This difference suggests that the smallest particles have a wider range of densities among their individual particles. We also investigated the smallest R6+2

particle sizes by passing an electromagnet over a population of powders to separate

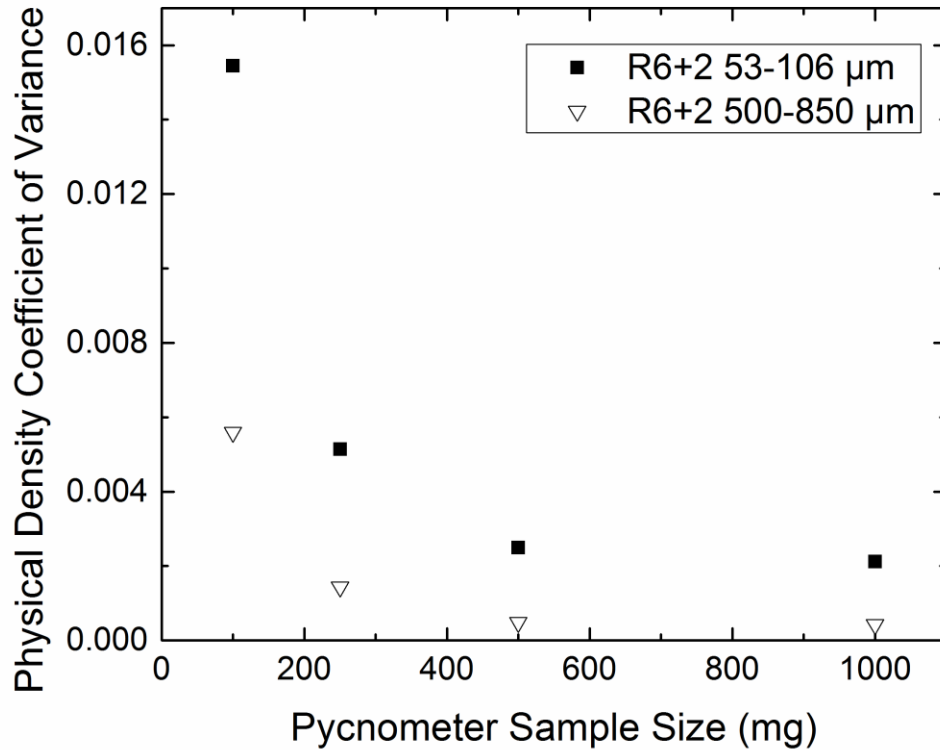
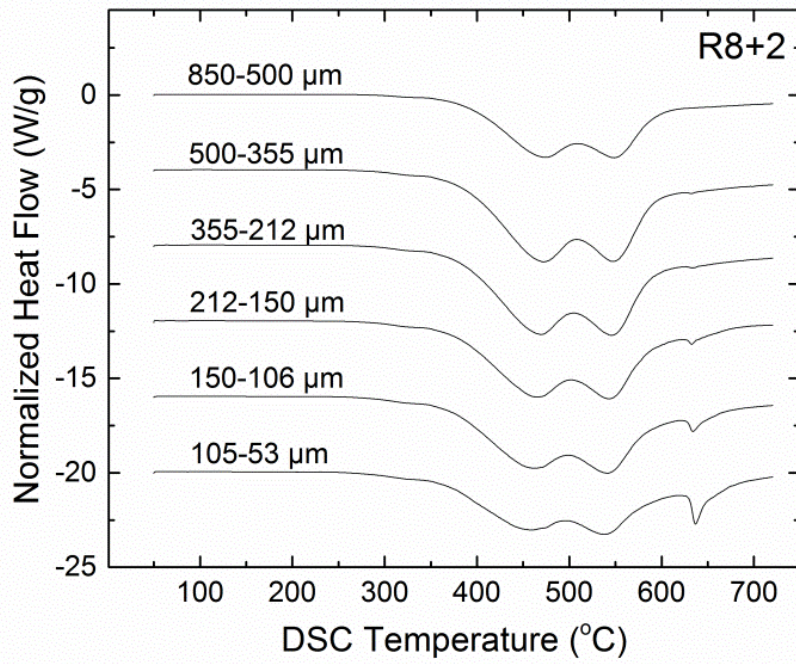
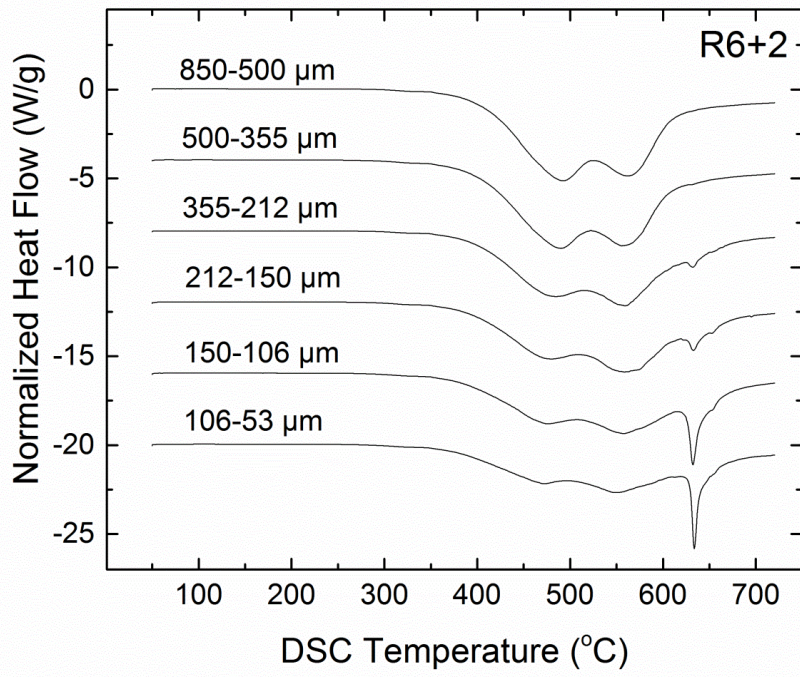


Figure 5.4 Coefficient of variance (CoV) of the physical density measurements as a function of sample size for both R6+2 53-106  $\mu\text{m}$  and 500-850  $\mu\text{m}$  powders. The larger CoV's for the smaller particle sizes suggests the smaller particles have a wider range of densities.

Ni-rich powders from Al-rich powders, as they would be more likely to stick to the magnet. We isolated a 100 mg population of powders with a density of 5.79 g/cc, which is much higher than the mean population density of 5.52 g/cc for these small particles.



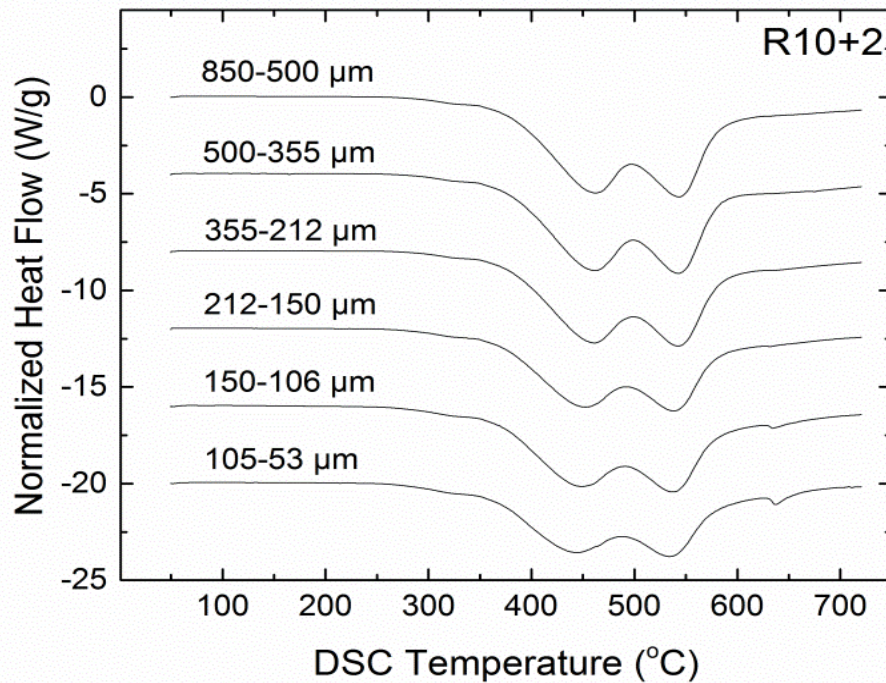


Figure 5.5 (a)-(c) DSC curves for the 3 different powder microstructures and particle sizes. The first of the double-bottomed exotherms corresponds to the formation of  $\text{Al}_3\text{Ni}$  and the second is the formation of  $\text{Ni}_2\text{Al}_3$  and  $\text{NiAl}$ . The double-bottomed exotherm gradually diminishes with smaller particle sizes and a much sharper peak at  $640^\circ\text{C}$  becomes prominent, corresponding to the melting and mixing of elemental Al. This effect is strongest for powders with the coarsest microstructure (R6+2.)

Multiple DSC scans were run on each of the powder size ranges and typical scans are plotted in Figures 5.5 (a) through (c). All of the particle sizes show two broad exotherms between  $400^\circ\text{C}$  and  $700^\circ\text{C}$ ; however, as the particle size decreases, these two exotherms become broader and shallower, and a large, sharp exotherm appears at  $640^\circ\text{C}$ .

Based on symmetric X-ray diffraction (XRD) of samples that were

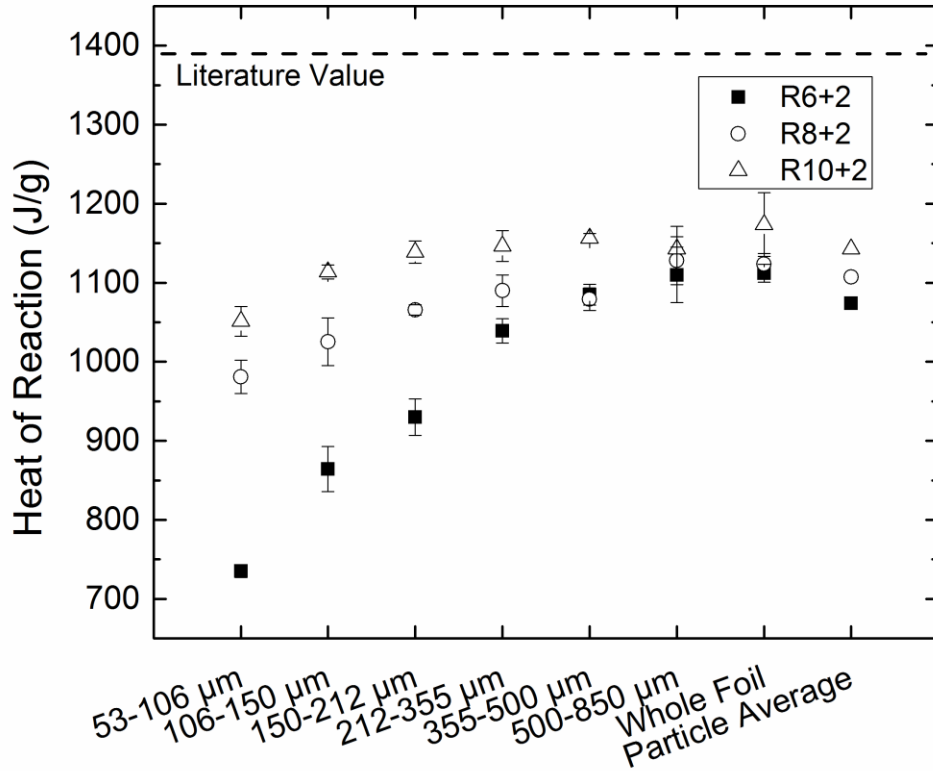


Figure 5.6 Integrated heats from the DSC curves in Figures 5.5 (a)-(c). The measured heat of reaction decreases with the particle size, with the largest decrease seen for the R6+2 powders. This correlates with the reduction of the double-bottomed exotherm and the presence of a sharp exotherm at 640 °C. The heat evolved for each powder size range is mass averaged using Figure 5.1 to determine the weighted “Particle Average” shown in this figure.

heated just beyond the peak temperatures and then quenched, the first broad peak corresponds to the formation of  $\text{NiAl}_3 + \text{Ni}$  and the second broad peak is the formation of the  $\text{Ni}_2\text{Al}_3 + \text{NiAl} + \text{Ni}$ . However, XRD scans of powders heated just below and just above the pronounced exotherm at 640 °C show there is elemental Al present just before the peak and none after, suggesting Al is melting and mixing with Ni during this exotherm. Powders without the sharp exotherm show no elemental Al at these temperatures.

The heats of reaction, obtained by integrating the curves in Figures 5.5 (a) through (c), are plotted in Figure 5.6 and show that the heat released is reasonably

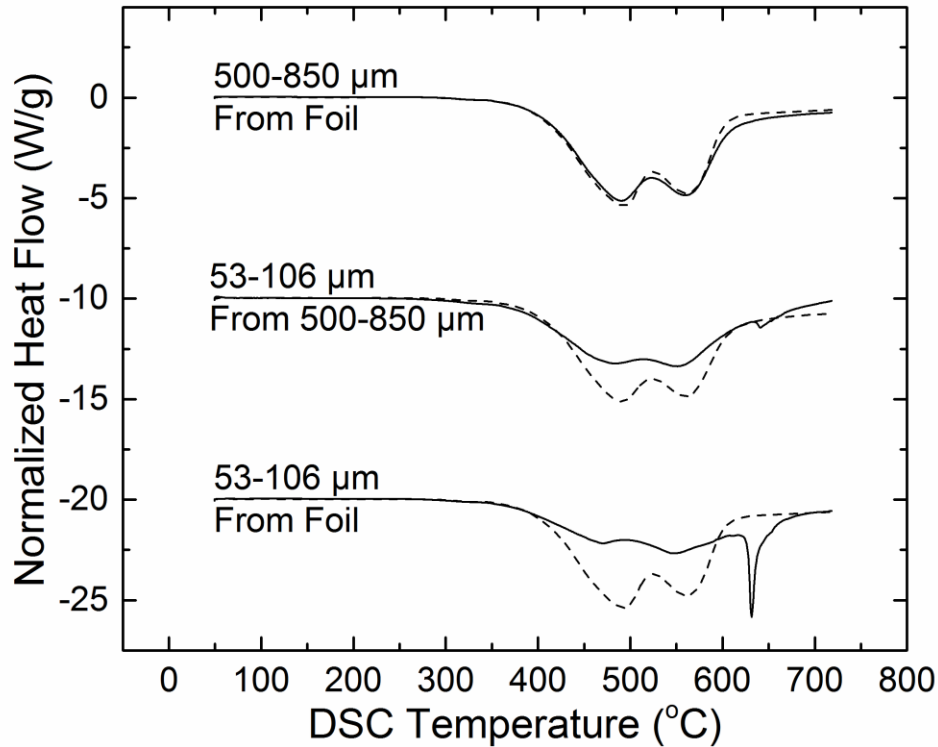


Figure 5.7 DSC scan of R6+2 53-106  $\mu\text{m}$  powders ground from large, 500-850  $\mu\text{m}$  powders compared with 500-850  $\mu\text{m}$  and 53-106  $\mu\text{m}$  powders ground from the foils. Instead of a large exotherm at 640  $^{\circ}\text{C}$ , the small particles ground from large particles show a much smaller exotherm at 640  $^{\circ}\text{C}$ , and its integrated heat (1051 J/g) is much closer to that of the large particles and bulk foil.

constant for the largest particle sizes, but drops off for smaller particle sizes. Furthermore, the drop-off is more pronounced for R6+2 powders, which have the largest volume average bilayer thickness. Heats of reaction were also measured for the rolled foils and are similar to the largest particles for each sample type. All measured heats of reaction are lower than the literature value, which is expected as the powders (and foils)

cannot fully react in DSC scans to 725°C. More stored energy will be released at high temperatures when the metastable Ni<sub>2</sub>Al<sub>3</sub> and Ni phases transform to the stable B2 NiAl intermetallic. A “Particle Average” value is also shown in Figure 5.6 and represents the sum of each particle size’s mass fraction multiplied by its measured heat of reaction.

To further probe the presence of the sharp exothermic peak at 640 °C, we compare small R6+2 particles that come from two different sources. The first source is R6+2 foils; the second source is large R6+2 particles that ranged in diameter from 500 to 850 μm. Both sources were ground to create 53-106 μm powders, and the powders were heated in the DSC in a similar manner. The resulting DSC curves appear in Figure 5.7 along with DSC curves for the source material. Results for the large, 500-850 μm powders are also shown for comparison. For all three sets of curves in Figure 5.7, the solid lines are DSC curves for the resulting powders, while the dotted lines are DSC curves for the source materials, from which the powders were ground. Therefore the top set of curves compare 500-850 μm powders to the initial foil from which they were ground. The middle set compares 53-106 μm powders to the 500-850 μm powders from which they were ground. Lastly, the bottom set of curves compares 53-106 μm powders to the initial foil from which they were ground. Note that the large exotherm at 640 °C is much less prominent for the 53-106 μm powders when they are ground from the large particles than when they are ground from the initial foil. Furthermore, the mass density of the 53-106 μm powders ground from large particles is 5.2 g/cc, similar to the parent foils and in contrast to the Ni-rich 53-106 μm powders ground from the whole foil that have a mass density of 5.53 g/cc. The following discussion examines this unexpected result and the trends in DSC curve shape and heat release as a function of particle size.

## **5.4 Discussion**

### **5.4.1 Physical Density**

None of the micrographs show evidence of voids and the average densities for the largest particles and the foils fall slightly above the expected value. Therefore, with an assumption of full-density in the particles we attribute any deviations in their physical density from the expected value of 5.2 g/cc to variations in their binary chemistry. With this assumption in mind we note the density data in Figure 5.3 strongly suggests that at smaller particle sizes R6+2 powders become increasingly Ni-rich and R8+2 powders trend Al-rich. The R10+2 powders have relatively constant Ni/Al ratios regardless of powder size. These variations with particle size imply that the grinding or blending of the three rolled foils yields particles with a unique microstructural and chemical makeup that is not a random sampling of the microstructure from the foil. We will now consider the other particle data with this hypothesis in mind.

### **5.4.2 DSC Curve Shapes**

The exothermic peak temperatures in DSC scans are known to vary with the average diffusion distance of reactants for a given sample chemistry, and when combined with quenching and XRD experiments a reaction sequence for a given diffusion distance and chemistry can be determined [23]. As expected, decreasing the diffusion distance or bilayer thickness through more rolling passes shifts the exotherms in Figure 5.5 to lower temperatures. However, as the particle size decreases below 355  $\mu\text{m}$ , a small peak becomes visible at 640 °C and the two broad exotherms increase in width and decrease in amplitude. This effect is strongest in the powders with the largest average bilayer thickness, R6+2, and is weakest for the R10+2 powders, which have the finest

microstructure. XRD scans were performed on DSC samples quenched at various temperatures to elucidate the different reaction sequences for all R6+2 powder size ranges. The two broad exotherms correspond first to the formation of  $\text{Al}_3\text{Ni} + \text{Ni}$  and then to the formation of  $\text{Ni}_2\text{Al}_3 + \text{Ni} + \text{NiAl}$ . The formation of the NiAl equilibrium phase is not completed during the DSC scans due to the limited temperature capability of the instrument, which has been seen before [24]. We also note that the sharp exotherm at 640 °C, seen for the smaller particles, appears to be associated with the melting of Al. X-ray diffraction of samples heated to just before the sharp exotherm show elemental Al while samples heated just beyond the exotherm do not. Further still, as the powder size decreases the elemental Al peaks in the X-ray diffraction scans increase in intensity and the size of the sharp exotherm in Figure 5.5 increases as well. This apparent variation in the amount of the Al that melts, as a function of particle size, also suggests that the foils breakup into large and small particles in a non-uniform manner.

#### 5.4.3 DSC Evolved Heats

The measured heats of reaction shown in Figure 5.6 are reasonably close in magnitude for the whole foil and the largest particle sizes, but values begin to drop off as the particle size decreases below 212  $\mu\text{m}$ . Note also that the decrease in measured heat is greatest for R6+2 powders, which have the largest volume average bilayer thickness. We argue that this drop-off in heat is caused mainly by the non-random breakup of the foils during blending and the formation of small particles with a high volume fraction of Ni-rich and Al-rich bilayers. However, before exploring this argument in more detail, we first consider an average heat for all of the particles.

Note that while the drop-off in heat with particle size is significant, the average heat for all particle sizes is very similar to the values measured for the foils and the largest particles. The average particle heat was calculated by convolving the mass fraction of each powder size range (Figure 5.1) with its measured heat for each foil type. The limited volume fraction of small particles results in the particle average heats falling only 4% below the values measured for the whole foils. We attribute the slightly lower particle averages to surface area effects that are most prominent in the small particles. Bilayers near the surface of particles are less likely to react completely compared to bilayers located within the interior of the particles. Since the particles have far more surface area on average than the foils, the effect will be more pronounced for the particles and heats will be slightly lower. We estimate an 8% decrease for the particle average, compared to the foils, based on the known ratios of bilayer thicknesses to particle diameters. This estimate agrees reasonably well with the difference between the foil and the particle average heats shown in Figure 5.6. However, this surface area effect is not strong enough to explain the far more significant drop-off in heat with particle size that also appears in Figure 5.6.

#### **5.4.4 Grinding Foils vs. Powders**

To further support the hypothesis that the foils breakup in a nonrandom manner during blending or grinding we fabricated the smallest R6+2 powders (53-106  $\mu\text{m}$ ) from two different sources: whole foils and the largest (850-500  $\mu\text{m}$ ) powders. Figure 5.7 compares DSC scans of the two resulting sets of powders to DSC scans of their R6+2 source material. DSC scans of the largest (850-500  $\mu\text{m}$ ) powders are also compared to their source material, the R6+2 foils. We first note that the scans of the largest particles

are very similar to the foils. Both the largest particles and the foils yield two large and broad exotherms that overlap as shown in the top set of curves. However, the smallest particles ground from the foils have very different scans from the foils as shown in the bottom set of curves. These 53-106  $\mu\text{m}$  particles have two shallow exotherms followed by one sharp exotherm at 640 °C that is attributed to the melting of Al. In contrast the 53-106  $\mu\text{m}$  powders ground from the larger of R6+2 particles have two more pronounced and broad exotherms followed by only a very small exotherm at 640 °C. Also, the powders ground from the larger R6+2 particles release 1051 J/g, compared to 723 J/g for the 53-106 powders ground from R6+2 foil. Thus, R6+2 53-106  $\mu\text{m}$  particles behave very differently depending on whether they are ground from whole foils or large particles. These comparisons support the hypothesis that foils breakup into large and small particles in a non-uniform manner.

#### **5.4.5 Non-Random Breakup**

The grinding of foils clearly leads to particles for which the average densities, DSC scans, and measured heats of reaction vary with particle size. In addition, the latter two variations are strongest for the R6+2 foils that have the largest volume average bilayer. These differences and trends could be attributed to three different factors that vary as a function of particle size: bilayer thickness, average particle chemistry or local bilayer chemistry.

If the smaller powders contain a higher volume fraction of large bilayers, compared to the original foils, then the mixing of Ni and Al and the formation of NiAl may be less complete in the smaller powders on heating to 725 °C. A smaller volume fraction of the Ni and Al layers would react in the larger bilayers and less heat would be

produced as particle size decreases and the average bilayer thickness increases. This effect would also be most pronounced in the R6+2 particles that are ground from foils with the largest average bilayer thickness. However, while a higher volume fraction of large bilayers in smaller particles does explain the trends in measured heats in Figure 5.6, it does not account for the subtle shift of the two broad exotherms in Figure 5.5. Note that as particle size decreases for all three materials, the two broad exotherms shift to lower temperatures suggesting that the volume average bilayer thickness actually decreases slightly as powders become smaller. Thus, variations in bilayer thickness with particle size cannot account for all of the observed trends.

Another possible explanation for the observed trends is a bimodal distribution in the density and chemistry of whole particles that grows more pronounced as particle size decreases. However, some of the particles would need to be more than 75 at% Al to see any Al melting during DSC scans, as the 3:1 Al:Ni intermetallic can form via solid-state diffusion for the bilayer thicknesses shown here [23]. Thus, the Al-rich particles would need a density lower than 3.82 g/cc, and this would imply that a significant population of powders have densities over 270 standard deviations from the mean. Such a distribution of particle densities does not seem plausible given the density results in Figure 5.3.

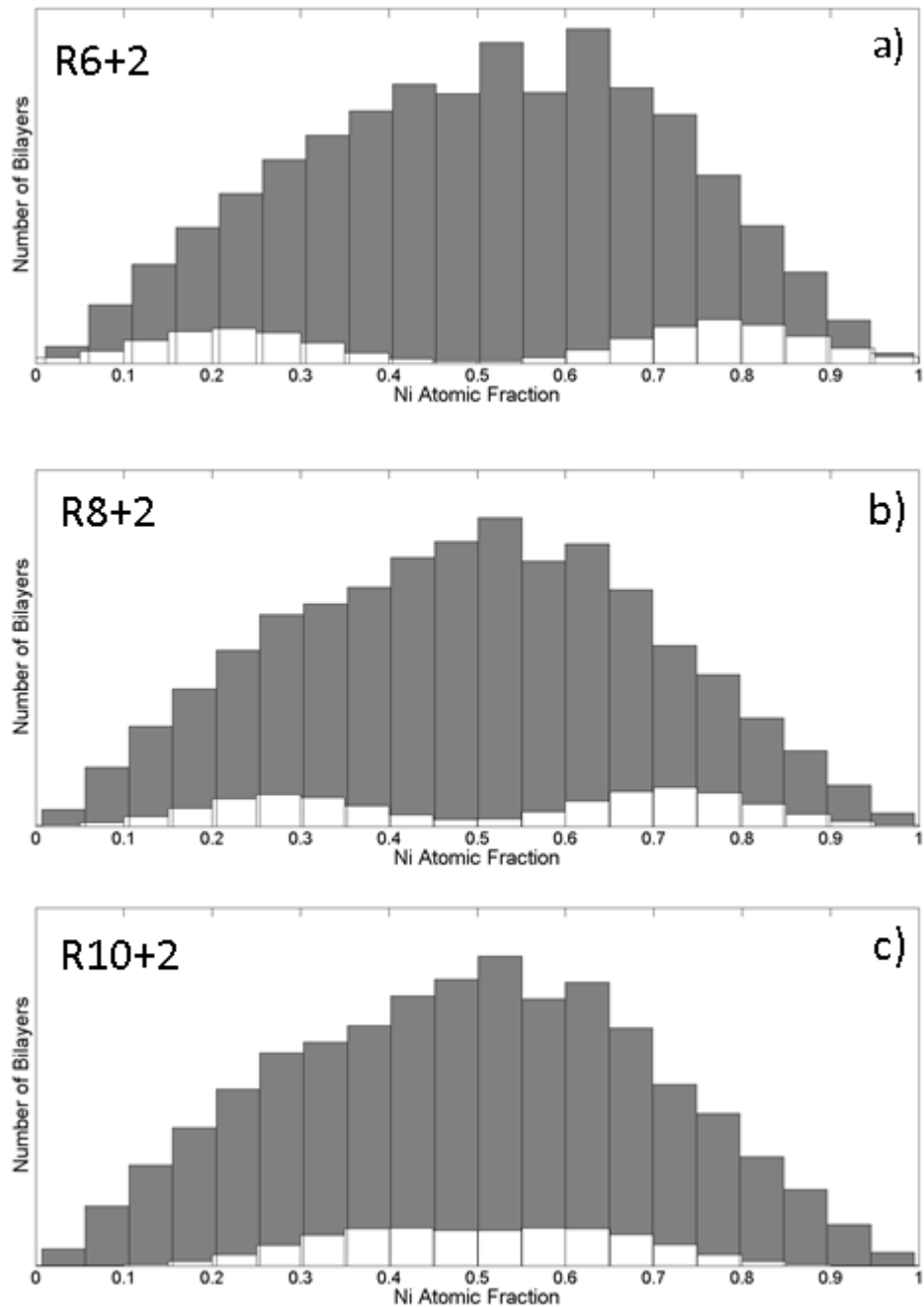


Figure 5.8 The total bilayer chemistry distributions (in gray) overlaid with modeled bimodal distributions (in white) to simulate the breakup in the smallest particle sizes for the three foils. The bimodal distributions are generated to correspond to the physical density of the powder size ranges by tailoring the relative heights of either the Ni-rich or Al-rich side.

As a third alternative we argue that very Al-rich and very Ni-rich regions do appear in individual bilayers in the foils, and a large fraction of the most Al-rich and Ni-

rich bilayers segregate into the smallest particle sizes during break-up. This nonrandom breakup of the foil can lead to small particles with enough Al-rich bilayers to show significant Al melting during DSC scans and large drops in measured heats. However, the fraction of both Al-rich and Ni-rich bilayers in each of the small particles must be relatively balanced to account for the measured particle densities shown in Figure 5.3. To support this hypothesis, we will simulate the densities and the heats of reactions of small particles by assuming the bilayers within the small particles have bimodal distributions of chemistry (Al-rich and Ni-rich) that are extracted from the chemistry distributions from the original foils.

#### **5.4.6 Microstructural Modeling**

As we cannot directly image and quantify the bilayer thicknesses and chemistries for individual powders, due to their random orientation in a mounting medium, we instead use the distribution of bilayer thicknesses and chemistries acquired from the SEM micrographs of the foils (Figure 5.2) to create simulated bimodal distributions for the smallest powders as shown in Figure 5.8.

The bimodal distributions, shown in Figures 5.8 (a)-(c) are generated by specifying the Ni atomic fractions of the Al-rich and Ni-rich particles, their standard deviations and their relative heights. We also ensure that they are a subset of the total distributions in Figure 5.8. The relative heights of the Al-rich and Ni-rich peaks are chosen to match the measured physical densities of the powders (Figure 5.3) and the spacing of the Al-rich and Ni-rich peaks away from the nominal 50:50 composition are

adjusted to see if the DSC heats in Figure 5.6 be explained. The peaks are centered on Ni atomic fraction values of 0.22 and 0.78 for R6+2, 0.28 and 0.72 for R8+2, and 0.38 and 0.62 for R10+2. Not surprisingly, the largest separation of peaks is needed for R6+2 powders that show the largest drop in DSC heats.

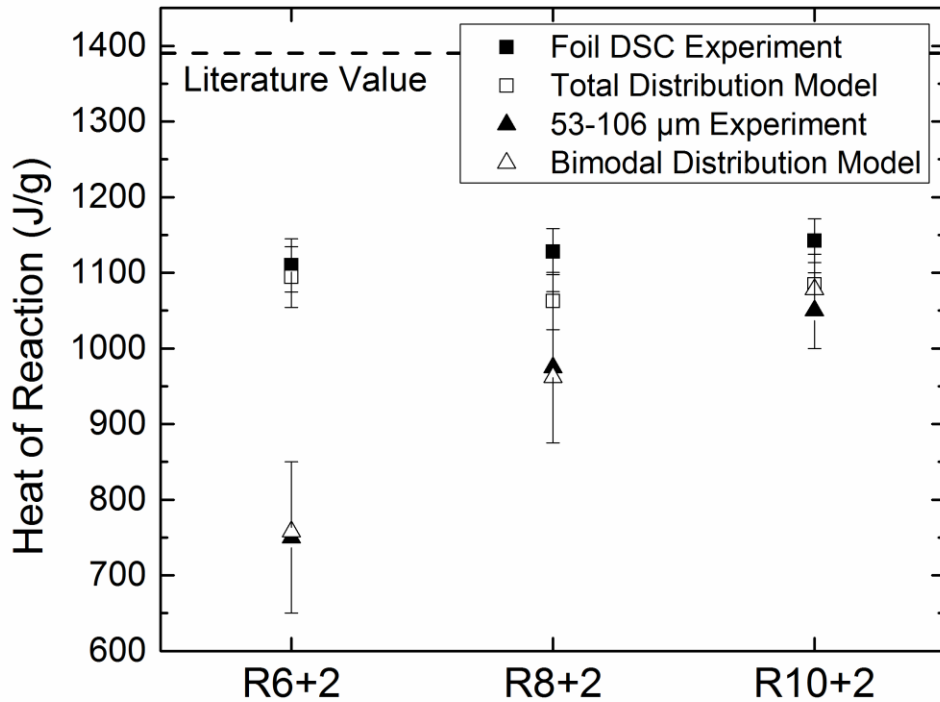


Figure 5.9 Comparison between measured and predicted heats of reaction for foils and the smallest powders. The “Total Distribution Model” uses each SEM image to tabulate every bilayer’s Ni atomic fraction and determine its predicted energy release in DSC by assuming only local chemistry equilibration. The error bars represent variations image to image. Both models assume complete mixing within each bilayer, but no intermixing between bilayers. The “Bimodal Distribution Model” calculates the heat release from the modeled bilayer chemistry bimodal distribution, used to simulate the resulting powder microstructure after breakup.

To predict heats of reaction from the bimodal distributions, we assume that each bilayer, Al-rich, Ni-rich or 50:50, reacts to achieve chemical equilibrium within itself. Diffusional mixing between bilayers is ignored. Every bilayer's heat release is determined by its local chemistry and linear fits between the enthalpies of formation of the known equilibrium Ni-Al phases [24]. In Figure 5.9, we assess the quality of these assumptions by calculating the heats of reactions for the complete foils, using the full distributions in Figure 5.8. Note that the "Total Distribution Model" and the measured heats of reaction ("Foil DSC Experiment") agree quite well and support the assumptions above.

Heats of reaction were calculated for the smallest powders using the bimodal distributions in Figures 5.8 and are shown in Figure 5.9 as well. Note that the calculated values, labeled as "Bimodal Distribution Model" agree very well with the measured values for the smallest particles, labeled "53-106  $\mu\text{m}$  Experiment." The agreement suggests that non-random breakup is a viable explanation for the trends in physical density, DSC curve shapes and heat release.

#### **5.4.7 Bilayers per Particle**

Given these composite particles show promise in commercial applications such as component bonding, structural energetics and chemical delays, the heat released during reaction is a key parameter for their application. We reconsider Figure 5.6, which shows the measured heats as a function of particle size, and remember that R6+2 samples show the largest drop-off in heat while R10+2 samples show the smallest as particle size decreases. However, if we instead plot the measured heats of reaction versus the average number of bilayers in each particle, using the volume average bilayer thickness and the

average particle size, the measured heats merge towards one curve, as shown in Figure 5.10. Furthermore, we see that the sharpest drop-offs in heat begin when there are fewer than ~150 bilayer per particle (marked with a dotted line.) Therefore, we believe that for any application, one should strive to obtain a sufficient number of bilayers in each particle to avoid significant reductions in stored energy and reaction properties. We hypothesize that more bilayers in each particle can offset the effects of preferential breakup, as sampling more of the microstructure forces a more uniform bilayer chemistry distribution in each particle.

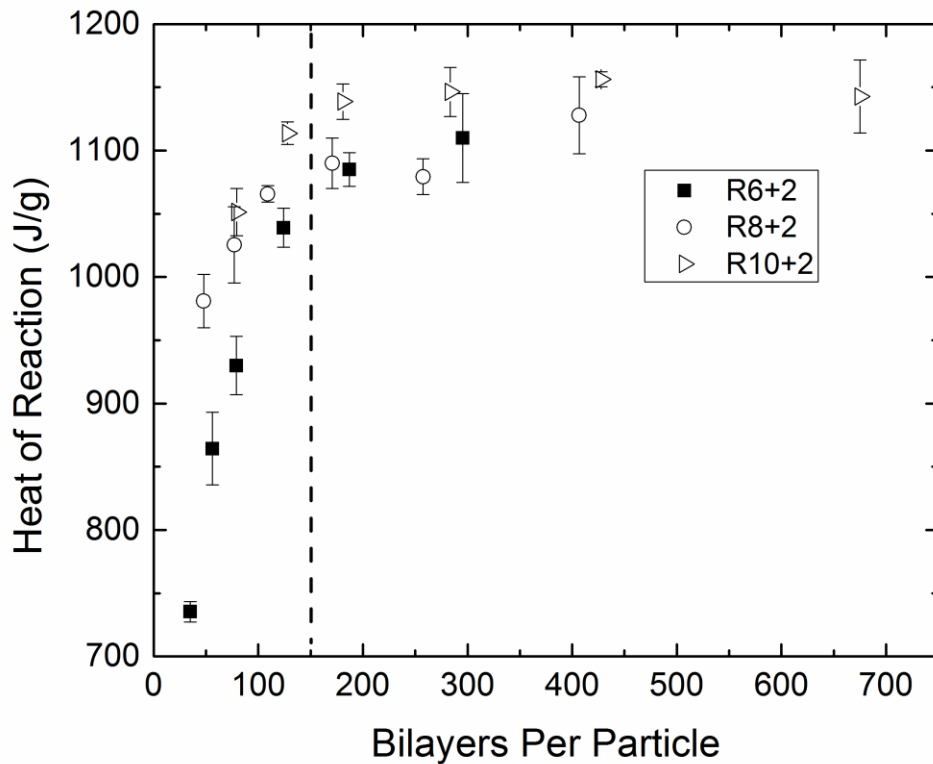


Figure 5.10 Measured heats of reaction (Figure 5.6) plotted versus bilayers per particle. All of the values fall close to one curve, and the sharpest drop is seen below 150 bilayers per particle.

## References

- [1] Knepper R, Snyder MR, Fritz G, Fisher K, Knio OM, Weihs TP. *Journal of Applied Physics* 2009;105:083504.
- [2] Reiss ME, Esber CM, Van Heerden D, Gavens AJ, Williams ME, Weihs TP. *Materials Science and Engineering: A* 1999;261:217.
- [3] Besnoin E, Cerutti S, Knio OM, Weihs TP. *Journal of Applied Physics* 2002;92:5474.
- [4] Rogachev AS, Grigoryan AÉ, Illarionova E V., Kanel IG, Merzhanov AG, Nosyrev AN, Sachkova N V., Khvesyuk VI, Tsygankov PA. *Combustion, Explosion, and Shock Waves* 2004;40:166.
- [5] Rogachev AS. *Russian Chemical Reviews* 2008;77:21.
- [6] Mann AB, Gavens AJ, Reiss ME, Van Heerden D, Bao G, Weihs TP. *Journal of Applied Physics* 1997;82:1178.
- [7] Floro JA. *Journal of Vacuum Science & Technology A: Vacuum, Surfaces, and Films* 1986;4:631.
- [8] Dyer, T S, Munir, Z A, Ruth V. *Scripta Metallurgica et Materialia* 1994;30:1281.
- [9] Ma E, Thompson C V., Clevenger LA, Tu KN. *Applied Physics Letters* 1990;57:1262.
- [10] Hebert RJ, Perepezko JH. *Scripta Materialia* 2004;50:807.
- [11] Sieber H, Wilde G, Perepezko J. *Journal of Non-Crystalline Solids* 1999;250-252:611.
- [12] Sieber H, Park JS, Weissmüller J, Perepezko JH. *Acta Materialia* 2001;49:1139.
- [13] Saito Y, Utsunomiya H, Tsuji N, Sakai T. *Acta Materi* 1999;47:579.
- [14] Eizadjou M, Kazemi Talachi A, Danesh Manesh H, Shakur Shahabi H, Janghorban K. *Composites Science and Technology* 2008;68:2003.
- [15] Mozaffari A, Danesh Manesh H, Janghorban K. *Journal of Alloys and Compounds* 2010;489:103.
- [16] Qiu X, Liu R, Guo S, Graeter JH, Kecskes L, Wang J. *Metallurgical and Materials Transactions A* 2009;40:1541.

- [17] Badiola C, Schoenitz M, Zhu X, Dreizin EL. *Journal of Alloys and Compounds* 2009;488:386.
- [18] Umbrajkar SM, Schoenitz M, Dreizin EL. *Propellants, Explosives, Pyrotechnics* 2006;31:382.
- [19] Bazyn T, Glumac N, Krier H, Ward TS, Schoenitz M, Dreizin EL. *Combustion Science and Technology* 2007;179:457.
- [20] Stamatis D, Jiang X, Beloni E, Dreizin EL. *Propellants, Explosives, Pyrotechnics* 2010;35:260.
- [21] Morsi K. *Materials Science and Engineering: A* 2001;299:1.
- [22] Fritz GM, Jores H, Weihs TP. *Combustion and Flame* 2011;158:1084.
- [23] Michaelsen C, Barmak K, Weihs TP. *Journal Physics D; Applied Physics* 1997;30:3167.
- [24] Boer RF, Boom R, Mattens WCM, Miedema AR, Niessen AK. *Cohesion in Metals*. Amsterdam: Elsevier Ltd; 1988.

## Chapter 6 Unsteady Reaction Propagation in Cold-Rolled Ni:Al Laminates

### 6.1 Introduction

Binary laminate composite materials have been investigated for multiple applications such as structural reactive components [1], combat armor [2] and reactive materials [3–14]. Specifically for reactive materials, a critical material parameter is the thickness of the two alternating layers within the composite, which is commonly called the bilayer thickness [5–12,15]. Typically, the bilayer thickness determines the ease of initiating a self-propagating reaction as well as its velocity, as the bilayer thickness controls the average interdiffusion distance [5,16–23]. This distance is thought to be  $\frac{1}{4}$  of the bilayer thickness.

The velocity of self-propagating reactions is important to many RM applications, such as joining or reactive fragments, and recent investigations have begun to probe the morphology of reaction fronts in simple binary laminate systems using high-speed cameras [24–26]. Some have found that when heat losses are high or the rate of reaction is low, the reaction front is no longer planar but becomes unsteady or spin-like [24–26,31, have you added the in situ observations]. Unsteady reaction morphologies have also been studied in powder compacts as their slower velocities make capturing the reaction front far easier [13,28–32]. In addition, efforts have been made to develop numerical models that can effectively predict unsteady reaction fronts [32,33].

McDonald *et al* [24] were the first to directly visualize the spin-like reactions fronts in Al/Co sputtered foils. Two different reaction morphologies were observed and which type appeared was reported to depend on the bilayer thickness of the reactive laminate foil. In foils with smaller bilayer thicknesses (66.4 nm), reactions progress by

single reaction bands propagating across the full width of the foil, parallel to the reaction front. The velocity of the reaction front depends on the width of the bands, their propagation speed, and the number that propagate concurrently from one edge of the foil to the other. In foils with larger bilayer thicknesses (250 nm) multiple bands nucleate along the reaction front and propagate parallel to the front until they impinge on one another. The impingement event often leads to the nucleation of a new band, ahead of the reaction front. Thus, in this case the velocity of the reaction front depends on the width of the reaction bands, their velocity, and the frequency of their nucleation ahead of the front. A later investigation by McDonald *et al* [25] showed similar unsteady reactions in Ni/Ti multilayers, as well as the impact of environment on reaction morphology due to oxidation.

This work explores unsteady reaction propagation in much thicker cold-rolled Ni/Al foils that contain a complex laminate microstructure. Instead of the uniform laminate microstructure found in the thinner sputter deposited reactive foils, the materials studied here have a nonuniform layering, where both the bilayer thickness and the local Al/Ni fraction vary. The propagation morphology is similar to the mode reported for the Al/Co multilayers with thicker bilayers, however the nucleation of new bands ahead of the reaction front appears random and is thought to be related to the nonuniformity of the layering.

## 6.2 Experimental Methods

### 6.2.1 Materials Fabrication and Characterization

Ni/Al cold-rolled laminates were fabricated and characterized as described in Chapter 2. The volume average bilayer thickness of the foils was measured with the ‘home-built’ MATLAB code described in Chapter 4.

### 6.2.2 High-speed Video Analysis

Local reaction propagations were analyzed using a freeware program, Tracker. A photograph before reaction initiation was used to determine the scale and each foil type was videoed three times. Five reaction bands were measured for each video.

Table 6.1 Volume average bilayer thickness, number average bilayer thickness, the coefficient of variance (COV) for the volume average and the volume average bilayer reduction percentages per pass are listed for each sample. The volume average coefficient of variance either drops or stays constant after rolling with additional 20% thickness reductions. In general, microstructural refinement decreases with each additional rolling pass.

|       | Volume Average Bilayer Thickness ( $\mu\text{m}$ ) | Volume Average Bilayer Coefficient of Variance | Volume Average Bilayer Reduction Percentage per Rolling Pass |                |                      |
|-------|--|--|--|----------------|----------------------|
|       |  |  | 50 % Reductions  | 20% Reductions | Three 20% Reductions |
| R6    | 5.2 +/- 1.8  | 0.35   | 29%  |                |                      |
| R6+2  | 2.4 +/- 0.7  | 0.29   |  | 12%            | 32%                  |
| R8    | 2.9 +/- 1.1  | 0.38   | 25%  |                |                      |
| R8+2  | 2.0 +/- 0.7  | 0.35   |  | 3%             | 9%                   |
| R10   | 2.3 +/- 0.9  | 0.39   | 1%   |                |                      |
| R10+2 | 1.8 +/- 0.7  | 0.39   |  | 4%             | 12%                  |

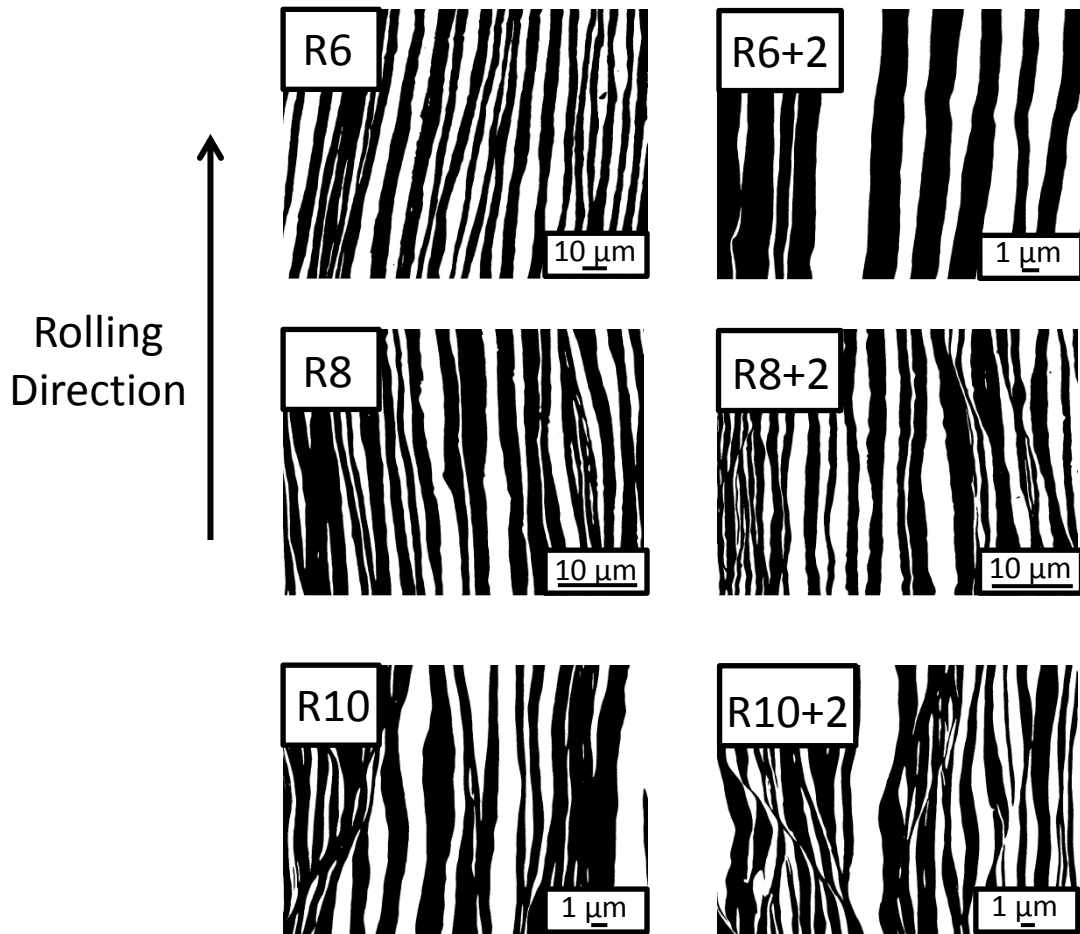


Figure 6.1 SEM images of the 6 composites. The images are thresholded to black and white; the white represents Ni and the black represents Al.

### 6.3 Results

SEM images of transverse cross-sections for the six cold-rolled samples are shown in Figure 6.1, with the rolling direction marked. Table 6.1 compiles microstructure data that was quantified for each sample using approximately 10 transverse cross-sections and 10 rolling cross-sections [35]. The first two columns display the volume average bilayer thickness and the coefficient of variance for the volume average bilayer thickness. In general, we note that bilayer thickness decreases as more rolling passes are employed. The relatively large standard deviations and

coefficients of variance (COV) confirm that rolled microstructures are nonuniform, but the COV either drops or stays constant following the additional 20% rolling passes, suggesting that the more gradual 20% reductions improve the uniformity of the microstructures. The last three columns in Table 6.1 list percent reductions in the volume average bilayer thickness per rolling pass. Note that the percent reduction per pass tends to decrease as the number of rolling passes increases and the material hardens.

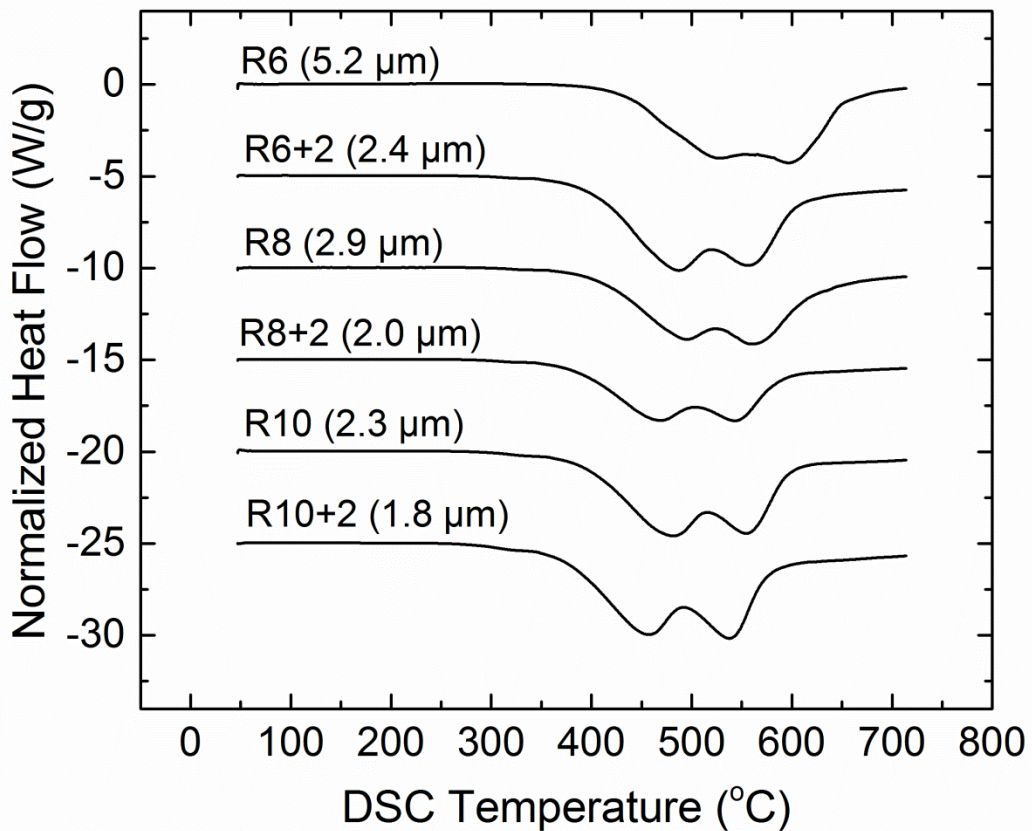


Figure 6.2 Differential scanning calorimetry (DSC) scans for the 6 rolled foils. The two major exothermic peaks shift to lower temperatures as the number of rolling passes increase and the volume average bilayer (in parentheses) decreases. The first peak corresponds to the formation of the  $\text{NiAl}_3$  intermetallic with excess Ni and the second peak is the formation of the  $\text{Ni}_2\text{Al}_3$  intermetallic + NiAl with excess Ni.

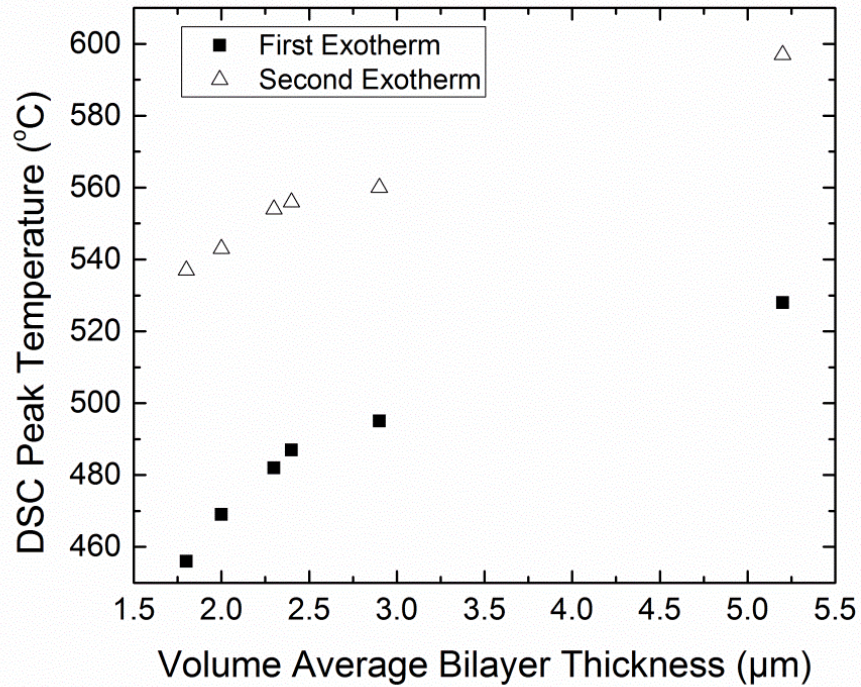


Figure 6.3 Peak temperatures for the DSC scans in Figure 3 are plotted versus volume average bilayer thickness for each sample. Note that peak temperatures decrease with additional rolling passes and correlate well with the calculated volume average bilayer thickness.

Multiple DSC scans were run on each of the six rolled composites and typical scans are plotted in Figure 6.2; all show two broad exotherms between 400 °C and 700 °C. Based on symmetric X-ray diffraction of samples that were heated just beyond the peak temperatures and then quenched, the first peak corresponds to the formation of

$\text{NiAl}_3 + \text{Ni}$  and the second peak is the formation of the  $\text{Ni}_2\text{Al}_3$  intermetallic +  $\text{NiAl}$  intermetallic +  $\text{Ni}$ . Note that the peaks for the two exotherms shift to lower temperatures as the amount of rolling increases and the bilayer thickness decreases. The trend of decreasing peak temperature with smaller bilayer thicknesses is displayed clearly in Figure 6.3. The heats of reaction, obtained by integrating the curves in Figure 6.1, are

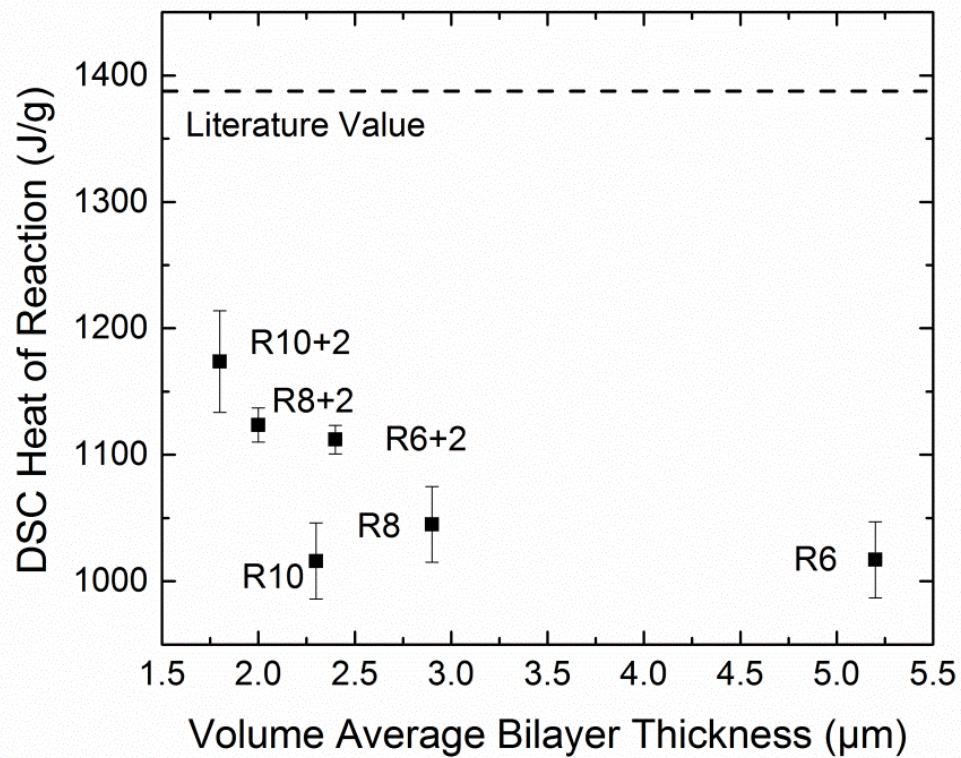


Figure 6.4 The curves in Figure 3 are integrated to yield the measured heats of reaction versus volume average bilayer thickness. In general, foils with more rolling release more heat. The literature heat for full intermixing is  $1380 \pm 40$  J/g [39].

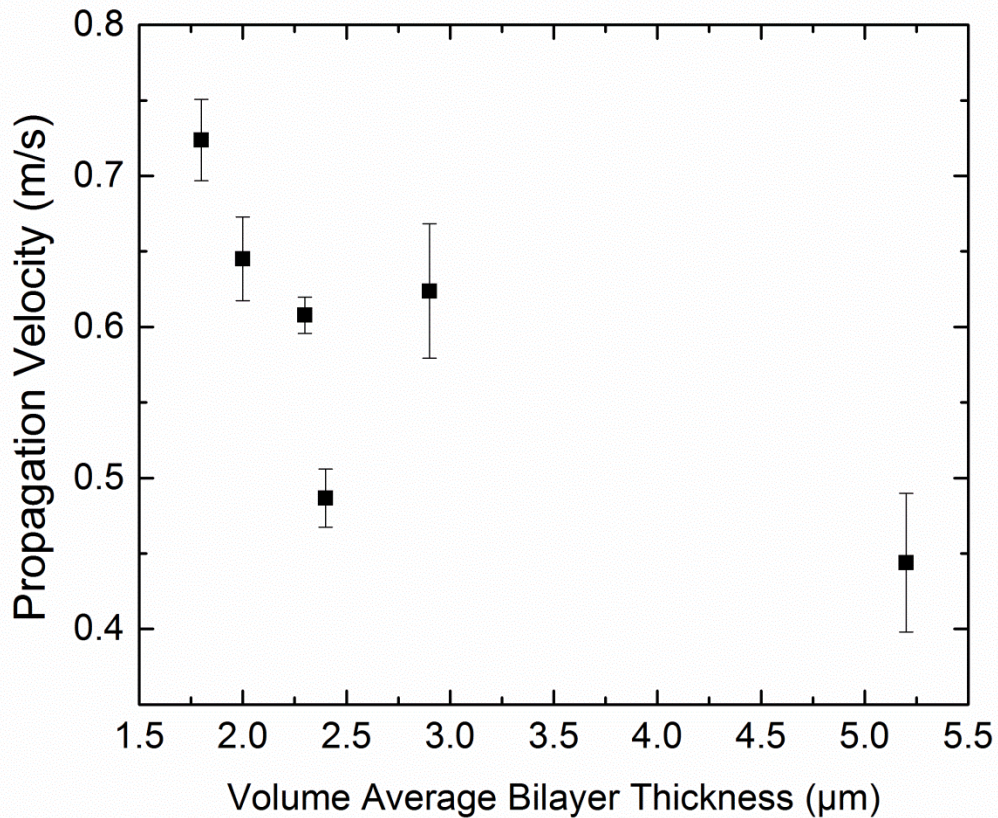


Figure 6.5 Reaction velocity vs. volume average bilayer thickness. In contrast to an earlier study on similar materials [36] the reaction velocity depends on the average microstructure rather than the type of rolling thickness reduction rate. However, this result agrees with most of the previously reported literature [5, 16-23].

plotted in Figure 6.4 and show that in general, as the foils receive more rolling reductions the heat release increases. The measured heats of reaction are lower than the literature values [36], as the foils cannot react fully in DSC scans to 725°C. More stored energy will be released at high temperatures when the metastable products transform to the stable NiAl intermetallic.

The self-propagating reaction velocities are plotted versus the volume average bilayer thickness in Figure 6.5. Foils with a coarser microstructure have a slower velocity while foils with the most refined microstructure have faster propagation rates.

The maximum temperatures during reaction are shown in Figure 6.6. All of the foils have a maximum temperature that is very close to the melting temperature of the NiAl intermetallic, within one or two standard deviations. The typical morphology of the unsteady reaction propagation is shown in Figure 6.7 through a series of four images taken over time. In the first image a reaction band nucleates ahead of the reaction front, as highlighted. The nucleus grows normal and parallel to the reaction front, and comes close to reaching its maximum width in the second image. From there, it grows mainly parallel to the reaction front until it is much longer than it is wide in the third image. The

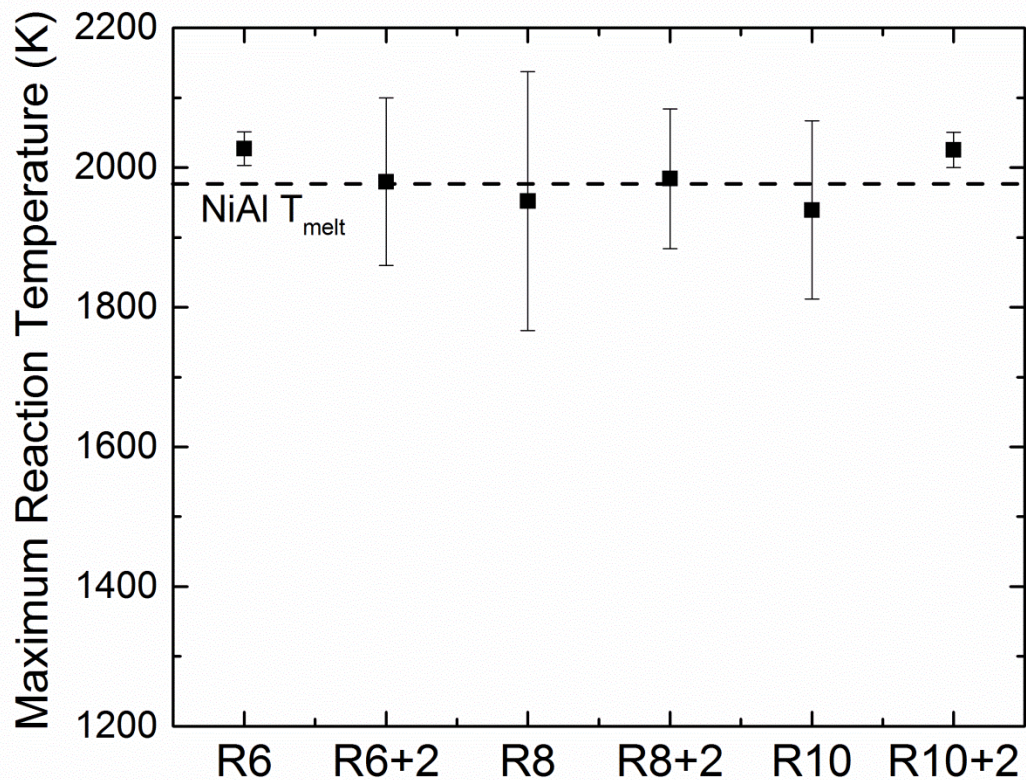


Figure 6.6 Maximum reaction temperature for each foil. All temperatures are near the melting temperature of the B2 NiAl intermetallic, which should serve as a ceiling as the reaction products are only partially molten.

band continues to elongate until it impinges on other growing bands as shown in the fourth image. Note that there is more than one frame between each snapshot. The growth rates of the reaction bands were determined by tracking the growth distance parallel and perpendicular to the net propagation direction. Figures 6.8 (a)-(f) show the band growth distance as a function of time for the six rolled foils. The points are averages of 15 growths tracked throughout the high-speed reaction videos.

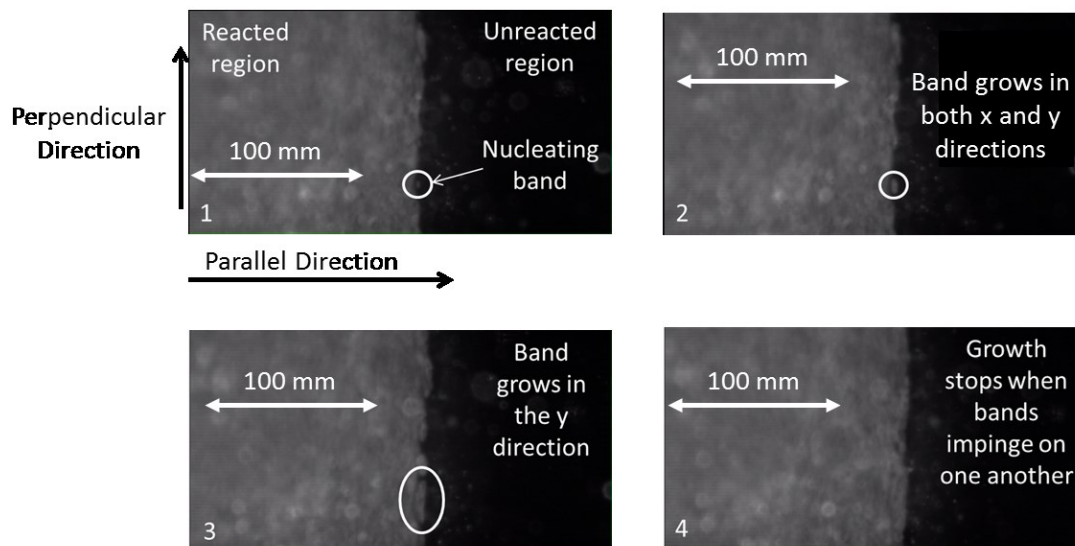
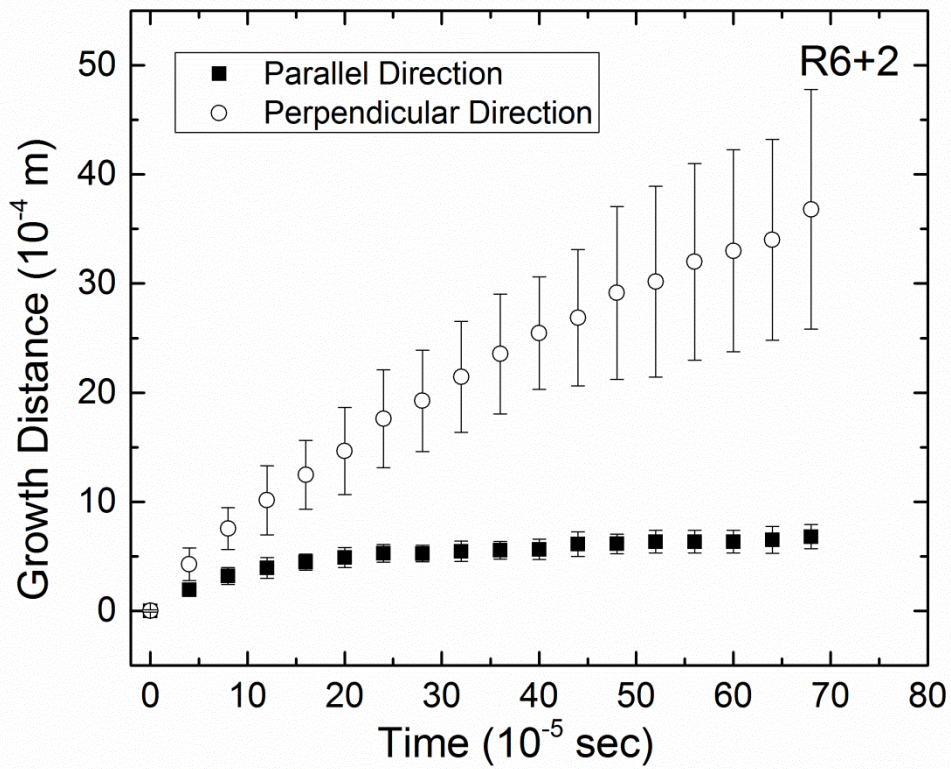
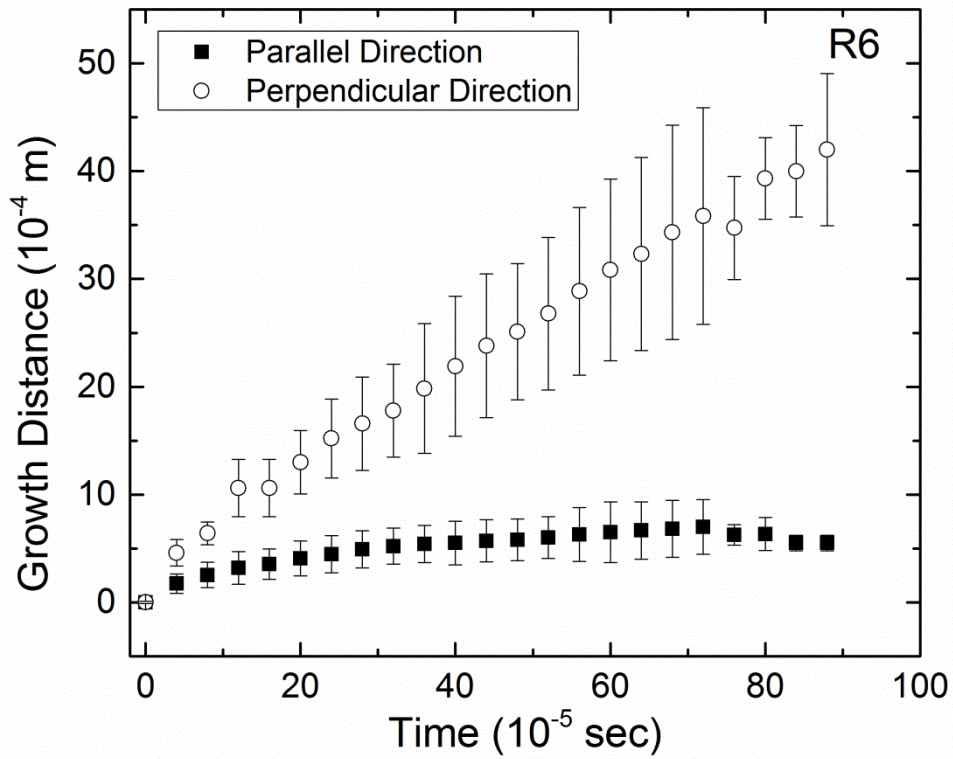
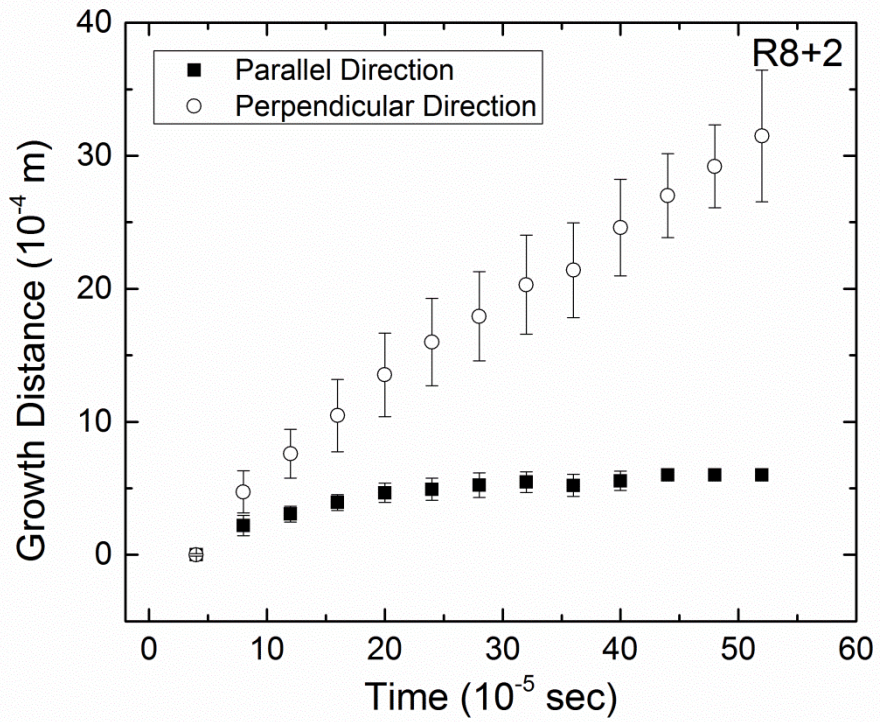
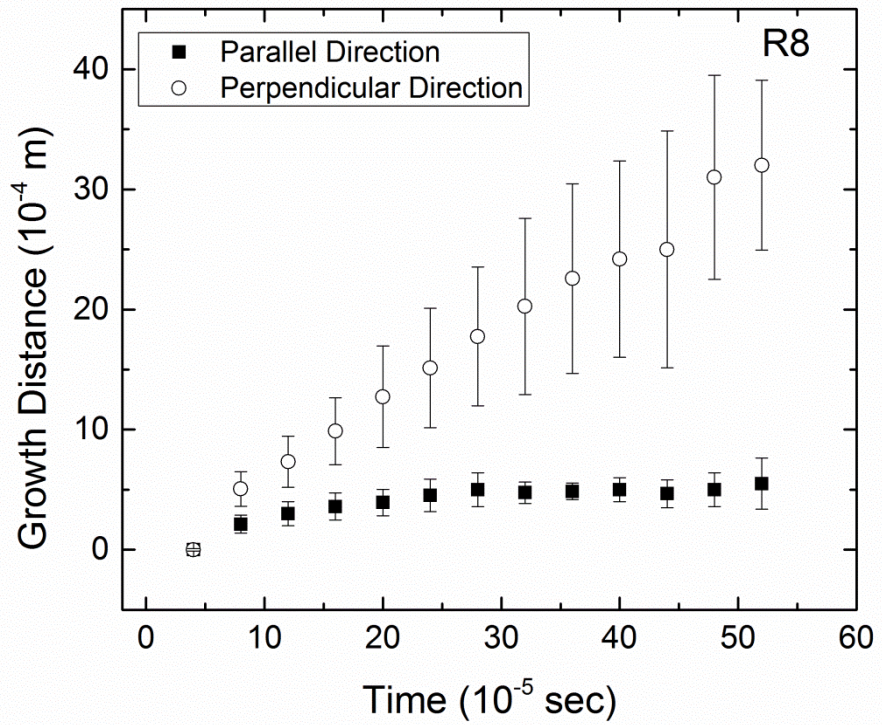


Figure 6.7 Reaction snapshots highlighting the unsteady reaction propagation morphology. The y direction is defined as perpendicular to the global propagation direction while the x direction is the global propagation direction. The four frames are noted with numbers to signify their order in the propagation timeline. First, a nucleation site occurs. Then, the band begins grows first in the x direction followed by the y direction. Growth finishes when bands impinge on one another. Note the random and non-periodic reaction nucleation sites.

Note that as the band growth distance increases, the number of points that constitute the average tend to drop as not all bands grow the same distance. For all six foils, the parallel growth distances are lower than those in the perpendicular direction.

Linear fits are made to the growth distance versus time plots in Figures 6.8 (a)-(f) to determine the average band growth velocities in both directions shown in Figure 6.9. The perpendicular band velocities closely track that of the net propagation velocity (Figure 6.5) while the parallel growth rates show no discernible trend. The perpendicular band velocity is overlaid with the net propagation rate in Figure 6.10. The net velocity is shown in blue while the perpendicular band velocity is black. The bands propagate roughly an order of magnitude faster than the net front. The following discussion will investigate the different band growth velocities and compare the trends seen in these foils to others seen in the literature.





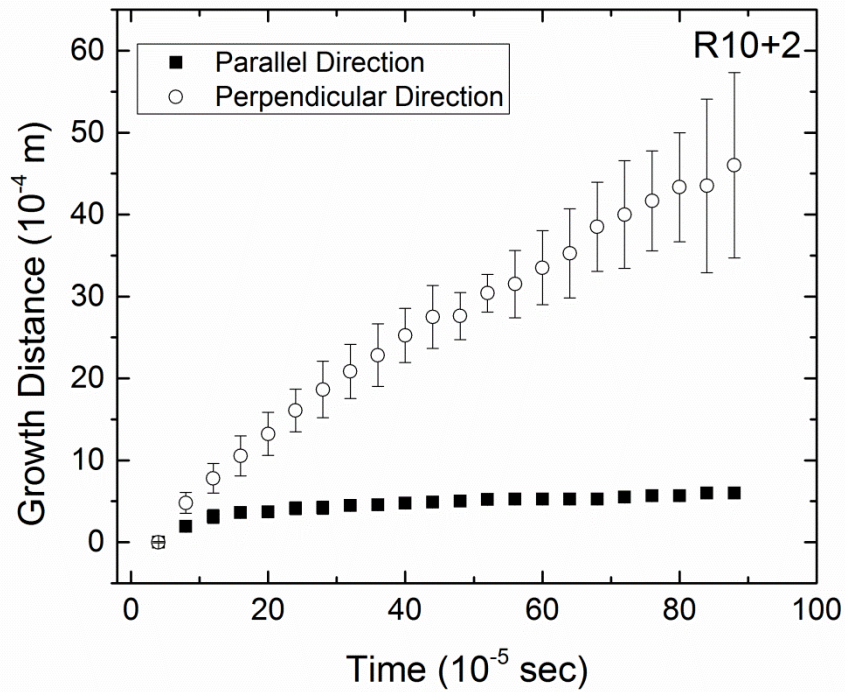
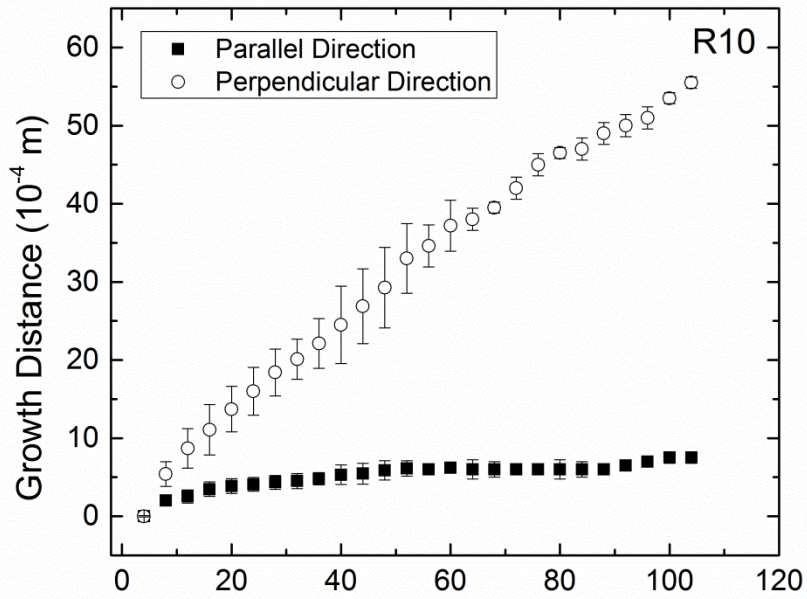


Figure 6.8 Reaction band growth distance versus time elapsed for the six rolled foils. The points are averages of 15 growths tracked throughout the high-speed reaction videos. Note that as the band growth distance increases, the number of points that constitute the average tend to drop as not all bands grow the same distance.

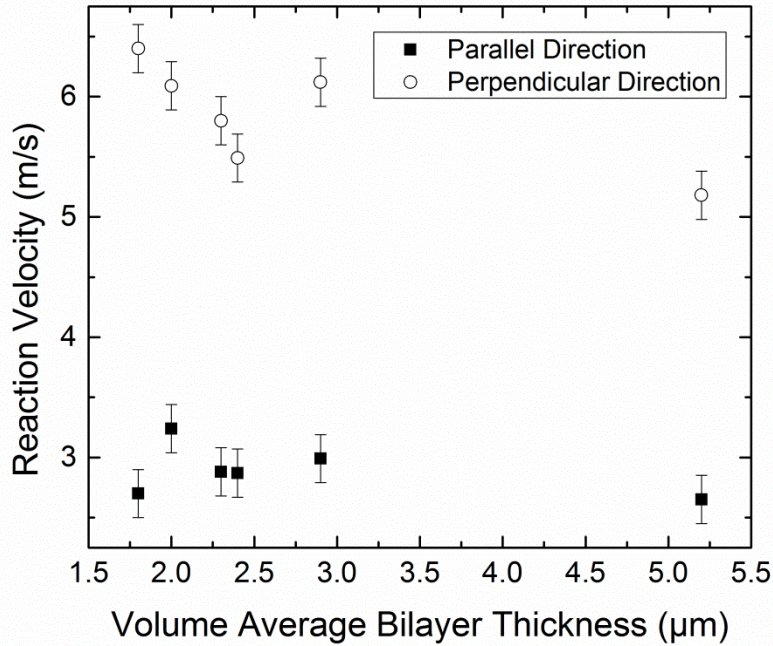


Figure 6.9 Perpendicular and parallel growth speed as a function of the volume average bilayer thickness. Linear fits are made to the curves in Figures (a)-(f) to determine the average band growth velocity in each direction. Note that the perpendicular growth rate closely tracks the net propagation velocity (Figure 6.4) while the parallel growth direction shows little trend with bilayer.

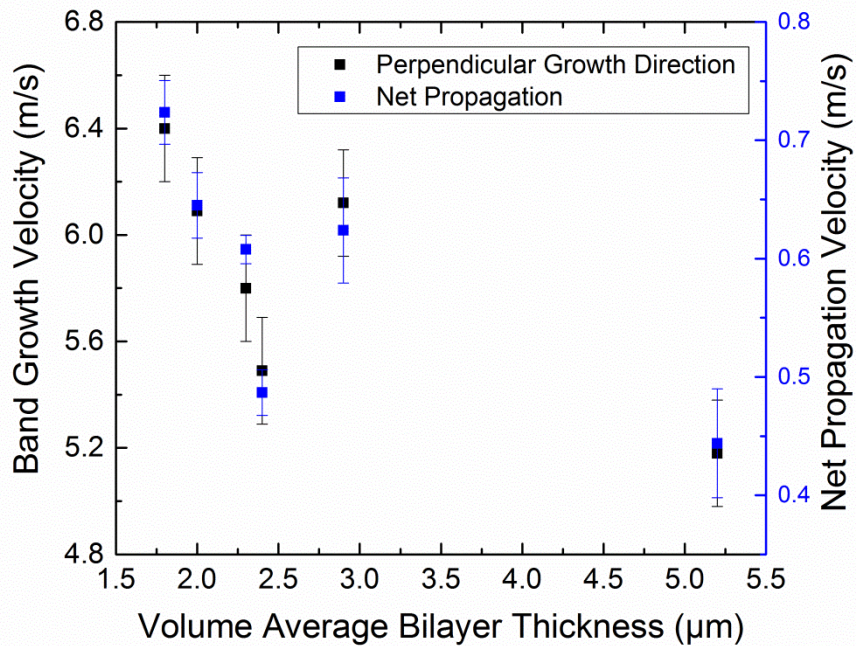


Figure 6.10 Overlay of the perpendicular band growth velocity with the net propagation velocity. Both velocities follow the same trend with volume average bilayer thickness.

## 6.4 Discussion

### *Cold-Rolled Microstructure*

Table 6.1 shows that the average bilayer thickness of all the foils consistently decreases with additional rolling passes. However, the degree of bilayer thinning for each 50% reduction in sample thickness tends to diminish with more rolling passes and the biggest decreases occur for the passes with the largest strain. As others have reported [35,37–42], both the total accumulated strain and the strain per pass control the refinement of the layering. The results in Table 6.1 support the earlier finding that using lower strains per pass and more passes to achieve a given total strain refines layering or microstructure more effectively than using higher strains per pass and fewer passes [35,37,38].

Consider samples R6 and R8 in Table 6.1. Both samples received two 50% thickness reductions in two different types of rolling passes. In first method they received two rolling passes each with a 50% reduction in thickness per pass. This yields samples R8 and R10, respectively. In the second method, the foils received six rolling passes each with a 20% reduction in thickness per pass. This yields samples R6+2 and R8+2, respectively. Both methods lead to the same total strain, as three 20% thickness reductions are approximately equivalent to one 50% reduction. The equivalency of total strain allows for a direct comparison of the microstructure refinement associated with either 20% or 50% thickness reductions per pass. Note in Table 6.1 that when the R6 foil is thinned to R8 or R6+2, and when the R8 foil is thinned to R10 or R8+2, the 20% reductions per pass lead to smaller volume average bilayer thicknesses (samples R6+2 and R8+2) than the 50% reductions per pass (samples R8 and R10). In addition, the

coefficient of variance (COV) either decreases or stays constant with the 20% thickness reductions, agreeing with previous studies [35].

### *Differential Scanning Calorimetry*

The reduction of the average bilayer thickness with rolling leads to a clear shift in the DSC curves in Figure 6.2. The peak temperatures, shown in Figure 6.3 for the first and second exotherms, gradually shift to lower temperatures as the volume average bilayer thickness decreases, corresponding to a decrease in the average diffusion distance. In addition, we see in Figure 6.3 that samples R6+2 and R8+2 have lower peak temperatures than samples R8 and R10, respectively. This matches the lower average bilayer thicknesses for samples R6+2 and R8+2, compared to samples R8 and R10 (Table 6.1).

The curves from Figure 6.2 are integrated to yield the measured heats of reaction, shown in Figure 6.4. We note that they all fall below the literature value [36], which we attribute to incomplete mixing during heating. X-ray diffraction shows only partial formation of the equilibrium B2 NiAl intermetallic after DSC heating. Some of the diffusion distances in the foils are too large to fully react on the time and temperature scale of the DSC experiments, and more stored energy will be released at high temperatures when the metastable products transform to the stable NiAl intermetallic.

### *Self-Propagating Reaction Velocity*

The self-propagating reaction velocities in Figure 6.5 follow the previously reported trend of faster reaction velocities for smaller average bilayer thicknesses [5,16–

23]. In addition, the maximum reaction temperature (Figure 6.6) is consistent with the NiAl intermetallic melting temperature, agreeing with most previously reported results [11,43,44]. However, a previous study on cold-rolled Ni/Al laminates fabricated in a similar fashion reported reaction velocities and maximum temperatures that depended only on the percent of thickness reduction during rolling and not the volume average bilayer thickness [35]. At this stage we are unable to explain this difference in bilayer thickness dependence and because the first study did not capture the steady or unsteady nature of reaction propagation, we are unable to compare reaction propagation in the two studies directly. Instead, we compare the current results with results from an earlier study of unsteady propagation in sputter deposited Al/Co [24].

The reaction process, shown in Figure 6.7, consists of four steps as noted earlier. First, a reaction band nucleates ahead of the reaction front. Second, it grows normal and parallel to the front. In the third step it grows mainly parallel to reaction front, increasing mainly in length but little in width. In the fourth and final step growth stops when the band impinges on another band growing along the reaction front. This morphology is similar to one of the two morphologies reported by McDonald *et al* [24] for reactions propagating in Al/Co multilayers with a bilayer thickness of 250 nm. In their study McDonald *et al* [24] report the nucleation of many bands along the reacting front that creates a ‘weave-like’ pattern. However, we believe that the nonuniform microstructure in the cold-rolled Ni/Al foils causes the nucleation sites for the reaction bands to be random, and the reaction front is not always planar as the reaction can propagate more quickly in some regions than in others. However, as the ‘weave-like’ pattern is most analogous to the reaction morphology in these foils, it will serve as the basis of

comparison. The band propagation velocity perpendicular to the net reaction direction is roughly an order of magnitude higher than the total velocity (0.45 vs 5.52 m/s.)

For our foils, the net reaction velocities vary between 0.45 and 0.71 m/s, and the band velocities perpendicular to the net reaction direction range between 5.2 to 6.4 m/s. We note that the differences in the two velocities in our Al/Ni foils are also approximately an order of magnitude, which agrees with McDonald et al [24]. The net propagation rate in the Al/Co foils is  $\sim 0.45$  m/s, matches the low end of our 0.45 to 0.71 m/s range in our Al/Ni foils. Also, the perpendicular band velocity seen in Al/Co lies in our observed range. Interestingly, the foils in our study have a volume average bilayer thickness that ranges from 1.8  $\mu\text{m}$  to 5.2  $\mu\text{m}$ , which is roughly an order of magnitude higher than the 250 nm bilayer in the Al/Co system. As both the local and net reaction velocities are the same, the reaction kinetics for the Al/Ni system should be faster to overcome the longer diffusion distance. The energy density of the Al/Ni system is higher than that of Al/Co (1380 J/g vs. 1285 J/g) [45] which should provide a difference in driving force, allowing the difference in diffusion distance to be overcome.

## References

- [1] Montgomery HE. Reactive Fragment. U.S. Patent 375,246, 1976.
- [2] Severin GE. Body Armor Laminate. U.S. Patent 519,644, 1980.
- [3] Hunt EM, Pantoya ML. Journal of Applied Physics 2005;98:034909.
- [4] Bockmon BS, Pantoya ML, Son SF, Asay BW, Mang JT. Journal of Applied Physics 2005;98:064903.
- [5] Weihs TP. Self-propagating Reactions in Multilayer Materials, in: Handbook of Thin Film Process Technology. Bristol: TOP; 1998.
- [6] Floro JA. Journal of Vacuum Science & Technology A: Vacuum, Surfaces, and Films 1986;4:631.
- [7] Gavens AJ, Heerden D Van, Mann AB, Reiss ME, Weihs TP. Journal of Applied Physics 2000;87:1255.
- [8] Ma E, Thompson C V., Clevenger LA, Tu KN. Applied Physics Letters 1990;57:1262.
- [9] Anselmi-Tamburini U, Munir ZA. Journal of Applied Physics 1989;66:5039.
- [10] Wickersham CE. Journal of Vacuum Science & Technology A: Vacuum, Surfaces, and Films 1988;6:1699.
- [11] Dyer, T S, Munir, Z A, Ruth V. Scripta Metallurgica et Materialia 1994;30:1281.
- [12] Reiss ME, Esber CM, Van Heerden D, Gavens AJ, Williams ME, Weihs TP. Materials Science and Engineering: A 1999;261:217.
- [13] Moore JJ, Feng HJ. Progress in Materials Science 1995;39:243.
- [14] Barzykin V V. Pure and Applied Chemistry 1992;64:909.
- [15] Arzt E. Acta Materialia 1998;46:5611.
- [16] Salloum M, Knio OM. Combustion and Flame 2010;157:288.
- [17] Salloum M, Knio OM. Combustion and Flame 2010;157:436.
- [18] Salloum M, Knio OM. Combustion and Flame 2010;157:1154.

- [19] Makino A, Law CK. *Combustion and Flame* 1995;101:551.
- [20] Makino A. *Progress in Energy and Combustion Science* 2001;27:1.
- [21] Makino A, Law CK. Twenty-Fourth Symposium (International) on Combustion/The Combustion Institute, 1992/pp. 1883-1891, in: *Twenty-Fourth Symposium on Combustion*. 1992.
- [22] Knepper R, Snyder MR, Fritz G, Fisher K, Knio OM, Weihs TP. *Journal of Applied Physics* 2009;105:083504.
- [23] Shteinberg AS, Shcherbakov VA, Munir Z a. *Combustion Science and Technology* 2001;169:1.
- [24] McDonald JP, Hodges VC, Jones ED, Adams DP. *Applied Physics Letters* 2009;94:034102.
- [25] McDonald JP, Reeves R V., Jones ED, Chinn KA, Adams DP. *Journal of Applied Physics* 2013;113:103505.
- [26] McDonald JP, Rodriguez MA, Jones ED, Adams DP. *Journal of Materials Research* 2011;25:718.
- [27] Trenkle JC, Wang J, Weihs TP, Hufnagel TC. *Applied Physics Letters* 2005;87:153108.
- [28] Deevi SC. *Journal of Materials Science* 1991;26:2662.
- [29] Yeh CL, Li RF. *Intermetallics* 2008;16:64.
- [30] Mukasyan AS, Rogachev AS, Varma A. *Chemical Engineering Science* 1999;54:3357.
- [31] Hwang S, Mukasyan AS, Varma A. *Combustion and Flame* 1998;115:354.
- [32] Moore JJ, Feng HJ. *Progress in Materials Science* 1995;39:275.
- [33] Alawieh L, Knio OM, Weihs TP. *Journal of Applied Physics* 2011;110:013509.
- [34] Jayaraman S, Knio OM, Mann a. B, Weihs TP. *Journal of Applied Physics* 1999;86:800.
- [35] Stover AK, Krywopusk NM, Fritz GM, Barron SC, Gibbins JD, Weihs TP. *Journal of Materials Science* 2013.

- [36] Boer RF, Boom R, Mattens WCM, Miedema AR, Niessen AK. Cohesion in Metals. Amsterdam: Elsevier Ltd; 1988.
- [37] Bordeaux F, Yavari R. Z Metallkde 1990;81:130.
- [38] Dinda GP, Rösner H, Wilde G. Scripta Materialia 2005;52:577.
- [39] Hebert RJ, Perepezko JH. Materials Science and Engineering: A 2004;375-377:728.
- [40] Hebert RJ, Perepezko JH. Scripta Materialia 2003;49:933.
- [41] Sieber H, Park JS, Weissmüller J, Perepezko JH. Acta Materialia 2001;49:1139.
- [42] Sieber H, Wilde G, Perepezko J. Journal of Non-Crystalline Solids 1999;250-252:611.
- [43] Munir ZA, Anselmi-Tamburini U. Materials Science Reports 1989;3:277.
- [44] Rogachev AS. Russian Chemical Reviews 2008;77:21.
- [45] Fischer SH, Grubelich MC. A Survey of Combustible Metals, Thermites, and Intermetallics for Pyrotechnic Applications, in: Lake Buena Vista: 1996.

## Chapter 7 Conclusions and Future Work

### 7.1 Conclusions

Ten different Ni/Al laminates were fabricated using cold-rolling and two different rolling thickness reductions, and the resulting bilayer thicknesses and chemistries were analyzed using cross-sectional micrographs and a numerical code. The code was validated on model images and then it was used to quantify changes in the nonuniform microstructure of the samples as a function of processing. In general, the volume average bilayer thickness decreases with more rolling passes, and the rate of decrease, when normalized against the total strain per pass, is higher for more gradual thickness reductions. In addition, the coefficient of variance decreases when a foil rolled with only large thickness reductions (50% per rolling pass) is subjected to additional rolling passes with smaller thickness reductions (20% per rolling pass). This phenomenon is attributed to less uniform layer deformation and more pinch-off when rolling with the larger 50% thickness reductions, compared to more uniform layer deformation and less pinch-off with the more gradual 20% thickness reductions. We see no clumping of large bilayers in any of the composites.

For R3, R3+2, R6, R6+2, R9 and R9+2 foils, DSC peak temperatures correlate with the volume average bilayer thickness; while the energy released during the DSC scans correlates with the volume average bilayer thickness and the bilayer thickness distribution. Velocity and  $T_{\max}$  were measured for self-propagating reactions in the laminates and were found to vary according to processing conditions and not according to the volume average bilayer thickness. Foils with additional 20% thickness reductions have both faster and hotter reactions compared to samples with only 50% thickness

reductions. We use the local bilayer thicknesses and Ni atomic fractions to predict the extent of mixing, the quantity of heat released and a foil's maximum reaction temperature. Our predictions for maximum reaction temperature show good agreement with experimental results. However, we are unable to effectively model the propagation velocity and cannot yet explain the lack of dependence on the volume average bilayer thickness.

We used the same rolling process to create R6, R6+2, R8, R8+2, R10 and R10+2 to investigate the reaction propagation using high-speed cameras. The reaction morphology seen is similar to one reported by McDonald *et al* [1] with a two-step growth process, first parallel to the net propagation direction and then perpendicular to it.. The net velocities of the foils are shown to vary inversely with the volume average bilayer thickness, as well the local propagation rate perpendicular to that direction.

From the R3+2, R6+2 and R9+2 foils, reactive Ni:Al powders were fabricated in a two-step process. First, a bulk Ni:Al reactive composite was created by cold-rolling stacked sheets to first tune the microstructure. Then, the foils were ground to create reactive particles with a range of particle sizes. The heats of reaction that were measured for the powders and foils via DSC vary not only as a function of the initial foil microstructure, but also as a function of particle size. The parent foils and large particles show two broad exotherms that correspond first to the formation of first  $\text{Al}_3\text{Ni} + \text{Ni}$  and then to the formation of  $\text{Al}_3\text{Ni}_2 + \text{NiAl} + \text{Ni}$ . However, as particle size is decreased, the sizes of the exotherms decrease, while a sharp exotherm at 640 °C appears that is attributed to Al melting and rapid mixing. In addition, the heat evolved in the DSC drops as the particle size decreases, with the biggest drop seen in powders with the coarsest

microstructure. We believe these trends are due to preferential breakup during the blending process, with the smallest particles containing the most Ni-rich and Al-rich bilayers. We have fabricated 53-106  $\mu\text{m}$  powders from the largest powders, rather than the whole foil, and find that their evolved heats and reaction sequences mirror those of the foil, strongly suggesting that the foil microstructures have a tendency to segregate into specific powder sizes during the initial breakup of the foil.

In support of the non-uniform breakup of the particles, we created bimodal distributions of bilayer chemistry for the smallest particles (53-106  $\mu\text{m}$ ) that yield densities and heats of reaction that match the measured values. The simulated bimodal distributions are taken from the normal distributions of bilayer chemistry that are measured for the full foils, and they show that the most Al-rich and Ni-rich distributions are needed for the coarsest microstructures (R6+2) and the least Al-rich and Ni-rich distributions are needed for the finest microstructures (R10+2). Lastly, the ratio of bilayers per particle can be used to predict if particles have sufficient stored energy. Below a ratio of 150, the measured heats drop sharply and reaction properties will decrease while above this ratio, heats are relatively constant and consistent reaction properties can be expected.

## **7.2 Future Work**

Compacts of mechanically fabricated composite reactive particles are of interest due to promise for green delays. Their propagation velocity would be the material parameter most important to their application. A previous study [2] on composite reactive particles has shown the time spent heating the particle to ignition controls the net

propagation velocity. However, the particles have nonuniform shapes and packing fractions, which make predicting the interparticle heat transfer difficult. Furthermore, the particles' DSC heat release is a function of particle size, which could alter the local thermal gradient between the particles.

However, as shown in Chapter 5, particles with a smaller volume average bilayer show more uniform behavior across particle size ranges. Therefore, if particles with an even smaller volume average bilayer thickness are fabricated by more (~16) rolling steps, this effect can be minimized or eliminated. High-speed optics could also be utilized to capture the maximum temperature of the propagating front and therefore the local thermal gradient. First, the packing fraction of loose compacts could be determined for each powder size range, and then the net reaction velocity could be determined as a function of packing fraction for loose compacts, as well as fully-dense compacts via swaging.

The unsteady propagation of the rolled Ni/Al foils also holds areas for further research. While many instances of unsteady propagation have been discovered in planar foils [1,3–5], there has been little theoretical analysis or numerical simulation [6]. The reaction morphology appears to change depending on the rate of energy generation versus the rate of energy dissipation [3,5,7], but typically faster reaction velocities are associated with more 'band' nucleation sites. However, the interplay of energy generation and dissipation has not been explored in detail, and predicting when reactions will proceed in an unsteady manner could be useful for bonding and reactive delay applications.

## **References**

- [1] McDonald JP, Hodges VC, Jones ED, Adams DP. Applied Physics Letters 2009;94:034102.
- [2] Fritz GM, Jores H, Weihs TP. Combustion and Flame 2011;158:1084.
- [3] McDonald JP, Hodges VC, Jones ED, Adams DP. Applied Physics Letters 2009;94:034102.
- [4] Tappan AS, Mcdonald JP, Adams DP, Jones ED. n.d.:143.
- [5] McDonald JP, Rodriguez MA, Jones ED, Adams DP. Journal of Materials Research 2011;25:718.
- [6] Alawieh L, Knio OM, Weihs TP. Journal of Applied Physics 2011;110:013509.
- [7] McDonald JP, Reeves R V., Jones ED, Chinn KA, Adams DP. Journal of Applied Physics 2013;113:103505.

## Appendix A MATLAB Code for Image Analysis

```
%This code determines the Ni/Al layer thicknesses, the bilayer
thicknesses,
%the local chemistries, the number average bilayer thickness and the
volume
%average bilayer thickness.
clc
close all
clear all

Im=input('Name of the Image:', 's'); %Name of the image to be analyzed
pic = imread(Im); %MATLAB imports the image
pinum=input('Number of pixels in a micron:', 's'); %Determine the
scale bar and enter it here
pinum=str2num(pinum);

Rnum=input('Number of times rolled:', 's'); %Imput number of times
rolled to determine intermixing distance for the diffusion model
Rnum=str2num(Rnum);
if Rnum==5;
    BI=6.5;
elseif Rnum==6;
    BI=5.3;
elseif Rnum==8;
    BI=2.2;
elseif Rnum==9;
    BI=3.2;
elseif Rnum==11;
    BI=2.4;
end

[picheight,picwidth,picdepth] = size(pic);
picheight=picheight-60; %60 refers to the scalebar
picdepth = picdepth/3;
%Turn every pixel black or white
picmean = mean(mean(mean(pic)));
bwpic=zeros(picheight-60,picwidth);
%Makes matrix of 1's and 0's to correspond to white and black pixels
for i = 1:picheight %picheight minus scalebar
    for j = 1:picwidth
        if pic(i,j) < picmean
            bwpic(i,j) = 0;
        else
            bwpic(i,j) = 1;
        end
    end
end
end
```

```

Edge=ones(size(bwpic));
for n=1:picheight;
    if bwpic(n,1)==0 %If the first pixel is black
        Edge(n,1:find(bwpic(n,:),1)-1)=0;
    elseif bwpic(n,1)==1 %if the first pixel is white
        Edge(n,1:find(bwpic(n,:)==0,1)-1)=0;
    end
    if bwpic(n,length(bwpic))==0 %if the last pixel is black
        Edge(n,(find(bwpic(n,:),1,'last')+1):length(bwpic))=0;

        else %if the last pixel is white
            Edge(n,(find(bwpic(n,:)==0,1,'last')+1):length(bwpic))=0;
        end
    end
end
%Edge is a matrix of 0's and 1's that identify the first whole layer in
%each pixel row. The 0's correspond to edge layers, and thus will not
be
%counted (see below.)

layercounter=1;
for i = 1:964; %sets number of sampling lines (must be a factor of the
number of height pixels, picheight)
ydist = i; %Sets the distance between sampling lines. Typically leave
at 1.
T=1; %Thickness of a given layer
blacklayercounter=1;
whitelayercounter=1;
for x = find(Edge(ydist,:),1):(find(Edge(ydist,:),1,'last')-1); %Edge
is used to only count the non-edge layers.
if bwpic(ydist,x)==0 && bwpic(ydist,x+1)==0 %if black and pixel next to
it is black
T=T+1; %Keeps adding to the Al layer thickness
elseif bwpic(ydist,x)==1 && bwpic(ydist,x+1)==1 %if white and pixel
next to it is white
T=T+1; %Keeps adding to the Ni layer thickness
elseif bwpic(ydist,x)==1 && bwpic(ydist,x+1)==0 %if pixel is white and
next is black
whitelayers(i,whitelayercounter)=T; %Puts the layer into the
whitelayercounter matrix with a thickness of T and resets the counting
T=1;
whitelayercounter=whitelayercounter+1; %Indexes the matrix to place
the next Ni layer into the next matrix slot.
elseif bwpic(ydist,x)==0 && bwpic(ydist,x+1)==1 %if pixel is black and
next is white
blacklayers(i,blacklayercounter)=T; %Puts the layer into the
blacklayercounter matrix with a thickness of T and resets the counting
T=1;
blacklayercounter=blacklayercounter+1; %Indexes the matrix to place
the next Al layer into the next matrix slot.
end
end
end

```

```

%The next section assembles the Al and Ni layer thickness matrices
(blacklayers and whitelayers, respectively) into the bilayer thickness
matrix and the corresponding Ni atomic fraction matrix. Two different
counting methods are used, and make two matrices, bilayers and
bilayers2 and WBRatio and WBRatio2.
for i = 1:964 %Use the same 'i' when assembling the layer matrix, as
this sets the number of layer rows that are tabulated
if find(whitelayers(i,:),1,'last')-find(blacklayers(i,:),1,'last')==0;
%If there are equal Ni layers and Al layers (Ni at one edge and Al at
the other)
for n=1:find(whitelayers(i,:),1,'last');
bilayers(i,n)=(whitelayers(i,n)+blacklayers(i,n)); %First counting
method adds the ith Al to the ith Ni
WBRatio(i,n)=(1.52.*(whitelayers(i,n))./(blacklayers(i,n)+(whitelayers(
i,n)*1.52))); %Computes the atomic percentage of Ni in the ith element
bilayers2(i,n)=(whitelayers(i,n+1)+blacklayers(i,n)); %Second counting
method adds the i+1th Ni and the ith Al (effectively counting the other
way.)
WBRatio2(i,n)=(whitelayers(i,n+1).*1.52)./((blacklayers(i,n)+whitelayer
s(i,n+1).*1.52)); %Same methodology for the WBRatio2 matrix
end
elseif find(whitelayers(i,:),1,'last')-
find(blacklayers(i,:),1,'last')>0; %If there are more Ni layers than
Al layers (Ni at both edges)
for n=1:find(blacklayers(i,:),1,'last');
bilayers(i,n)=(whitelayers(i,n)+blacklayers(i,n));
bilayers2(i,n)=(whitelayers(i,n+1)+blacklayers(i,n));
WBRatio(i,n)=(1.52.*whitelayers(i,n)./(blacklayers(i,n)+whitelayers(i,n
).*1.52));
WBRatio2(i,n)=(1.52.*whitelayers(i,n+1)./(blacklayers(i,n)+whitelayers(
i,n+1).*1.52));
end
else
for n=1:find(whitelayers(i,:),1,'last'); %If there are more Al layers
than Ni layers (Al at both edges)
bilayers(i,n)=(whitelayers(i,n)+blacklayers(i,n));
bilayers2(i,n)=(whitelayers(i,n)+blacklayers(i,n+1));
WBRatio(i,n)=(1.52.*whitelayers(i,n)./(blacklayers(i,n)+whitelayers(i,n
).*1.52));
WBRatio2(i,n)=(1.52.*whitelayers(i,n)./(blacklayers(i,n+1)+whitelayers(
i,n).*1.52));
end
end
end
%The next section of code concatenates the bilayer and WBRatio matrices
together while maintaining positional information.
size1=size(bilayers,2);
size2=size(bilayers2,2);
if size1>size2; %If one bilayer matrix is slightly wider than the other
they won't concatenate
bilayers2(964,size(bilayers,2))=0; %Makes a uniform length
WBRatio2(964,size(WBRatio,2))=0;
elseif size2>size1;
bilayers(964,size(bilayers2,2))=0;
WBRatio(964,size(WBRatio2,2))=0;
end
end

```

```

bilayers=cat(1, bilayers, bilayers2); %Combines bilayers into one
matrix
bilayers=bilayers./pinum; %Takes into account scalebar to convert from
pixels to microns
WBRatio=cat(1, WBRatio, WBRatio2);
VABT=sum(sum((bilayers.*bilayers)./(sum(sum(bilayers)))));
%Calculates the Volume Average Bilayer Thickness
%The next section takes the bilayer thickness matrix to determine the
%volume fraction of bilayers in each thickness range
%Determines the volume fraction of bilayers between 0 and 1  $\mu\text{m}$ 
worker=0;
bilayersofinterest=0;
worker=(bilayers-1.01);
worker=worker./abs(worker);
worker=worker+1;
worker=worker./2;
workerl=bilayers./abs(bilayers);
worker=workerl-worker;
bilayersofinterest=worker.*bilayers;
bilayersofinterest=bilayersofinterest(~isnan(bilayersofinterest));
Volfrac1=sum(sum(bilayersofinterest))./sum(sum(bilayers));
%Determines the volume fraction of bilayers between 1 and 2  $\mu\text{m}$ 
worker=0;
bilayersofinterest=0;
worker=(bilayers-2.01);
workerl=bilayers-1.01;
workerl=workerl./abs(workerl);
workerl=workerl+1;
workerl=workerl./2;
worker=worker./abs(worker);
worker=worker+1;
worker=worker./2;
worker=workerl-worker;
bilayersofinterest=worker.*bilayers;
bilayersofinterest=bilayersofinterest(~isnan(bilayersofinterest));
Volfrac2=sum(sum(bilayersofinterest))./sum(sum(bilayers));
%Determines the volume fraction of bilayers between 2 and 4  $\mu\text{m}$ 
worker=0;
bilayersofinterest=0;
worker=(bilayers-4.01);
worker=worker./abs(worker);
worker=worker+1;
worker=worker./2;
workerl=bilayers-2.01;
workerl=workerl./abs(workerl);
workerl=workerl+1;
workerl=workerl./2;
worker=workerl-worker;
bilayersofinterest=worker.*bilayers;
bilayersofinterest=bilayersofinterest(~isnan(bilayersofinterest));
Volfrac4=sum(sum(bilayersofinterest))./sum(sum(bilayers));

```

```

%Determines the volume fraction of bilayers between 4 and 6  $\mu\text{m}$ 
worker=0;
bilayersofinterest=0;
worker=(bilayers-6.01);
worker=worker./abs(worker);
worker=worker+1;
worker=worker./2;
workerl=bilayers-4.01;
workerl=workerl./abs(workerl);
workerl=workerl+1;
workerl=workerl./2;
worker=workerl-worker;
bilayersofinterest=worker.*bilayers;
bilayersofinterest=bilayersofinterest(~isnan(bilayersofinterest));
Volfrac6=sum(sum(bilayersofinterest))./sum(sum(bilayers));
%Determines the volume fraction of bilayers between 6 and 8  $\mu\text{m}$ 
worker=0;
bilayersofinterest=0;
worker=(bilayers-8.01);
worker=worker./abs(worker);
worker=worker+1;
worker=worker./2;
worker=real(worker);
workerl=bilayers-6.01;
workerl=workerl./abs(workerl);
workerl=workerl+1;
workerl=workerl./2;
worker=workerl-worker;
bilayersofinterest=worker.*bilayers;
Volfrac8=sum(sum(bilayersofinterest))./sum(sum(bilayers));
%Determines the volume fraction of bilayers between 8 and 10  $\mu\text{m}$ 
worker=0;
bilayersofinterest=0;
worker=(bilayers-10.01);
worker=worker./abs(worker);
worker=worker+1;
worker=worker./2;
workerl=bilayers-8.01;
workerl=workerl./abs(workerl);
workerl=workerl+1;
workerl=workerl./2;
worker=workerl-worker;
worker=real(worker);
bilayersofinterest=worker.*bilayers;
Volfrac10=sum(sum(bilayersofinterest))./sum(sum(bilayers));
%Determines the volume fraction of bilayers between 00 and 12  $\mu\text{m}$ 
worker=0;
bilayersofinterest=0;
worker=(bilayers-12.01);
worker=worker./abs(worker);
worker=worker+1;
worker=worker./2;
workerl=bilayers-10.01;
workerl=workerl./abs(workerl);
workerl=workerl+1;
workerl=workerl./2;
worker=workerl-worker;

```

```

worker=real(worker);
bilayersofinterest=worker.*bilayers;
Volfrac12=sum(sum(bilayersofinterest))./sum(sum(bilayers));
%Determines the volume fraction of bilayers between 12 and 15 μm
worker=0;
bilayersofinterest=0;
worker=(bilayers-15.01);
worker=worker./abs(worker);
worker=worker+1;
worker=worker./2;
worker1=bilayers-12.01;
worker1=worker1./abs(worker1);
worker1=worker1+1;
worker1=worker1./2;
worker=worker1-worker;
worker=real(worker);
bilayersofinterest=worker.*bilayers;
Volfrac15=sum(sum(bilayersofinterest))./sum(sum(bilayers));
%Determines the volume fraction of bilayers between 15 and 20 μm
worker=0;
bilayersofinterest=0;
worker=(bilayers-20.01);
worker=worker./abs(worker);
worker=worker+1;
worker=worker./2;
worker1=bilayers-15.01;
worker1=worker1./abs(worker1);
worker1=worker1+1;
worker1=worker1./2;
worker=worker1-worker;
worker=real(worker);
bilayersofinterest=worker.*bilayers;
Volfrac20=sum(sum(bilayersofinterest))./sum(sum(bilayers));
%Determines the volume fraction of bilayers between 20 and 25 μm
worker=0;
bilayersofinterest=0;
worker=(bilayers-25.01);
worker=worker./abs(worker);
worker=worker+1;
worker=worker./2;
worker1=bilayers-20.01;
worker1=worker1./abs(worker1);
worker1=worker1+1;
worker1=worker1./2;
worker=worker1-worker;
worker=real(worker);
bilayersofinterest=worker.*bilayers;
Volfrac25=sum(sum(bilayersofinterest))./sum(sum(bilayers));
%Determines the volume fraction of bilayers with Ni atomic fractions
less than 0.1
worker=0;
worker1=0;
bilayersofinterest=0;
worker=(WBRatio-.1001);
worker=worker./abs(worker);
worker=worker+1;
worker=worker./2;

```

```

worker1=WBRatio./abs(WBRatio);
worker=worker1-worker;
bilayersofinterest=worker.*bilayers;
Chemfrac1=sum(sum(bilayersofinterest))./sum(sum(bilayers));
%Determines the volume fraction of bilayers with Ni atomic fractions
between 0.1 and 0.2
worker=0;
bilayersofinterest=0;
worker=(WBRatio-.2001);
worker=worker./abs(worker);
worker=worker+1;
worker=worker./2;
worker1=WBRatio-.1001;
worker1=worker1./abs(worker1);
worker1=worker1+1;
worker1=worker1./2;
worker=worker1-worker;
worker=real(worker);
bilayersofinterest=worker.*bilayers;
Chemfrac2=sum(sum(bilayersofinterest))./sum(sum(bilayers));
%Determines the volume fraction of bilayers with Ni atomic fractions
between 0.2 and 0.3
worker=0;
bilayersofinterest=0;
worker=(WBRatio-.3001);
worker=worker./abs(worker);
worker=worker+1;
worker=worker./2;
worker1=WBRatio-.2001;
worker1=worker1./abs(worker1);
worker1=worker1+1;
worker1=worker1./2;
worker=worker1-worker;
worker=real(worker);
bilayersofinterest=worker.*bilayers;
Chemfrac3=sum(sum(bilayersofinterest))./sum(sum(bilayers));
%Determines the volume fraction of bilayers with Ni atomic fractions
between 0.3 and 0.4
worker=0;
bilayersofinterest=0;
worker=(WBRatio-.4001);
worker=worker./abs(worker);
worker=worker+1;
worker=worker./2;
worker1=WBRatio-.3001;
worker1=worker1./abs(worker1);
worker1=worker1+1;
worker1=worker1./2;
worker=worker1-worker;
worker=real(worker);
bilayersofinterest=worker.*bilayers;
Chemfrac4=sum(sum(bilayersofinterest))./sum(sum(bilayers));

```

```

%Determines the volume fraction of bilayers with Ni atomic fractions
between 0.4 and 0.5
worker=0;
bilayersofinterest=0;
worker=(WBRatio-.5001);
worker=worker./abs(worker);
worker=worker+1;
worker=worker./2;
worker1=WBRatio-.4001;
worker1=worker1./abs(worker1);
worker1=worker1+1;
worker1=worker1./2;
worker=worker1-worker;
bilayersofinterest=worker.*bilayers;
Chemfrac5=sum(sum(bilayersofinterest))./sum(sum(bilayers));
%Determines the volume fraction of bilayers with Ni atomic fractions
between 0.5 and 0.6
worker=0;
bilayersofinterest=0;
worker=(WBRatio-.6001);
worker=worker./abs(worker);
worker=worker+1;
worker=worker./2;
worker1=WBRatio-.5001;
worker1=worker1./abs(worker1);
worker1=worker1+1;
worker1=worker1./2;
worker=worker1-worker;
bilayersofinterest=worker.*bilayers;
Chemfrac6=sum(sum(bilayersofinterest))./sum(sum(bilayers));
%Determines the volume fraction of bilayers with Ni atomic fractions
between 0.6 and 0.7
worker=0;
bilayersofinterest=0;
worker=(WBRatio-.7001);
worker=worker./abs(worker);
worker=worker+1;
worker=worker./2;
worker1=WBRatio-.6001;
worker1=worker1./abs(worker1);
worker1=worker1+1;
worker1=worker1./2;
worker=worker1-worker;
bilayersofinterest=worker.*bilayers;
Chemfrac7=sum(sum(bilayersofinterest))./sum(sum(bilayers));
%Determines the volume fraction of bilayers with Ni atomic fractions
between 0.7 and 0.8
worker=0;
bilayersofinterest=0;
worker=(WBRatio-.8001);
worker=worker./abs(worker);
worker=worker+1;
worker=worker./2;
worker1=WBRatio-.7001;
worker1=worker1./abs(worker1);
worker1=worker1+1;
worker1=worker1./2;

```

```

worker=worker1-worker;
bilayersofinterest=worker.*bilayers;
Chemfrac8=sum(sum(bilayersofinterest))./sum(sum(bilayers));
%Determines the volume fraction of bilayers with Ni atomic fractions
between 0.8 and 0.9
worker=0;
bilayersofinterest=0;
worker=(WBRatio-.9001);
worker=worker./abs(worker);
worker=worker+1;
worker=worker./2;
worker1=WBRatio-.8001;
worker1=worker1./abs(worker1);
worker1=worker1+1;
worker1=worker1./2;
worker=worker1-worker;
bilayersofinterest=worker.*bilayers;
Chemfrac9=sum(sum(bilayersofinterest))./sum(sum(bilayers));
worker=0;
%Determines the volume fraction of bilayers with Ni atomic fractions
greater than .9
bilayersofinterest=0;
worker=(WBRatio-1);
worker=worker./abs(worker);
worker=worker+1;
worker=worker./2;
worker1=WBRatio-.9001;
worker1=worker1./abs(worker1);
worker1=worker1+1;
worker1=worker1./2;
worker=worker1-worker;
bilayersofinterest=worker.*bilayers;
Chemfrac10=sum(sum(bilayersofinterest))./sum(sum(bilayers));
%This section calculates the expected volumetric heat release for each
%bilayer by looking at its chemistry and
for i = 1:1928; %sets number of sampling lines (must be a factor of the
bwpicheight)
ydist = i; %picheight/i; %distance between sampling lines
counter=1;
x=1;
while x <= find(bilayers(ydist,:),1,'last');
%If a bilayer is greater than the volume average bilayer thickness
if bilayers(ydist,x)>2*BI;
chemdistbil100(ydist,x)=bilayers(ydist,x); %Bilayer will have unreacted
thickness accounted for later
totalchem100(ydist,x)=WBRatio(ydist,x); %Chemistry is simply chem of
bilayer
counter=counter+1;
x=x+1;
else %Bilayer is less than VABT
chemdistbil100(ydist,x)=bilayers(ydist,x); %Bilayer thickness stays the
same
leftchem=0;
rightchem=0;
ghostcounterright=0;

```

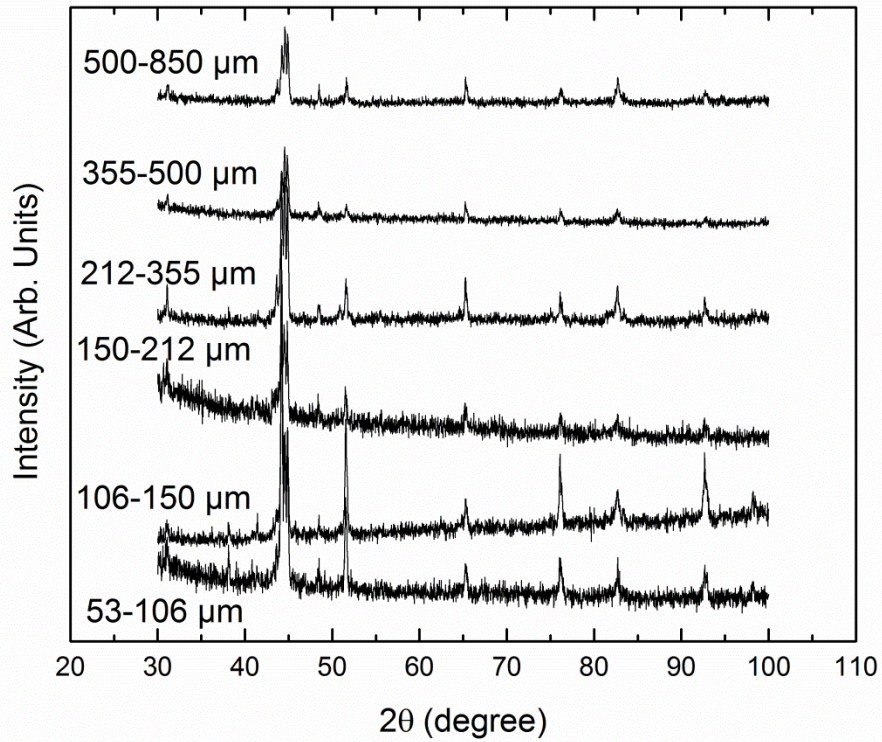
```

while sum(bilayers(ydist,x:x+ghostcounterright))<BI; %start adding
bilayers until you reach a full VABT in the right direction
if x+ghostcounterright==find(bilayers(ydist,:),1,'last');
break
end
ghostcounterright=ghostcounterright+1;
end
ghostcounterleft=0; %And the left
while sum(bilayers(ydist,x:-1:x+ghostcounterleft))<BI
if x+ghostcounterleft==find(bilayers(ydist,:),1,'first');
break
end
ghostcounterleft=ghostcounterleft-1;
end
if (x+ghostcounterleft)>1; %Determines the volume average chemistry of
the bilayers to the left
leftremainder=WBRatio(ydist,x+ghostcounterleft)*(BI-
sum(bilayers(ydist,x:-1:x+ghostcounterleft+1)))/(2*BI);
leftchem=sum(WBRatio(ydist,x:-
1:x+ghostcounterleft+1).*bilayers(ydist,x:-
1:x+ghostcounterleft+1))/(BI)+leftremainder.*WBRatio(ydist,x+ghostcount
erleft);
end
if (x+ghostcounterright)<find(bilayers(ydist,:),1,'last'); %And the
right
rightremainder=WBRatio(ydist,x+ghostcounterright)*(BI-
sum(bilayers(ydist,x:x+ghostcounterright-1)))/(2*BI);
rightchem=sum(WBRatio(ydist,x:x+ghostcounterright-
1).*bilayers(ydist,x:x+ghostcounterright-
1))/(BI)+rightremainder.*WBRatio(ydist,x+ghostcounterright);
end
totalchem100(ydist,x)=sum(WBRatio(ydist,x+ghostcounterleft+1:x+ghostcou
nterright-1).*bilayers(ydist,x+ghostcounterleft+1:x+ghostcounterright-
1))/(2*BI)+rightremainder+leftremainder; %Tabulates the entire bilayer
chemistry
if leftchem~=0 && rightchem~=0;
chemdist100(ydist,x)=(leftchem+rightchem)/2;
elseif leftchem==0;
chemdist100(ydist,x)=rightchem;
elseif rightchem==0;
chemdist100(ydist,x)=leftchem;
end
x=x+1;
counter=counter+1;
end
end
end
%Determines unreacted fraction
unreacted100=bilayers-2*BI;
unreacted100(unreacted100<0)=0;
unreacted100=sum(sum(unreacted100))/sum(sum(bilayers));
unreacted100=1-unreacted100;
bilayersssum=sum(nonzeros(bilayers));
%Calculates expected heat release using a fitted enthalpy curve
ExpectedHeatRelease=unreacted100.*(sum(sum((totalchem100.*totalchem100.
*381.14-370.08.*totalchem100+30.761).*bilayers))/bilayersssum)*1000/-
26.2;

```

```
%Output the relevant calculations to Excel using xlswrite  
xlswrite('ChemandBiDists.xls', [ExpectedHeatRelease]);
```

## Appendix B X-ray Diffraction Patterns of Ni/Al Laminate Powders After DSC Heating to 620° C.



Appendix B: Peak at 38  $2\theta$  is the only unique Al peak and is seen only in powders with a diameter less than 150  $\mu\text{m}$ .

## **Biography**

Adam Stover, born in Williamsport, PA and raised in Lock Haven, PA graduated from Central Mountain High School in 2002. From there, he enrolled at Haverford College to pursue a bachelor's degree in chemistry and graduated in May, 2006. After a brief stint in Pittsburgh, PA as a professional poker player, he started his doctoral studies as a chemist at The Johns Hopkins University. However, after taking a course on the mechanical properties of materials with who is now his current thesis advisor, decided to switch into metallurgy and materials science and engineering.

After he graduates, he will join Special Metals Inc. in Utica, New York as a senior process engineer to support their production of Ni-based superalloys.